PMAI

www.pmai.in

TRANSACTIONS OF POWDER METALLURGY ASSOCIATION OF INDIA

Chief Editor - P. Ramakrishnan

www.pmai.in

TRANSACTIONS OF POWDER METALLURGY ASSOCIATION OF INDIA

Vol. 45 No.1, June 2019

Chief Editor - P. Ramakrishnan

Powder Metallurgy Association of India

Office Bearers

President
　　Shri N. Gopinath

Vice President
　　Shri Deepak Grover
　　Shri Narendra Dhokey
　　Shri Rajendra Sethiya

General Secretary
　　Dr. Deep Prakash

Hon. Treasurer
　　Dr. Murli Gopal Krishnamoorty

Joint Secretary
　　Shri Aniket Gore
　　Shri Rajat Varshney

Editorial

PMAI organised a very successful 5th.International Conference on powder metallurgy in Asia 2019 for the first time in India at the Hotel JW Marriot, Pune. Trans. PMAI. Vol.45(1)2019 contain selected papers from this outstanding event. Pandemic outbreak of COVID-19 has disrupted the global activities of life in an unprecedented way including the publication of Trans. PMAI. Vol.45.2019.

First paper deals with the atomizing plants using argon or nitrogen closed couple system, which guarantee defined grain sizes and distribution of alloy metal powder along with reset of anti-satellite system for spherical particle shape for good flow properties during 3D printing process. The classical flowmeters are unable to give pertinent information about powder flow behavior in powder based additive manufacturing. The paper highlights how the Granudrum instrument is able to make spreadability and flowability classification between two different bronze powders. Next paper deals with mechanical activation of mill scale with carbon by high energy attrition milling followed by reduction, resulted in iron powders with a particle size of 0.4 micron and crystallite size <100nm and are evaluated for magnetic properties for medical and biological applications. This is followed by an article on low fines technology whereby -44microns fines are removed from the starting powder which can yield higher density at room temperature compaction with reduced lubricant content. The technology can further enhance the density achieved by warm compaction also. Next article is on the Variable valve timing system which can reduce fuel consumption in automobile engines. The part manufacturer must control the dimensional changes and density gradient in the parts and this can be achieved by establishing suitable collaboration between the part producer and powder manufacturer.

This is followed by an article describing the nitriding processes of ferrous PM components including plasma nitriding, gas nitrocarburizing, quench-polish-quench complex bath nitriding to improve the overall performance of the products. Powder injection molding in the microworld deals with the characteristics and process details of micro metal injection molding for manufacturing complex shaped parts with final accuracies. Next paper is on powder injection molding to manufacture functionally graded 17-4PH & 316L stainless steel powders. Changes in microstructure and mechanical properties of selective laser melted Al-10%Si-04% Mg alloy after hot isostatic pressing is the subject matter of the next paper. Improving machinability of PM components with the use of Ancorcut in comparison with MnS is discussed in the next article. Processing of high-density W-Cu alloy by Nano powders by mechano-chemical process is the subject matter of the next paper. Next paper is on the current trends and advances in fabrication and application of diamond tools. There are continuous developments in the raw materials, tools and their production routes to improve the working characteristics and introduce them to new application areas. The effect of different reinforcements such as borides, nitrides and carbides in the development of Titanium based composites have been covered. Next paper deals how FEM simulation tools can be used to mitigate issues related to distortion in additive manufacturing process of thin walled structures. The final paper is on the computational fluid dynamics simulations for additive manufacturing. Case studies from industries and academia have been presented and discussed to highlight the use of computational fluid dynamics and numerical methods in understanding powder based fusion processes.

P. Ramakrishnan

CONTENTS

ADDITIVE MANUFACTURING AND POWDER METALLURGY AT SMS GROUP – PROVIDING MOST ADVANCED POWDER ATOMIZATION PLANTS FOR THE PRODUCTION OF HIGH-GRADE METAL POWDERS

T. Brune, T. Nerzak, H. J. Odenthal, P. Weiland and M. Hüllen

SMS group GmbH, Moenchengladbach, Germany

Abstract: *The SMS group is a group of global players in plant construction and mechanical engineering for the steel and nonferrous metals processing industry with over 14,000 employees in more than 50 global locations. The objective is to provide integrated high-end turn-key solutions for our customers also in the field of Additive Manufacturing (AM). Therefore, SMS is targeting to become a full liner by taking all major processing steps of 3D printing into account, including powder atomization, design and 3D printing. SMS group has set up a 3D Competence Center at their location in Moenchengladbach, Germany to continuously investigate all major steps of metal additive manufacturing. A full scale powder atomization plant* **(see Picture 1)** *for the production of high-grade metal powders has been built to gain detailed operator know-how and production expertise to develop and produce different AM powders.*

Picture 1: Full scale powder atomization plant in the 3D Competence Center at SMS group Germany

The metal powders are tested in a fully equipped laboratory which guarantees high qualities and are further processed using a laser based powder bed fusion (LPBF) printer.

The main goal is to analyze and develop the different influencing factors during atomization and further powder processing and the correlating properties during processing steps. By this full liner approach for the entire value chain of additive manufacturing, SMS can bring the best value to customers.

In this paper, the Powder Atomization Plant and its technical features are described in detail to show the correlations of the powder processing and best results of the laser based powder bed fusion printer. In addition, a detailed description of some AM design solutions that have already been implemented with success, thereby effectively contributing to significant increase in performance of our customer's plants will be shown. The melting and refining of metals and alloys is taking place under vacuum or inert gas atmosphere to realize highest cleanness of the powder. The atomizing process with argon or nitrogen, using the close-coupled principal, guarantees defined grain sizes and distribution of metal powders. A unique and self-developed anti-satellite system is used for the needed spherical particle shapes which guarantee good flow properties during the 3D printing process.

Detailed know-how of the atomizing process is necessary to ensure highest quality standards of the powder and therefore SMS currently develops

a CFD model that is able to calculate the particle size distribution for varying process parameters such as steel grade, superheating temperature of melt, primary and secondary nozzle size, nozzle protrusion length, gas flow pressure, gas-to-liquid ratio (GLR) and others. Jointly with academic research partners, a laboratory experimental setup for water atomization has been built-up to investigate the interaction between shock/expansion wave structure and water flow (Schlieren measurement, PDA, high speed observations). Parallel to the pilot-plant operation and the laboratory studies, the development of a CFD model for the close-coupled atomization process has been started. The behavior of the liquid fragments beneath the nozzles, the interaction between liquids (melt, water) and gas (shocks, expansion waves) and the lick-back phenomena will be predicted by a CFD model.
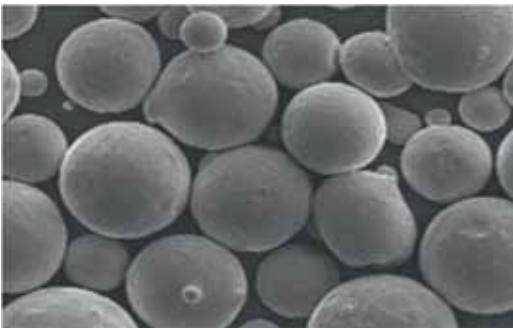
Conclusion:

The full liner approach of SMS group ensures in-depth know-how of all major processing steps of additive manufacturing. All the gained technological understanding is transferred into the Powder Atomization Plant. Customers are enabled to become the leading supplier of the AM industry by combining a high utilization grade of metal powder and the right particle size and shape for additive manufacturing at highest quality.

POWDERS SPREADABILITY ASSESSEMENT IN ADDITIVE MANUFACTURING USING NEW POWDER RHEOMETRY (GRANUDRUM INSTRUMENT)

Quentin Ribeyre[a], Geoffroy Lumay[b] and Filip Francqui[a]

[a]Granutools, Rue Jean-Lambert Defrêne, Awans, Belgium
[b]University of Liège (Belgium)

Introduction

Granular materials and fine metallic powders are widely used in several Additive Manufacturing (AM) applications. For example, in SLS (Selective Laser Sintering), SLM (Selective Laser Melting) and EBM (Electron Beam Melting) techniques, successive thin layers of powders are created with a ruler or with a rotating cylinder. Each layer is partially sintered or melted with and energy beam (laser or electron beam). The layer thickness defines a vertical resolution. Therefore, a thin-layer leads to a better resolution. In order to obtain this effect, the powder is as fine as possible. Unfortunately, when the grain size decreases, the cohesiveness increases and the flowability decreases. Moreover, the powder becomes more and more sensitive to moisture. Thus, a compromise between grains size and flowability must be found. The quality of the part build with Additive Manufacturing is directly related to the powder flowing properties. The flowability must be good enough to obtain homogeneous successive powder layers. Different recent publications have evidencing that the classical flowmeters are unable to give pertinent information about powder flow behaviour in powder-bed-based AM. In shear cell tested and classical rheometers, the existence of a compressive load is incompatible with the free surface flow used in AM devices. However, the measurement method based on the rotating drum is a good candidate because the powder flow is analysed precisely at the powder/air interface without any compressive load. Moreover, the rotating drum geometry allows studying the natural aeration of the powder during the flow. In this paper, we show how the GranuDrum instrumentis able to make

spreadability& flowability classification between two similar bronze powders provided by the Retsch company. Material and Methods Two bronze powders were selected for this study, they were provided by the Retsch company and they are called sample A and B as shown in Fig. 1 & 2 respectively.

Figure 1: Sample A.
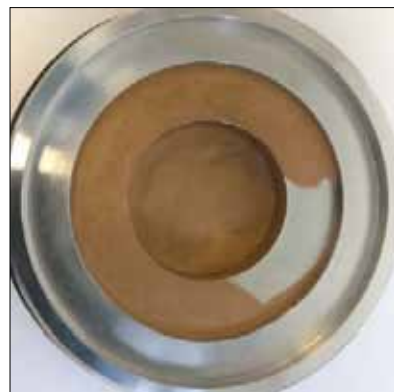
Figure 2: Sample B.

All powders are orange / brown in colour and sample A is darker than sample B.
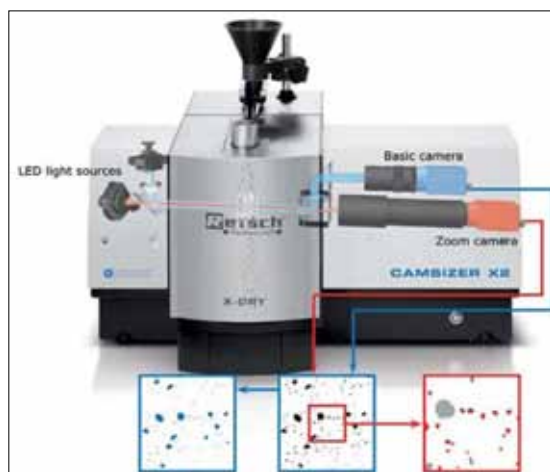
Figure 3: CAMSIZER X2.

The Particles Size Distribution (PSD) and shape characterisation were carried out by the Retsch Technology GmbH using the CAMSIZER X2 instrument shown in Figure 3. This instrument is a powerful, extremely versatile particle analyser with a wide measuring range that combines state-of-the-art camera technology with flexible dispersion options. Based on the principle of Dynamic Image Analysis, the CAMSIZER X2 provides precise particle size and shape information of powders, granules and suspensions in a measuring range from 0.8µm to 8mm.

In the measurement set-up of Dynamic Image Analysis (DIA), particles, typically in a size range from 1 micron to several millimetres, move in front of a camera system, either transported by air flow or in liquid. Thus, it is possible to obtain data from hundreds of thousands up to several millions of particles within a few minutes. The results are based on a representative amount of sample material and are therefore statistically sound.

Figure 3 displays the principal set-up of the optics for Dynamic Image Analysis. As the particles pass through the field of view a light source illuminates the particles from one direction while a camera system takes pictures from the opposite side. A software evaluates the shadow projections of the particles to determine the size distribution of the sample with a high acquisition rate. A unique feature of Retsch Technology's CAMSIZER X2 is the dual camera technology: Two cameras with different magnifications cover a wide measuring range. One camera with high magnification is optimized for the analysis of small particles, a second camera with a lower magnification but wide field of view allows to simultaneously analyse the larger particles with high detection efficiency. The CAMSIZER X2 records more than 300 pictures per second with one single image easily containing several hundreds of particles. DIA allows to measure particle size distribution and quantitative particle shape (percentage of round versus irregular shaped particles, satellites, agglomerates etc.). Smallest amounts of oversized, undersized, or irregular shaped particles can be detected, even with a percentage as low as 0.01%. DIA enables the user to obtain a comprehensive and thorough understanding of size and morphology related to sample properties and thus is the ideal method for both R & D applications and quality control because it provides accuracy and sensitivity as well as robustness and easy handling.

Figure 4 compares the cumulative and frequency density distribution curves of powders A and B. Both powders are in the size range of 20µm to 70µm, which is typical for additive manufacturing processes. Sample B is coarser with an average particle size D50 of 47.0µm, whereas Sample A has a D50 of 32.1µm. Sample A contains about 9% of dust below 20µm. The amount of dust in sample A is much smaller, only 0.2%.

The size and shape analysis by the CAMSIZER X2 confirm that both samples differ in particle size and particle shape. The pictures indicate that sample A contains many particles with satellites, that means large and small round particles fused together. Sample B seems

POWDERS SPREADABILITY ASSESSMENT IN ADDITIVE MANUFACTURING USING NEW POWDER RHEOMETRY (GRANUDRUM INSTRUMENT)
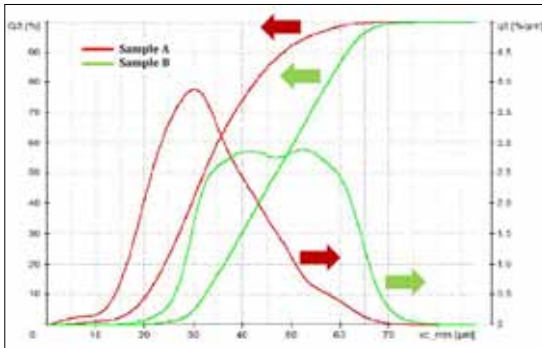
Figure 4: Particle Size Distribution, shown as cumulative distribution (left y-axis) and frequency density distribution (right Y-axis). The graph compares the result from sample A (red) and sample B (green). Sample A is finer and contains more dust.

to consist mainly of almost perfectly round particles, with only a few satellites and few odd shaped particles (ellipse, broken). In addition to the qualitative shape analysis from the pictures, the quantitative shape analysis from the graphs and tables allows to determine specifications for the acceptable particle shape as shown in figure 5. In this example, about 10% of the particles in sample B have an aspect ratio (b/l) smaller than 0.9, whereas 63% of the particles from sample A are below b/l 0.9. The average aspect ratio of sample A is 0.86, whereas the average aspect ratio of sample B is much higher, 0.97.
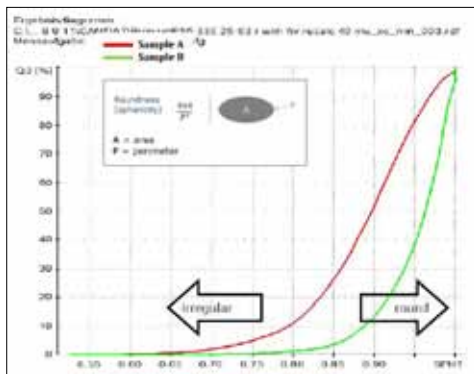
Figure 5: Particles Shape analysis. The graph shows the roundness (SPHT) versus the sample amount. The particles in sample B are rounder than the particles in sample A.

Experimental results

The powders flowability was investigated using the GranuDrum instrument (GranuTools, Belgium) It is an automated powder flowability measurement method based on the rotating drum principle. A horizontal cylinder with transparent sidewalls called drum is half filled with the sample of powder. The drum rotates around its axis at an angular velocity ranging from 2 rpm to 60 rpm. A CCD camera takes snapshots (30 to 100 images separated by 1s) for each angular velocity. The air/powder interface is detected on each snapshot with an edge detection algorithm. Afterward, the average interface position and the fluctuations around this average position are computed. Then, for each rotating speed, the flowing angle (also known in the literature as 'dynamic angle of repose') αf is computed from the average interface position and the dynamic cohesive index σf is measured from the interface fluctuations. In general, a low value of the flowing angle αf corresponds to a good flowability. The flowing angle is influenced by a wide set of parameters: the friction between the grains, the shape of the grains, the cohesive forces (van der Waals, electrostatic and capillary forces) between the grains. The dynamic cohesive index σf is only related to the cohesive forces between the grains shown in figure 6. A cohesive powder leads to an intermitted flow while a non-cohesive powder leads to a regular flow. Therefore, a dynamic cohesive index closes to zero corresponds to a non-cohesive powder. When the powder cohesiveness increases, the cohesive index increases accordingly. The flowability results are as follow:
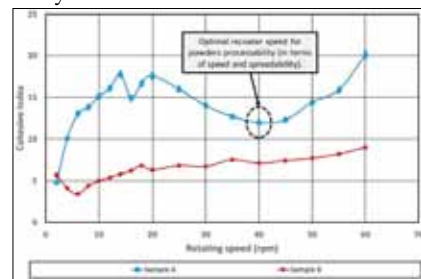
Figure 6: Cohesive Index versus Rotating drum speed.

First of all, if we look at a low velocity (2rpm), we can see that the powders flowability classification is difficult to achieve. However, when the drum speed is increasing, the products characterisation can be achieved easily.

The sample B shows a shear-thickening behaviour, in other words, its spreadability is decreasing, when the shear stress applied is getting more and more important. This fact is probably due to its spherical shape. However, the maximum measured Cohesive Index is close to 8 at 60rpm, therefore, the product spreadability is excellent over the whole velocity range. Since, the particle size distribution is inversely proportional to flowability, these observations are in good compliance with particles characterisation previously described.

Sample A behaviour is more complex, indeed, between 2 to 16rpm, a shear-thickening trend is highlighted, then between 16 to 40rpm, the powder spreadability is increasing. Finally, above 40rpm, another shear-thickening behaviour is measured, resulting in a diminution is the powder spreadability. This complex behaviour may be link to the particles shape which is far away from a sphere. Finally, due to its lower particle shape distribution (in comparison with sample B), this product highlights a lower flowability/spreadability.

These results are highly interesting, especially for sample A, indeed, the GranuDrum measurements allow us to define an optimal recoater, i.e., to achieve the optimal spreadability at the optimal process speed. This value is close to 40rpm, and thus to 170mm/s (see Appendix 2). On addition, observations made on powders cohesive index at low speed (i.e. 2rpm) are in good compliance with Retsch thoughts and GranuPack data interpretations.

Conclusions

In this paper it was highlighted that the GranuDrum instrument is able to make classification between two bronze powders.

This new powder rheometry technic (with the Cohesive Index measurement) is a promising way for powders spreadability assessments. Moreover, it can also show huge differences between two similar powders in terms of particles size distribution.

During this study, two samples were selected, they were bronze powders, one with big particle size and spherical shape and the other one with smaller particles and non-spherical shape. However, despite these differences, it was impossible to conclude about powder flowability in quasi-static conditions. Indeed, the powders Cohesive Index at 2 rpm were similar. Nonetheless, working at higher speeds, several differences were observed:

1) Smallest particle size distribution shows the lower Cohesive Index, and consequently the best spreadability. In addition, due to the spherical shape a shear-thickening behaviour is highlighted.

2) Biggest particle size distribution has the lowest spreadability (due to its highest Cohesive Index) and also a complex rheological behaviour due to its non-spherical shape.

Acknowledgments

PREPARATION AND MAGNETIC CHARACTERIZATION OF NANOSTRUCTURED IRON POWDER FROM CARBOTHERMIC REDUCTION OF MECHANICALLY ACTIVATED MILL SCALE

S. Junwal, Nitika Kundan and P. R. Soni

Department of Metallurgical and Materials Engineering, Malaviya National Institute of Technology, Jaipur, India

Abstract: *In this study, the nanostructured iron powder was obtained from mechanically activated mill scale and its magnetic properties were explored. Mill scale and activated charcoal powder were mixed in a stoichiometric ratio. Mechanical activation of this mixture was carried out in a high energy attrition mill for 60 hours. The activated mill scale was then reduced at 950ºC for 24 hours in a sealed graphite crucible in an electrical furnace. The sponge iron cake obtained was pulverized and magnetic separation was done. The iron powder thus obtained was then characterized by XRD and FESEM. X-ray diffraction studies confirmed the presence of the cubic phase of iron. The FESEM analysis showed that the iron powder obtained have the irregular morphology of spongy type. The average particle size in the powder is 0.4 µm and crystallite size <100 nm. Magnetic properties of this nanostructured iron powder were investigated using vibrating sample magnetometer (VSM). The room temperature hysteresis loop showed ferromagnetic nature (approaching super paramagnetic) of the nanostructured iron powder having a coercivity of 14.54 Oe. The magnetic moment of the prepared powder was found to be, as per the formula, 3.75 µB as compared to normal iron powder 2.23 µB.*

Introduction

The properties of magnetic nanoparticles have been discovered extensively in the last few decades due to a large number of applications in the areas of medical science, and biology. [1,2] Magnetic nanoparticles are an important class of nanostructured materials proposing high potential as magnetic targeting drug delivery, high-density data storage media [3,4], high-resolution magnetic resonance imaging [5]. Compared with bulk structures, whose properties are well known, magnetic nanoparticles are complex and manifest a great diversity in their properties because the energies associated with the various physical parameters are comparable in the nanostructures. These parameters include the magnetocrystalline anisotropy energy [6], surface anisotropy energy [7] and thermal energy.

The preparation method influences the properties of nanoscale iron particles. Mostly chemical and physical methods are used to generate iron nanoparticles in the form of colloids as well as powders [8]. From the preparation point of view, one of the important subjects in the study of magnetic nanoparticles is the preparation of stable nanoparticles with novel properties.

A wide variety of techniques are being used to synthesize nanostructured materials including inert gas condensation, rapid solidification, electrodeposition, sputtering, and chemical processing. Mechanical attrition –ball milling which induces heavy cyclic deformation in powders, is a technique which has also been used widely for the preparation of nanostructured materials [9]. Unlike many of the above methods, mechanical attrition produces its nanostructures not by cluster assembly but by the structural decomposition of coarser-grained structures as the result of severe plastic deformation.

The reduction of mill scale to sponge iron powder is potentially a new way to take advantage of a cheap by-product of the steelmaking industry, yielding sponge iron that can be reused to the electric furnace as a metallic charge for steelmaking to obtain a product with a lower residual content and improved properties [10]. Other possible uses include the manufacturing of structural components from sponge iron

PREPARATION AND MAGNETIC CHARACTERIZATION OF NANOSTRUCTURED IRON POWDER FROM CARBOTHERMIC REDUCTION OF MECHANICALLY ACTIVATED MILL SCALE

powder, such as magnets and components for electric motors due to its superior magnetic properties.

In these studies, the nanostructured iron powder was prepared by carbothermic reduction of mechanically activated mill scale. (Mill scale contains both iron in elemental form and three types of iron oxides: wustite (FeO), haematite (Fe_2O_3) and magnetite (Fe_3O_4). The chemical composition of the mill scale varies according to the type of steel produced and the process used. The iron content is around 70% in the mill scale [11]. Magnetic properties of prepared nanostructured iron powder were evaluated using vibrating sample magnetometer (VSM) show that the ferromagnetic phase is present in the prepared sample. For the ferromagnetic phase, Fe particles show single domain magnetic structure as the coercivity of the nanoparticles decreases with the particle size decreases.

Experimental

The mill scale used in these investigations was procured from local industry. After separating the dust, dirt and non-magnetic impurities using a magnetic separator, the mill scale were screened to -100 mesh. Philips X' Pert Pro X- rays diffractometer was used to analyse the different types of oxides present in the raw material.

In these experiment mechanical activation of the mill scale (mixed with activated carbon in 5.7 : 1 as per stoichiometry ratio was carried out by milling it in laboratory attrition mill, having mill chamber and impellers made of stainless steel, under the following parameters: RPM – 350, grinding ball (hardened steel) dia- 10mm, ball to charge ratio- 10:1. Milling was carried out up to 60 hrs in an air atmosphere. Milling was interrupted at 20 hrs and 40 hrs to remove the sample for characterization. The activated mill scale powder prepared was tightly sealed in an alumina crucible. The sealed alumina crucible was put in a muffle furnace for reduction at 950°C for 24 hours.

XRD patterns of unmilled, milled and reduced powder were taken in the range of 20- 85° with Cu K_α radiation (λ = 1.54 A°). The morphology of the mechanically activated powders for a different time interval of 0 hrs, 20 hrs, 40 hrs, 60 hrs, were analysed by FESEM. Vibrating sample magnetometer (VSM) was used to measure the magnetic properties of the reduced iron powder. Magnetization (M) versus magnetic field (H) strength graph was plotted to find coercivity, saturation magnetization and remanence.

Results and Discussion

1   Mechanical activation

Morphology

The morphology of the mechanically activated powders for a different time interval of 0 hrs, 20 hrs, 40 hrs, 60 hrs, were analysed by FESEM as shown in Fig. 1. As milling hrs increases, a loss in initial morphology of the particles was observed, with the production of relatively fine particles that are rounded. The formation of finer particles in the nanometer range at these stages causes massive aggregation, as the interaction of particles is increased due to the high surface energy between the nanoparticles. It can be observed in Fig 1 (a-d) that the particle size of the mill scale powder is reducing as the milling proceeds.
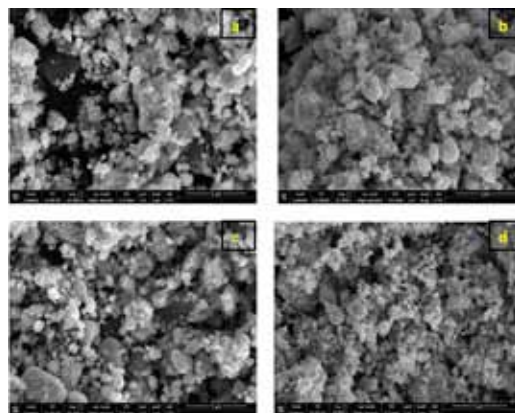
Fig 1: FESEM micrographs of Mill scale milled for (a) 0 hrs (b) 20 hrs (c) 40hrs (d) 60hrs

PREPARATION AND MAGNETIC CHARACTERIZATION OF NANOSTRUCTURED IRON POWDER FROM CARBOTHERMIC REDUCTION OF MECHANICALLY ACTIVATED MILL SCALE

Particle size analysis

The average particle size and size distribution of powder particles were analysed. The particle size distribution for all the samples are shown in Table 1 It is observed that with the increase in milling hours, the average particle size of the MA alloyed powder decreased. This is due to the intensive milling of powder for prolonged hours.

Table 1: Average particle size in the milled samples

S. No.	Milling Duration	Particle size (nm)
1.	Mill scale (as received)	1473
2.	20 hrs	1101
3.	40 hrs	650
4.	60 hrs	489

XRD studies

XRD patterns of milled samples were obtained and compared with JCPDE standard database, which confirms that the peaks obtained are of hematite, magnetite, wustite and iron (Fig. 2).
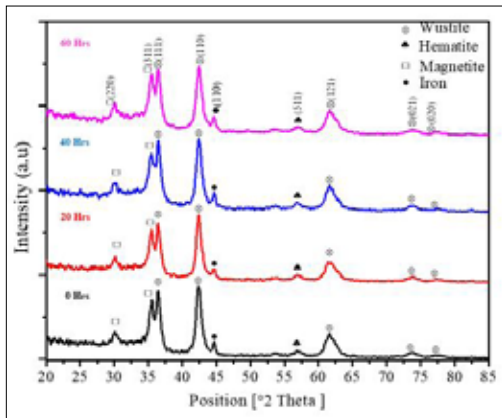
Fig 2: Comparison between the XRD patterns of mill scale powder milled for different hours i.e. 0 hrs, 20 hrs, 40 hrs, 60 hrs

Analysis by X-ray diffraction patterns (Fig. 2) shows the presence of hematite (Fe_2O_3), magnetite (Fe_3O_4), wustite (FeO) and iron (Fe) in the sample. Using Scherrer's formula, the crystallite size in the powder samples were calculated as listed in Table 2.

Table 2: Crystallite size in different powder samples

S. No.	Milling duration	Crystallite Size (nm)
1.	0 hrs	25.65
2.	20 hrs	19.32
3.	40 hrs	18.40
4.	60 hrs	15.88

2   Carbothermic reduction

XRD studies:

XRD pattern of the mill scale powder reduced at 950ºC for 24 h is shown in Fig. 3. Peaks corresponding to metallic iron, with minor impurities of wustite and hematite, confirm the reduction of the mill scale to sponge iron powder. During prolonged milling for 60 h, the collision between grinding media and the powder at high energy milling results in heat generation and the increase in powder surface energy due to the higher surface area of fine particles, and the presence of activated carbon results in the reduction of iron oxides at higher milling duration.

The crystallite size in the reduced iron powder using Scherrer's formula is found to be 15.77 nm.
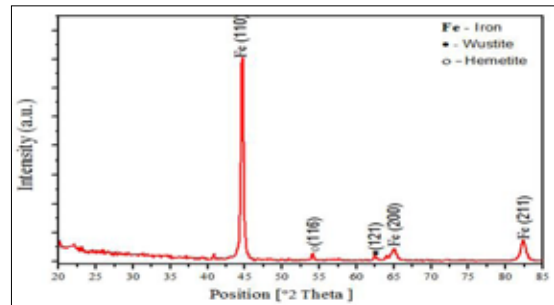
Fig 3: XRD patterns of reduced iron powder

Compositional Studies

The EDS analysis (Fig 4) shows that the sample is comprised of mostly metallic iron, with a small impurity of manganese which may present in the as-received mill scale.
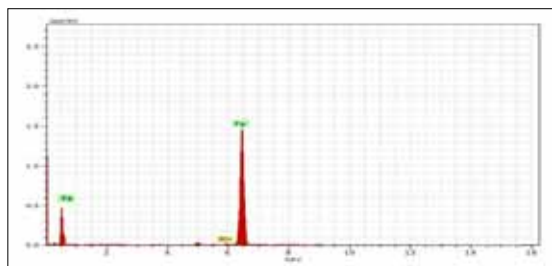
Fig 4: EDS Pattern of reduced iron

Morphology:

The morphology of the reduced iron powder was analysed by FESEM. Fig 5 shows the micrograph of reduced iron powder. FESEM images show that the mill scale reduction provided a sponge iron powder of an irregular morphology. The average particle size is around 0.4 μm in the prepared sponge iron powder (Fig. 6).
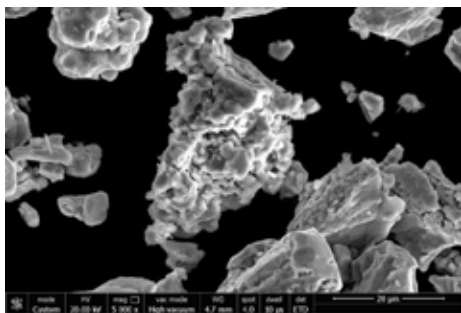
Fig 5: FESEM micrograph of the reduced iron powder
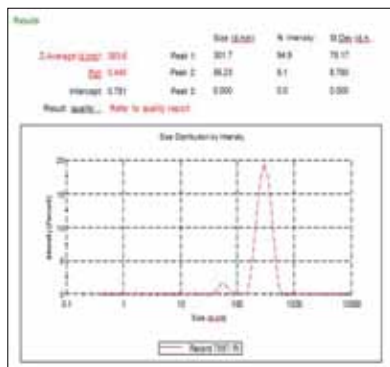
Fig 6: Particle size distribution for reduced iron powder

TEM studies

Fig 7 shows the TEM micrographs along with the SAED pattern for reduced iron powder, which clearly indicates that produced iron powder is nanocrystalline in nature. Lattice planes are clearly visible in the TEM micrographs.
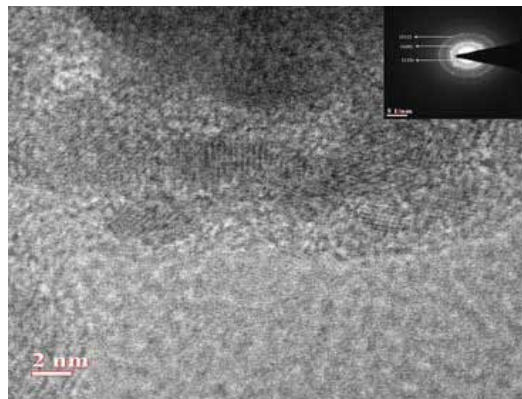
Fig: 7: TEM micrographs of reduced iron powder

3 Magnetic properties

Fig 8(a) shows the normalized magnetization, M, as a function of the applied magnetic field for reduced powder at room temperature. Fig 8(b) shows the normalized magnetization, M, as a function of the applied magnetic field for as received iron powder at room temperature. We have observed a clear ferromagnetic signal given that the M (H) curves show hysteresis. From these graphs, the coercivity for the sample was obtained. The coercivity of the reduced iron powder is 14.5366 Oe and that for as received iron powder is 58.4926 Oe. Comparison of these data shows that reduced iron powder is having less coercivity compared to as received powder which indicates that less hysteresis losses compared to as received iron powder. The coercivities measured are symmetric with respect to the magnetic fields.

The magnetic moment of the prepared powder as per formula is 3.752 μ_B as compared to iron

which has 2.227 µB. This increase in magnetic moment is an attribute of its nanostructured nature.
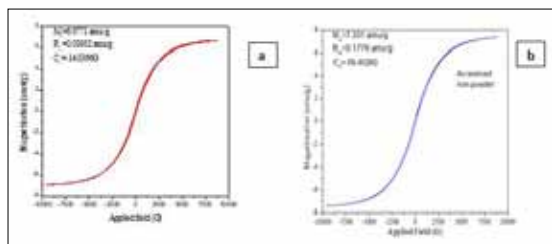
Fig 8: Magnetization curves measured at room temperature for (a) reduced iron powder (b) as-received iron powder

Conclusions

1. Mechanical activation of mill scale along with carbon as reductant resulted in intimate mixing and decreased reduction temperature of the carbothermic reaction to 950 ^{o}C which leads to providing nanostructured sponge iron powder.

2. Magnetic properties a studied show that the sponge iron powder obtained is ferromagnetic in nature (approaching to super paramagnetic) having a very low coercivity of 14.54 Oe.

3. The magnetic moment of the prepared powder per formula is 3.752 µB.

Acknowledgements

References

1. S. D. Bader, "Colloquium: Opportunities in nanomagnetism", Rev. Mod. Phys. 78 (1) (2006) 87.

2. D. Sander, "The magnetic anisotropy and spin reorientation of nanostructures and nanoscale films", Condens. Matter, 16 (2004) R603.

3. S. Rohart, C. Raufast, L. Favre, E. Bernstein, E. Bonet, and V. Dupuis "Magnetic anisotropy of CoxPt1−x clusters embedded in a matrix: Influences of the cluster chemical composition and the matrix nature", Phys. Rev. B, 74 (10) (2006) 104408.

4. C. Antoniak, J. Lindner, M. Spasova, D. Sudfeld, M. Acet, M. Farle, K Fauth, U. Wiedwald, H.-G. Boyen, P. Ziemann, F. Wilhelm, A. Rogalev, and S. Sun. "Enhanced orbital magnetism in Fe50Pt50 nanoparticles", Phys. Rev. Lett., 97 (11) (2006) 117201.

5. F. Zighem, and S. Mercone, "Magnetization reversal behavior in complex shaped Co nanowires: A nanomagnet morphology optimization", Journal of Applied Physics, 116 (19) (2014) 193904.

6. J. Sánchez-Barriga, M. Lucas, and F. Radu, "Interplay between the magnetic anisotropy contributions of Cobalt nanowires", Phys. Rev. B, 80 (18) (2009) 184424.

7. L. Berger, Y. Labaye, M. Tamine, and J. M. Coey, "Ferromagnetic nanoparticles with strong surface anisotropy: Spin structures and magnetization processes", Phys. Rev. B, 77 (10) (2008) 104431.

8. A. Alqudami, S. Annapoorni, S. Lamba, P. C. Kothari, and R. K. Kotnala, "Magnetic properties of iron nanoparticles prepared by exploding wire technique", Journal of Nanoscience and Nanotechnology, 7 (6) (2007) 1898.

9. C. C. Koch, "Synthesis of nanostructured materials by mechanical milling: problems and opportunities" Nanostructured Materials, 9 (1-8) (1997) 13.

10. L. Camci, S. Aydin, and C. Arslan: 'Reduction of ion oxides in solid wastes generated by steelworks', Turk. J. Eng. Environ. Sci., 26 (1) (2001) 37.

11. M. I. Martin, F. A. Lopez, and J. M. Torralba, "Production of sponge iron powder by reduction of rolling mill scale", Ironmaking & Steelmaking, 39 (3) (2012)155.

METHODS OF ACHIEVING HIGHER DENSITY BY ROOM TEMPERATURE AND WARM COMPACTION

Kalathur (Sim) Narasimhan

P2P Technologies, Moorestown, NJ, USA

Abstract: *Recently a technology was introduced for achieving higher densities by compaction at room temperature without heated tools. The concept depended on reducing the surface area of the powder that is compacted which helps in reducing the lubricant used without compromising ejection forces. The new technology is called low fines technology (LFT). LFT studies were extended to prealloyed molybdenum steels and compared with warm compaction technology. This technology can further enhance the density achieved by warm compaction technology, filling the need to close the gap between Double press double sinter and single press.*

Introduction:

Powder Metallurgy (PM) is the preferred metal working process with net shape capabilities, low energy and higher material utilization than the competing technologies such as castings, stampings, forgings and machining [1]. Over the past 60 years various technologies were developed in powder metallurgy that allowed conversion to PM parts with significant cost savings to end users.

The growth of powder metallurgy in automotive is closely linked to the ability of PM parts to be processed to higher densities. General trend in automotive engineering is to reduce weight of component by increasing) the strength of material without losing performance. The term power density is used to reflect increase in torque or performance by nearly 20% without increasing the weight of part [2]. This requires higher strength which can be achieved by increasing density. Fig.1 shows the effect of increasing density on the strength of a PM part for three different compositions [3].

Other benefits of higher density are improved ductility and higher fatigue endurance. Number of processes were introduced to achieve higher density over the years.
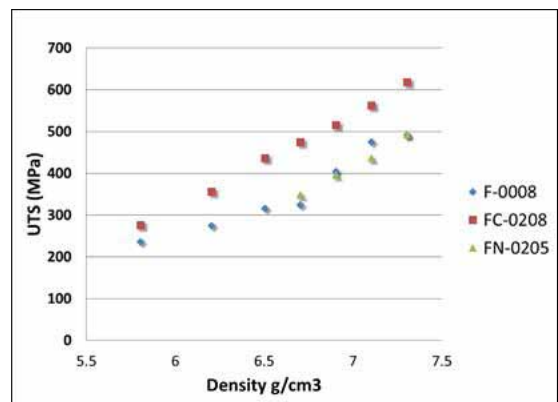
Fig.1. Effect of density on Ultimate tensile strength of common powder grades used for making PM parts.

Experimental:

The data collected in this publication were in conformance with MPIF standard test methods [4]. Laboratory work was performed to determine the powder characteristics, compressibility, and sintered mechanical properties. Powder flow and apparent density was determined using MPIF standard test methods (03 & 04). [7] Compressibility was determined using standard green strength bars. Sintering was done at 1120°C (2050 °F) for ~20 minutes at temperature in 90% nitrogen – 10% hydrogen atmosphere with conventional cooling.

TRS and tensile properties were determined using MPIF test standard methods (#41 and #10).

Results and discussion:

Series of trials were conducted to assess the effect of different particle size distribution on green density, green strength, sintered density sintered strength on FN-0205 containing 0.6% Kenolube mix compacted at 600 MPa and 800 MPa. Samples sintered at 1120C in 90N2-10H2 atmosphere with conventional cooling of about 0.9 degree per second. The data was collected on full distribution (see table 1, ref 5.), powder fraction of +100 mesh((149microns), +140 mesh (105 microns) and +325Mesh(44microns).

Table 1. Particle size distribution of Ancorsteel 1000B.

Sieve Distribution (w/o)

Micrometers	+250	-250 / +150	-150 / +45	-45
U.S. Standard Mesh	(+60)	(-60 / +100)	(-100 / +325)	(-325)
	Trace	12	67	21

Sieve Distribution /w/o/

We reported the results in detail in a previous paper (6), generally, +325 mesh (+44 microns) powder increases green density, green strength, sintered density Since the surface area of the powder is decreased by removing the-325 mesh (-44 microns) fines it should be possible to use lesser amount of lubricant. and achieve higher density. Decreasing the lubricant is not likely to affect ejection of compacted parts as the surface area is reduced by using +325 mesh powder. and hence reduced lubricant will, still provide lubricity. This technology is referred as low fines technology or LFT.Trials were conducted comparing full distribution Ancorsteel 1000B powder with 0.6%lubricant and LFT powder with 0.4 and 0.2% lubricant on Green and sintered density. results are shown in Table 2.

Table 2. Ancorsteel 1000B (Full distribution and LFT powder with 2%Nickel+0.6% graphite, compacted at 600 MPa and 800MPa at ambient temperature, sintered at 1120C in 90N2/10H2 atmosphere and normal cooled;

	Lube Wt.%	Powder Type	Green density (g/cm^3)	Sintered density((g/cm^3)	TRS (MPa)	D.C(%)	Hardness HRA
Compaction at 600MPa	0.6	Full distribution	7.16	7.17	936	0.09	43
Compaction at 600MPa	0.2	LFT powder	7.27	7.26	1004	0.16	45
Compaction at 600MPa	0.4	LFT powder	7.24	7.23	974	0.12	44
Compaction at 600MPa	0.6	LFT powder	7.17	7.19	913	0.12	43
Compaction at 800MPa	0.6	Full distribution	7.26	7.30	1002	0.13	46
Compaction at 800MPa	0.2	LFT powder	7.42	7.44	1162	0.20	48
Compaction at 800MPa	0.4	LFT powder	7.36	7.37	1073	0.17	47
Compaction at 800MPa	0.6	LFT Powder	7.28	7.31	1007	0.14	46

Table 2 illustrates the benefit of lowered lubricant on density. Lower lubricant is possible by reducing the fines. Based on part complexity and surface area the lubricant levels need to be adjusted.

Microstructure evaluation showed no laminations cracks at the reduced lubricant level of 0.2% and the pore distribution was uniform. Figure 2. shows the etched and as polished microstructure of 7.44 g/cm^3 density sample containing 0.2%lubricant with 0.6% lubricant sample at a density of 7.30g/cm^3.

We report in this paper work on prealloyed Mo powder FLN2-4405. We collected strip force (break load) after compaction. Strip force is static friction the parts experience in the die cavity after compaction. Lesser the static friction easier it is to eject the part from the die. Strip (ejection) forces were measured for the parts using load cells attached to the compaction die, Ejection characteristics of the lubricant system were compared to premix with 0.75% lubricant. Comparisons were done using a 25 mm tall

by 10 mm diameter round slug. Results are shown in Figure 3. The data is compared with full distribution powder with 0.75% Acrawax (EBS). Even at 0.2%lube LFT technology exhibits lower stripping forces than 0.75% Acrawax. Full distribution powder with 0.4%Acrawax is shown for comparison with 0.4% LFT powder showing the benefits of LFT technology for lower ejection forces.
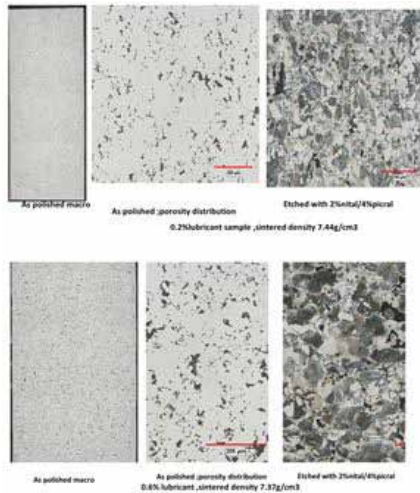
Figure 2. As polished and etched microstructure of FN-02025 with 0.2% (above)and 0.6% lubricant (below). Base iron powder is LFT powder.
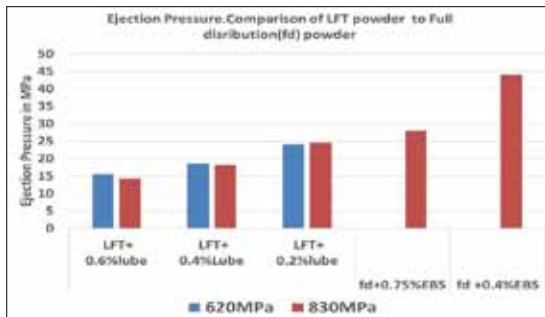
Figure 3. Strip(ejection) force for LFT technology with Full distribution powder

Figures 4 and 5 show the benefit of higher density realized using LFT technology in FLN2-4405 mixes.
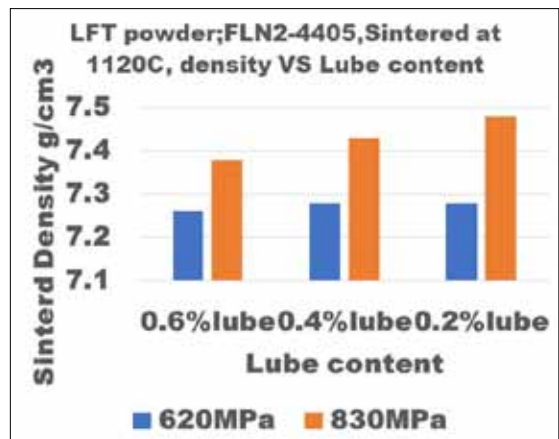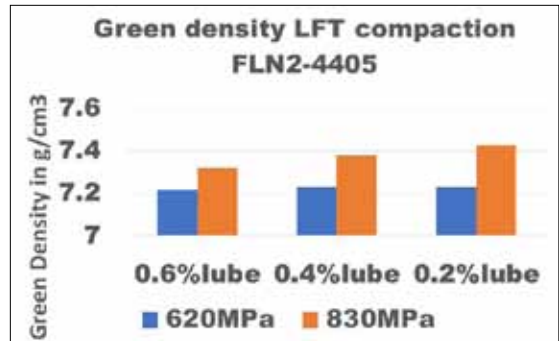
Figure 4. Green density and sintered density with various levels of lubricant content. LFT is low fine technology powder.
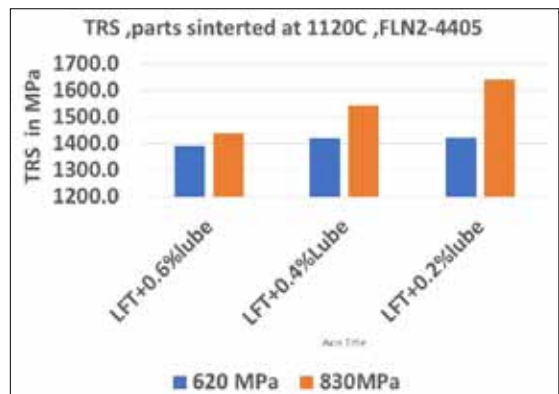
Figure 5. Sinterd transverse rupture strength using LFT technology.

Comparison with Warm Compaction technology:

In the 1990's it was discovered that when compaction of powders is carried out at elevated temperatures (up to ~300°C) density of the compacted part was higher than without heating, the higher the temperature the higher the density. At temperatures above ~250°C oxidation of the powder becomes an issue. Hoeganaes corporation introduced various products that enable compaction at 140°C (ANCORDENSE® [8-9], 60°C (AncorMax ®D) [10-11],92°C (AncorMax ®200) [12-13],160°C (ANCORDENSE ® 450),107°C (AncorMax ®225) [14].A review of these high-density process is discussed in [16]. Each of these products use different types of binders and lubricants that operate at maximum efficiency at the specified temperature to enable compaction to achieve density and ejection of the part. Part temperatures after ejection from the die tends to be higher, hence die temperature is kept below the optimum operating temperature of the specific grade. Comparison of the various high-density processes is shown in table 3. The aim is to lower the lubricant as low as possible without affecting the ejection pressure of the compact from the die after compaction. Warm compactions that requires powder and die heating has the maximum flexibility, field experience suggested powder heating is very inconvenient for most customers, although still widely used globally. The development of non-powder heating technology was a welcome change. This process relies on the heat transfer from the heated die to the powder during compaction. The powder away from the die wall may not be at the desired temperature if the mass is increased significantly, hence a limitation of part height and weight of 30mm or 1kg. respectively. One needs to consider the surface area of the compact as well. The major effort over the years is to reduce the lubricant to a minimum. AncorMax 225 achieved this objective with a lubricant content as low as 0.25%. (17). LFT technology is likely to enhance the density even further with warm compaction closing the current gap in density between double press and double sinter and warm compaction .

Table 3. Higher density compaction processes capabilities.

|	Warm Compaction ANCORDENSE®	Warm Die Compaction AncorMax®D	Warm Compaction ANCORDENSE®450	Warm Die Compaction AncorMax®200	Warm Die Compaction AncorMax® 225
Market Introduction	1994	2002	2006	2006	2012
Lubricant% (typical)	0.6	0.55	0.3-0.5	0.40	0.2-0.3
Powder Heating	YES	NO	YES	N0	NO
Powder Temp.	120-145°C	Not Required	135-165	Not Required	Not Required
Die Heating	Required	Required	Required	Required	Required
Part Temp	130-150°C	60-70°C	140-175°C	80-105°C	90-112°C
Density increase over 0.75% AcraWax at 700MPa Compaction	0.12g/cm^3	0.10g/cm^3	0.15g/cm^3	0.12g/cm^3	0.15g/cm^3
Green Strength at 700MPa (ref-0.75%acrawax - 13MPa)	25MPa	20MPa	30MPa	25MPa	35MPa
Ejection force at 830MPa Compaction	17MPa	26MPa	15MPa	27MPa	17MPa
Part Height limitation	Standard PM limits	20 mm	Standard PM limits	30mm	30mm

The above technologies helped the PM industry to achieve number of parts conversions globally.

In Figure 6 we show the ejection forces with various technologies. Preliminary work on combining LFT with warm compaction show lowered ejection forces at higher compaction force. LFT technology with warm compaction offers further opportunity to grow the business Further work is in progress.
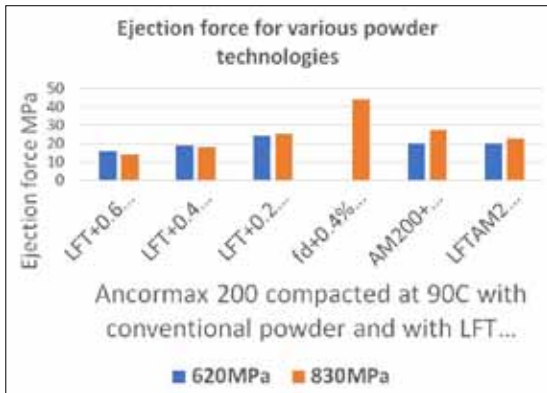
Figure 6. Strip (ejection) forces for some of the various technologies available.

Atomization technology development is necessary to minimize -the fines in the currently available atomized iron powders, Screening of the powder fraction to obtain LFT powder is not cost effective, Table 4, shows the relative cost of various processes and the projected cost of new technology developed. Utron process is a combustion driven process and high tonnage compaction is Toyota process (see ref 18)

Table 4: Rough estimate of relative cost of PM higher density processes

Relative cost	PM Process
1	Single Press and sinter
1,65	Double Press and Double sinters
1.5 to 1.8	Cu Infiltration
1.9to2.0	Powder Forging
1.4	Warm Compaction
1.2 to1.3	Warm Die Compaction
1.1to1.2	LFT
?	High Tonnage Compaction with warm die wall lubrication
??	UTRON, Combustion compaction

Conclusion:

Powder metal parts usage increases as higher density processes become available. The benefits of higher density using heated tools is an accepted process by many customers globally. Recent work on various sieve fractions of atomized iron powder suggest usage of LFT powder can yield higher density at room temperature compaction

and it is anticipated with the combination of warm compaction technology and LFT will provide means to reduce the lubricant further which will benefit increased density. The additional benefit will be reduced lubricant will make de-lubing easier during sintering.

References:

1. Kalathur S Narasimhan "New Products and Processes and the global Growth of Powder Metallurgy", Powder Metallurgy for Automotive and High-Performance Materials in Engineering Industries, Edited by P. Ramakrishnan, New Age International Publishers, New Delhi, 2012.PP 1-13

2. K.S. Narasimhan" Sintering of Powder mixtures and the growth of powder metallurgy", Materials Chemistry and Physics, Vol 67, Jan2001, PP56-65, Elsevier Publication, Updated with Industry shipments from MPIF and market research(unpublished)

3. Kim, General Motors Corporation Presentation, MPIF Conference Special Interest program, "Gears-Next Frontier", 2008 World congress.

4. R.J. Custom and T. Cimino," Machinability PM Steels" Powder Metal Technologies and Applications, ASM Hand book Vol 7. PP 671

5. Standard Test methods for Metal Powders and Powder Metallurgy Products, 2012, MPIF Princeton New Jersey.

6. Hoeganaes Corporation data Sheets; WWW. Hoeganaes.Com6.

7. Kalathur Narasimhan," Methods of achieving higher density in powder metal parts". Powdermet,2018, SanAntonio, MPIF Publication, Princeton New Jersey

8. S.H. Luk, H.G. Rutz and M.A. Lutz" Properties of Higher Density Ferrous P/M materials" International Conference on Powder Metallurgy and Particulate Materials, Toronto, 1994.MPIF Publication, Princeton New Jersey.

9. H.G. Rutz and F.H. Hanejko," High Density Processing of High-Performance Materials",

International Conference on Powder Metallurgy and Particulate Materials, Toronto, 1994.MPIF Publication, Princeton New Jersey.

10. *Ian Donaldson, S.H. Luk, Poszmik. K.S. Narasimhan" Processing of hybrid Alloys to High Densities" World Congress on Powder Metallurgy and Particulate Materials. Orlando, 2002, MPIF publication.*

11. *George Poszmik, Michael Marucci, K.S. Narasimhan" Single Press single Sintered P/M Products for High Performance Applications" World Congress on Powder Metallurgy and Particulate Materials, Vienna, 2004*

12. *F.G. Hanejko, G. Poszmik, P. King, and A.J. Rawlings, "Processing of PM Materials to a Density of 7.5 g/cm3 by Conventional pressing and Sintering, presented at Special Interest Program at PowderMet 2006 in San Diego, CA.*

13. *F.G. Hanejko, "High Density via Single Pressing/ Single Sintering, Euro PM2007, Toulouse, France, Vol. 3, p.15, published by European Powder Metallurgy Association.*

14. *F.G. Hanejko and S. Clisby, "A New Premixing and Compaction System to Achieve Green densities >7.4 g/cm3, presented at Special Interest Program at PowderMet2008 in Washington, DC.*

15. *F.G. Hanejko, W. Tambussi, and Jeanne Hooker, "Advances in Lubrication Technology in PM to Promote Higher Sintered Densities, presented at Special Interest Program at PowderMet2012 in Nashville, TN.*

16. *W. Brian James and K.S. Narasimhan" Warm Compaction and Warm Die compaction of Ferrous PM Materials" Powder Metallurgy association of India, Conference 2013*

17. *Gregory Falleur, Suresh Shah, Fran Hanejko, Sunil Patel "Production of High-Density PM components by warm die compaction Technology", World congress on Powder Metallurgy and Particulate Materials, Orlando,2014, Published by MPIF, Princeton, NJ,*

18. *M. Kondoh and H. Okajima: _ Advances in Powder Metallurgy & Particulate Materials (2002) 3-47–3-54.; Shin Tajima, Takeshi Hattori, Mikio Kondoh, Masaki Sugiyama, Kiyoshi Higashiyama, Hidefumi Kishimoto and Tadayoshi Kikko "Properties of High-Density Magnetic Composite (HDMC) by Warm Compaction Using Die Wall Lubrication"; Materials Transactions, Vol. 45, No. 6 (2004) pp. 1891 to 1894*

HIGH PERFORMANCE PREMIXES FOR VVT COMPONENTS MANUFACTURING

Vincent Paris[1], Philippe Francois[2], Andreas Buchmann[3]

[1] Rio Tinto Metal Powders, Canada
[2] Rio Tinto Iron and Titanium GmbH, Germany.
[3] Schunk Sintermetall technik GmbH (Thale), Germany.

Introduction:

As the pressure to develop more fuel efficient vehicles mounts, automakers are responding by embedding into their design more technologies leading to reduced fuel consumption[1][2]. One of such technologies is the Variable Valve Timing (VVT) system. While not an actually very recent innovation – it was initially developed in the 1960's – its use in engines is now extending to a large number of platforms. VVT systems can optimize fuel consumption by making slight adjustments to the timing of the opening and closing sequences of an engine intake and outtake valves at various operation regimes, hence optimizing combustion conditions[3]. To offset this timing, the cam shaft is made to rotate slightly when required by the onboard engine management system. This rotation of the cam shaft then affects the timing of the valve's opening and closing. This allows the engine to extract more energy from the same amount of fuel and become more efficient.

Parts for VVT systems can be broadly separated into two types: a rotor, which is attached to the cam shaft and the stator, which is fixed to the engine or the VVT assembly shown in figure 1. The rotor is allowed to shift within the stator by the pressure differential of the oil that is being fed to the system[4]. Both the rotor and stator are required to possess a high quality surface finish[5]. This is because, unlike a hydraulic cylinder, there is no gasket sealing off the chambers created by the vanes of the rotor within the stator. Surfaces must then be very straight, smooth and free of defects to allow the system to work flawlessly.
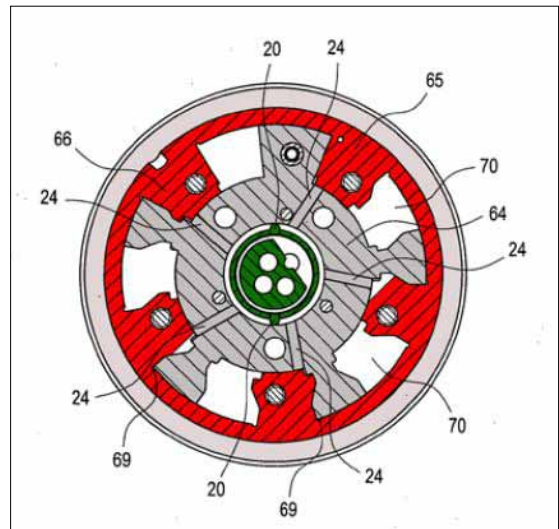
Figure 1. Schematic of a typical VVT stator and rotor assembly (Adapted from Hutcheson et al. (2009) [6])

Due to their shape and the high numbers of parts required, such parts are well suited to be produced using powder metallurgy[7]. Conventional manufacturing techniques would generate economically unsustainable levels of scrap. It follows that these requirements present an additional challenge for parts manufacturers. While powder metallurgy boasts a very high material utilization rate, producing parts that have very narrow tolerancesadds to the complexity of the process.

Development of premixes for VVT stators manufacturing

In order to respond to such challenges, powder premixes intended for the manufacturing of VVT stators should have properties that limit process

variability and perform at a higher level on an array of properties.

There a four main process steps that are involved in the manufacturing of VVT stators, namely: 1) powder compaction, 2) sintering, 3) sizing and 4) finishing operations [8]. In order to provide the best outcome possible (from a processing perspective) the powder feedstock needs to perform at its best in all four steps.

One of the most critical steps in the manufacturing process is the compaction of the green part. The compaction influences the other processing steps in several ways. Firstly, the thin-walled structure of a VVT stator makes it difficult to evenly fill the die cavity. Differences in the amount of powder being placed in the cavity prior to compaction will lead to in green density gradients across various sections of the part, further causing warping and dimensional change issues during sintering [9][10]. It is well know that in powder metallurgy, Fe-Cu-C systems will exhibit growth during sintering. This is due to copper and graphite dissolving into the iron matrix and occupying space in the lattice, forcing it to grow in size. Green density will impact the extent of that dimension change and if uneven, will cause anisotropic growth leading to warpage and deformation. Secondly, during the heating and cooling cycle, parts will exhibit thermal expansion and contraction. Thus, high dimensional precision can only be achieved by a good control of the dimensional behaviour from one part to the next. It follows that a powder premix exhibiting good die fill properties and evenly distributed additives will lead to a reduction in density gradients, thus greatly reducing some or the aforementioned problems.

Consequently, a powder premix containing a high performance lubricant was selected. A high performance lubricant is tentatively defined as a lubricant that will enhance lubrication at lower addition levels, improve green strength and

promotes better die fill [11].Table 1 shows some of the differences that can be expected between a regular powder premix and a premix lubricated with a high performance lubricant. Additionally, the particular shape of a VVT stator makes this type of part more difficult to lubricate compared to more traditional powder metallurgy parts. This is explained by the relatively small lubricant pool available in a thin-walled structure (high height-to-width ratio). Hence, as demonstrated in Figure 2, the improved lubrication offered by a high performance lubricant at the interface between the die wall and the part is expected to result in a better performance under industrial conditions. Stripping and ejection shear stresses are lower at higher compaction pressures for the high performance lubricant PR-2B, compared to a traditional EBS lubricant.

Table 1. Main physical properties for two typical FC-0208 premixes lubricated with a conventional EBS wax and the high performance lubricant PR-2B.

Premix lubricated with	Premix physical properties	
	Apparent density (g/cm^3)	Hall flow rate (s/50g)
PR-2B	3.05	35.5
EBS wax	3.03	38.4
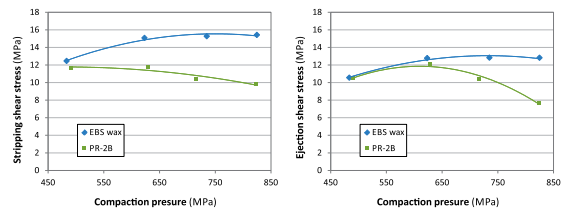
Figure 2. Ejection performance of FC-0208 powder premixes lubricated with the high performance lubricant PR-2B and conventional EBS wax.

Experimental Procedure

An ATOMET 1001HP premix was prepared by Rio Tinto Metal Powders especially for the compaction of VVT stators. ATOMET 1001HP is a highly compressible steel powder used in medium to high density applications. The premix included 0.7% w/w of a proprietary high

performance lubricant (PR-2B) developed by Rio Tinto Metal Powders. The premix contained 0.6% graphite (Timrex F-25, Imerys Carbon and Graphite, Switzerland) and 2.0% w/w powdered copper (165, Kymera International, Germany). It was prepared in a 15mt double-cone blender and compacted into VVT stators at SchunkSintermetalltechnik (Thale, Germany). Schunk Sinter Metals is a supplier of high precision powder metallurgy components for the automotive industry[12]. Table 2 shows the detailed composition of the premix.

Table 2. Composition of the powder mix used for the compaction of VVT stators at SchunkSintermetalltechnik.

Mix	Base powder	Graphite	Copper	Lubricant
B025D	AT-1001HP	0.6% Timrex F-25	2.0% Acupowder 165	0.7% PR-2B

The compaction of the VVT stator was performed on a Dorst TPA 250/3HP hydraulic press, equipped with a WC-Co die. The green parts were sintered in a Cremer sintering furnace under an endothermic atmosphere at 1120°C. Once sintered, as per the process described in the previous section, the parts were submitted to a sizing operation in order to adjust their final size with more precision.

The capability of the process was determined using the following procedure:

1. Evaluation of compaction capability (with respect to part weight);

2. Evaluation of sizing capability (with respect to sintered and sized part height);

3. Measurement of density variations across the part.

The process capability was determined using a statistical approach. A total of 50 consecutive parts were selected after each of the compaction and sintering steps. The height and weight of the green parts were measured using an SPC

software from the company Böhme + Weihs. For each of the distributions obtained, the probability mass function (PMF) was calculated, using Equation 1.

$$f(x, \mu, \sigma) = \frac{1}{\sqrt{2\pi\sigma}} e^{\frac{(x-\mu)^2}{2\sigma^2}} - \mu \qquad (1)$$

The distribution obtained from Equation 1 represents the probability, derived from production data that the part dimension (or weight) will end up at a given value. In order to make the data easily comparable, the targeted dimension is subtracted from the actual dimension, such that:

$$\Delta = x - t \qquad (2)$$

This yields a distribution that expresses the probability of the part dimension (or weight) to end up some distance away from the targeted measurement. In order to assess the density gradient throughout the part, a sintered part was sectioned in several portions, each taken from thinnest portion of the VVT stator. This location was selected due to the fact that it is the most difficult section to fill. Measurements were performed using the water immersion technique according to the standard DIN EN ISO2738. The geometry of the VVT stator throughout the various process steps was evaluated by measuring both the outer and inner diameter on a Zeiss coordinate measuring machine (CMM). In order to assess the deformation of the part, diameters were measured at several levels.

Results and Discussion

Process stability – Green and sized dimensions and green weight

The dispersion of the green part height is shown in Figure 3. The maximum probability occurs at +3μm from the specified height. This indicates that the average height of the compacted part is very well centered within the specified limits for this part. The actual tolerances are shown on the graph as LCL (Lower Control Limit) and UCL

(Upper Control Limit), which are respectively -50µm and +50µm. Standard deviation limits are also shown. The ±3σ range is well contained within the tolerance. Since compaction presses are typically driven on a position basis, a narrow distribution of part heights indicate that springback (the amount of elastic relaxation once pressure is removed on the part) is consistent. Coincidentally, springback is known to be well correlated with the green density, and, by corollary, to the die fill.

Figure 4. Adjusted normal density function for the green parts weight (grams).

Figure 3. Adjusted probability density function for the green parts height (mm).

Green weight data is shown in a similar graph in Figure 4. The highest probability for the part weight occurs at +0.075g above the targeted part weight. Similarly to the green part height, the ±3σ range is much smaller than the specification range. Actual green part weight tolerances (LCL and UCL) of -1.5g and +1.5g, respectively, are well shown on the graph. No sampled part exceeded the weight limits.

After sintering, VVT stators must be sized using a second pressing operation. This is done to correct potential distortion or warping that might have occurred during sintering. Sizing guarantees that all VVT stators are within the size requirements.

Figure 5. Adjusted probability density function for sized parts height (mm).

The probability density function for this parameter is shown in Figure 5. Similar to the green height, the most probable size height occurs at +3µm above the targeted height. Once more, the ±3σ range is well within the specified range. Tolerances for the sized part height are the same as for the green height, -50µm and +50µm.

Process capability – Green and sized dimensions and green weight

Statistics were derived from the parts sampled for the production (*n*=50) following compaction and

sintering. The capability metrics calculated were C_p and C_{pk} and the relative standard deviation. The C_p and C_{pk} values are calculated according to Equation 4 and Equation 5, respectively. These represent the process capability, that is, the capacity of an industrial process to produce within its tolerance limits. The C_p value assumes that the mean of the process is centered within the specification limits while C_{pk} does not.

$$C_p = \frac{UCL - LCL}{6\sigma} \qquad (3)$$

$$C_{pk} = min\left[\frac{UCL - \bar{x}}{3\sigma}, \frac{\bar{x} - LCL}{3\sigma}\right] \qquad (4)$$

Both the C_p and C_{pk} indices require that the data be normally distributed. Figure 3, Figure 4 and Figure 5 shown previously demonstrate the normality of the data. The distributions are however, not perfectly centered on the targeted value. This makes the C_{pk} parameter more accurate than the C_p value to assess the process capability. The relative standard deviation is calculated according to Equation 5 and represents the standard deviation in relation to the average measurement. It allows the comparison of the standard deviation metric as a dimensionless quantity without the distortion caused by differences in the average values.

$$relative\ standard\ deviation = \frac{\sigma}{\bar{x}} \times 100 \qquad (5)$$

Relative standard deviation, C_p and C_{pk} values are reported in Table 3.

Table 3. Process capability metrics obtained from the industrial production of the VVT stators.

Metrics	Parameter		
	Green height	Green weight	Sized height
Relative standard deviation (%)	0.044	0.14	0.049
C_p (dimensionless)	1.83	1.97	1.69
C_{pk} (dimensionless)	1.73	1.86	1.56

Process capabilities for all parameters are well above the required level of 1.67 (for C_p) and 1.33

(for C_{pk}). These values are standard requirements in statistical process control as well as for the automotive industry[13]. The powder premix used for the compaction of stators has a direct impact on the green metrics (sized dimensions are influenced by the sizing process rather than by powder feedstock). C_{pk} values for the green height and weight are well above 1.67, which indicates that the compaction of the stators is very stable and accurate.

Part geometry and density distribution

As mentioned in the introduction, part geometry and accuracy is an essential aspect of the manufacturing of VVT stators. In order to assess this variable, parts sampled at each stage of the process (post compaction, post sintering and finished parts) were accurately measured at various heights. The evolution of two critical measurements, the inner and outer diameters, is shown in Figure 6 for each process step
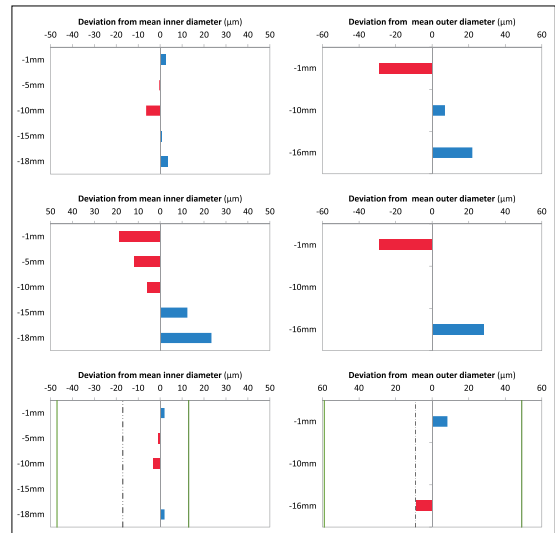
Figure 6. Variation in the stator dimensions for each process step: left column shows the inner diameter and right column the outer diameter. First row: as compacted; second row: as sintered and third row: final.

Following compaction, the inner diameter is 20µm to 30µm smaller than the tool size (ref. 1stFigure 6 row,). There is a geometric progression, as the top and bottom of the part have a very comparable and smaller inner diameter in comparison to the centre section of the part. The outer diameter is larger than the die size by 140µm to 190µm total. There is also a geometric progression on this diameter as the bottom portion of the part is wider than the top (the part has a conical shape). This can be explained by the springback that the part is experiencing post compaction, which is a known phenomenon[14].

Part distortion and warpage can occur during sintering, as the part goes through the heating and cooling cycles and as microstructure within the material develop. In a very homogeneous part, both in terms of additives distribution and density gradients, the dimensional change is highly isotropic, leading to little distortion. Since powder metallurgy parts are prone to density gradients (along the compaction axis but also the circumference of the part), some level of distortion is expected during sintering. The Fe-Cu-C system in powder metallurgy exhibits growth, leading to an increase in the inner diameter, which expands above the targeted final dimension. In this case, there is the presence of a geometric progression phenomenon (ref. 2ndFigure 6 row,), where the inner diameter is smaller at the top and gradually increases toward the bottom of the part, where it is greater than the average diameter. Similar observations were made about the outer diameter.

Sizing is meant to correct the part dimension post sintering in order to achieve the best tolerances. It is a theoretically simple operation, but requires the sintered part to fit appropriately within the sizing die. As shown in the last row of Figure 6, the final outer diameter is very close to the specified diameter, differing by only 8.5µm (one-sided, total 17µm) at the top, 4.5µm (one-sided, total 9µm) in the middle of the part and exactly on the specified size on the bottom section.

The initial distortion of the inner diameter following sintering was corrected and no geometric progression from the top to the bottom of the part was observed. After sizing, the inner diameter is constantly about 23µm larger (one-sided, total 46µm) than the specification. This difference is well within the allocated tolerances, especially considering that a diameter smaller than the one specified in the drawings is not allowed on such part. Understandably so, the VVT rotor could not rotate freely should the stator's inner diameter be too small to allow the rotor to fit within the inner diameter.

The final density was measured on three segments of the part and is shown in Table 4. The density is comparable on all three sections, indicating acceptable distribution of the powder within the die cavity.

Table 4. Distribution of the sized density in several segments around the circumference of the VVT stator.

Parameters	Segment		
	1	2	3
Density (g/cm^3)	7.08	7.06	7.06
Average density (g/cm^3)	7.07		
Standard deviation (g/cm^3)	0.01		
Relative standard deviation (%)	0.14		

Conclusions

While powder metallurgy is an excellent technology to produce VVT stators at an economical cost, it remains that the process to do so is not simple. Requirements in terms of geometrical and dimensional accuracy are adding complexity to the production process but are nevertheless required for VVT systems to perform flawlessly. Dimensional change and density gradients must be well controlled by the part manufacturer.

As the compaction of a green part is the first step in the powder metallurgy process, subsequent production operations are highly dependent on it

being as consistent and stable as possible. Failure to properly compact green parts can lead to defects that will not be possible to correct in a later process step. In achieving this delicate balance, powder producers can assist part manufacturers in selecting the best powder feedstock for their process. This is best achieved when a high level of collaboration can be established between the part producer and the powder manufacturer such that technical challenges can be addressed and solved in a structured way.

Acknowledgments

References

1. L. Cheah and J. Heywood, "Meeting U.S. passenger vehicle fuel economy standards in 2016 and beyond," *Energy Policy*, vol. 39, no. 1, pp. 454-466, 2011.

2. National Research Council, *Effectiveness and Impact of Corporate Average Fuel Economy (CAFE) Standards*, Washington, District of Columbia: National Academy Press, 202.

3. J. Dale, "Powder Metallurgy industry recognises VVT technology," Innovar Communications, [Online]. Available: http://beta.ipmd.net/news/000900.html?accept_cookies=1. [Accessed 12 May 2018].

4. M. Chermesnok, "Hydraulic Variable Valve Timing," Waterloo, 2016.

5. R. De Oro Calderon, "Miba Sinter Group: How a global PM producer is adapting to a changing automotive industry," *Powder Metallurgy Review*, vol. 7, no. 1, 2018.

6. J. D. Hutcheson, A. Knecht, D. Pohl, G. A. Barton, S. L. Nance and J. S. Cole, "Variable Valve Timing Device". United States of America Patent US 2009/0173297 A1, 9 July 2009.

7. D. Whittaker, "Economic considerations for powder metallurgy structural parts," DW Associates, [Online]. Available: http://www.pm-review.com/introduction-to-powder-metallurgy/economic-considerations-for-powder-metallurgy-structural-parts/. [Accessed 27 May 2018].

8. N. Igarashi, Y. Sonoda, R. Take and H. Terai, "High-Quality High-Productivity Manufacturing of," *SEI Technical Review*, no. 85, pp. 48-53, 2017.

9. E. Hjortsberg and B. Bergquist, "Filling induced density variations in PM compacts," *Powder Metallurgy*, vol. 45, no. 2, pp. 146-153, 2002.

10. R. M. German, *Powder Metallurgy & Particulate Materials Processing*, Princeton, New Jersey: Metal Powder Industries Federation, 2005.

11. L. Azzi, Y. Thomas and S. St-Laurent, "Lubricants for high-density compaction at moderate," *International Journal of Powder Metallurgy*, vol. 43, no. 6, 2007.

12. "Schunk Sinter Metals," [Online]. Available: http://www.schunk-sintermetals.com/en/company/about-us/. [Accessed 13 May 2018].

13. S. Steiner, B. Abraham and J. Mackay, "Understanding Process Capability Indices," Institute for Improvement of Quality and Productivity, Waterloo.

14. S. G. Selig and D. A. Doman, "Finite Element Simulation of the Compaction and Springback of Alumix 321 PM Alloy," *Journal of Applied Mathematics*, vol. 2015, p. 7, 2015.

NITRIDING PROCESSES OF FERROUS POWDER METALLURGY COMPONENTS

Zhi-dong Chen, Chong-xi Bao, Yang Cao

NBTM New Materials Groups Co., LTD, P. R. China

Abstract: *Ferrous PM components have good performance/cost ratio and are widely used in automobiles, home appliances and other industries. For more demanding applications, better hardness, wear resistance, and corrosion resistance of ferrous PM components are required. As an important surface treatment process, nitriding can improve the overall performance of ferrous PM components. This article describes nitriding processes of ferrous PM components, including plasma nitriding, gas nitrocarburizing, quench-polish-quench (QPQ), combined with the applications of nitriding in NBTM. The characteristics, advantages and disadvantages of those processes are discussed.*

Introduction

Ferrous PM components have good performance / cost ratio and are widely used in automobiles, home appliances and other industries. However, the inherent porosities decrease strength, ductility, wear resistance, corrosion resistance, and fatigue properties. As a thermochemical treatment process to improve surface properties, nitriding is suitable for ferrous PM parts, which can significantly improve surface hardness, wear resistance, corrosion resistance and fatigue strength [1-5]. Nitriding is generally a process that infiltrates nitrogen into the surface of parts at $500 \sim 600^{\circ}C$ (except plasma nitriding) to form a nitrogen-rich hardened layer. Compared with the high temperature quenching process, the nitriding temperature is lower, so the deformation of nitrided parts is very small. Nitriding is often used as the last step in powder metallurgy production process.

The nitrided layer of PM parts is mainly divided into a compound layer and a diffusion layer. The compound layer of ferrous PM parts with different nitriding processes is generally composed of γ'-Fe_4N and ϵ-$Fe_{2-3}N$ two-phase mixtures, but the contents are different [6,7]. Usually better properties of the nitride layer can be obtained with the addition of nitrogen-affinity alloying elements, such as Al, Cr, Mo, V,

Nb and Ti [8-10]. This paper briefly summarizes the principles, advantages and disadvantages of several commonly used nitriding processes in industry, including gas nitrocarburizing, plasma nitriding and quench-polish-quench complex salt bath nitriding (QPQ).

Gas Nitrocarburizing

Gas nitrocarburizing is a technology improved from gas nitriding. The obvious disadvantage of gas nitriding is that the treatment time is too long, which usually takes more than 30 hours. Although two or three stages gas nitriding processes greatly reduce the treatment time, it is difficult to meet the capacity of industrial mass production. Gas nitrocarburizing commonly used gas medium such as ammonia, urea, formamide and triethanolamine, which undergo thermal decomposition reaction at gas nitrocarburizing temperature, to produce active nitrogen and carbon atoms. Active nitrogen and carbon atoms are absorbed by the surface of the parts and then infiltrate into the surface by diffusion, obtaining a nitrocarburized layer. The hardness and brittleness of the nitrocarburized layer are lower than those of the nitrided layer. Gas nitrocarburizing temperature is generally $560 \sim 570$ $^{\circ}C$, at which the hardness of nitrided layer is the highest. The nitriding time is usually $2 \sim 3$ hours. More nitriding time contributes little to the depth of nitrided layer.

The technological operation of gas nitrocarburizing is simple and the equipment costs are relatively low. Nitrogen potential, temperature and cooling rate are easy to control and relatively stable. However, the gas is easy to enter the pores of ferrous PM components, which has some adverse influences, such as the embrittlement of diffusion zone and undesirable change of dimensions. Steam treatment is usually adopted to seal surface porosities and weaken the influences.

Figure 1 shows gas nitrocarburized rotor produced by NBTM. The metallographic of gas nitrocarburized rotor with pre-steam treatment is shown in Figure 2. The thickness of the compound layer is 12.52 μm and the surface microhardness is 424 ~ 435 $HV_{0.05}$. As shown, the compound layer has penetrated through the boundaries and interconnected pores towards the interior of the part. Strip nitrides are distributed along grain boundaries and pores in the diffusion zone. Figure 3 shows the metallographic of gas nitrocarburized rotor without pre-treatment. A large number of massive nitrides occur in the diffusion zone, which will cause material brittleness.

Figure 2. Metallographic of gas nitrocarburized rotor with pre-steam treatment
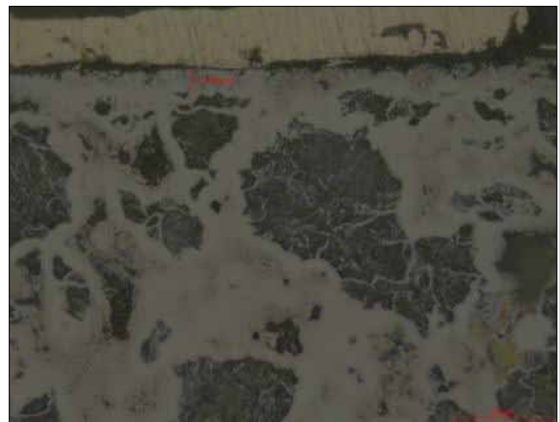
Figure 3. Metallographic of gas nitrocarburized rotor without pre-treatment

H. Fujikawa et al. have found that steel with a nitrided layer from nitrocarburizing had good corrosion resistance in the salt spray test [11]. Particularly, the steel with a nitrided layer of more than 10 μm showed obviously good corrosion resistance.

Plasma Nitriding

Plasma nitriding was invented by German B. Berghaus in 1932. During plasma nitriding, the components are connected with the cathode, and the furnace body is connected with the anode in

Figure 1. Gas nitrocarburized rotor produced by NBTM

the vacuum furnace. Hundreds of volts of direct current voltage is applied between the anode and the cathode to generate glow discharge, which ionizes the nitrogen-containing rare gas (such as ammonia) to form plasma. N+, H+ ions are accelerated in the cathode potential drop region, bombarding the cathode surface, activating the cathode surface, and a series of reactions occur. First, the kinetic energy of ion bombardment is converted into heat energy to heat the components. Secondly, due to the cathode sputtering, the Fe atoms on the surface of the components are bombarded and combined with the active N atoms (or N ions) near the cathode to form FeN deposited on the cathode surface. FeN is decomposed in turn: $FeN \rightarrow Fe_2N \rightarrow Fe_3N \rightarrow Fe_4N$, and active N atoms are produced simultaneously. Because of the high concentration difference between the surface and the inside of the cathode, the active N atoms diffuse to the core to form a nitride layer at a certain temperature.

Plasma nitriding has many characteristics that other treatment methods do not possess: The nitriding layer can be obtained at a lower temperature (e.g. 350 °C); The compound layer structure can be controlled accurately [8]; Energy and working gas can be saved greatly; It is easy to realize the impermeability of non-nitriding parts. However, shape and size of components are limited compared with other nitriding processes.

Figure 4 shows plasma nitrided small connecting rod produced by NBTM. The metallographic of plasma nitrided small connecting rod is shown in Figure 5. The compound layer (white layer) of the sample is about 6 ~ 7 microns thick. Because the nitrided parts are cooled in vacuum, the cooling rate is slow, leading to the precipitation of acicular in the diffusion layer. The compound layer is dense, with a small number of fine point-like micropores on the surface, which is closely bound to the matrix.

Figure 4. Plasma nitrided small connecting rod pro-duced by NBTM

Figure 5. Metallographic of plasma nitrided small connecting rod

The plasma nitriding temperature should not be too high, or porosities and channels will form in the compound layer [12]. Pores act as stress raisers and reduce the mechanical resistance of the nitride layer. By controlling the ratio of nitrogen and hydrogen in plasma nitriding, only γ′ phase can be obtained without ε phase in the compound layer. γ′ phase has good toughness and can reduce the brittleness of the compound layer. In plasma nitriding, hydrogen ions can reduce the surface nitrogen concentration and inhibit the formation of compound layers, especially the formation of high nitrogen ε phase. Hydrogen has a strong decarbonizing effect during plasma nitriding and forms a carbon-poor surface which is beneficial for the formation of γ′ phase.

A. F. Marcos et al. have studied the wear resistance of plasma treated PM parts [13]. Sintered ferrous alloy samples with plasma nitrided present better wear resistance than the untreated samples. And higher nitriding temperatures and times have a more favorable impact on the wear resistance.

Quench-Polish-Quench

Salt bath nitriding is a process in which CNO - decomposition in salt bath produces active nitrogen and carbon atoms, which infiltrate into the surface of parts to complete nitriding. Salt bath nitriding was initially used as a substitute for gas nitriding, but the application was limited since the strict requirement for wastewater treatment. With the development of salt bath formulation of trace cyanide, salt bath nitriding has begun to be used in industrial production again. The treatment of oxidation, polishing and re-oxidation after nitriding in salt bath is called quench-polish-quench complex salt bath process (QPQ). The process of QPQ is commonly as follows: pre-heating→ nitrocarburizing at 520 ~ 580 ^{o}C→ oxidation in an oxidation bath at 330 ~ 400 ^{o}C→ mechanical polishing→ re-oxidation in an oxidation bath. A dense Fe_3O_4 film is obtained on the surface of the parts, which can highly improve the wear and corrosion resistance of the surface due to its low friction coefficient and chemical stability. The nitrided layer beneath the oxide layer could improve the hardness and wear resistance of the surface [14,15].

The equipment cost of salt bath nitriding is relatively low. Since the new progress in pollution-free liquid nitriding process, there is no waste salt through the regeneration of salt bath itself.

Figure 6 shows salt bath nitrided valve produced by NBTM. The metallographic of salt bath nitrided valve is shown in Figure 7. The thickness of nitrided layer is 20 ~ 30 µm. The microhardness of nitrided layer is 1059 ~ 1203

HV0.1, while the microhardness of matrix is 560 ~ 692 $HV_{0.1}$. A certain amount of carbides are found in the matrix with the microhardness of 850-860$HV_{0.1}$.

Figure 6. Salt bath nitrided valve produced by NBTM
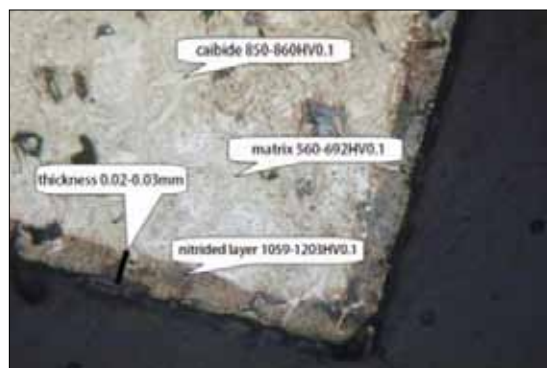
Figure 7. Metallographic of salt bath nitrided valve

The investigation of corrosion and wear resistance of QPQ treated PM parts was not yet presented in the literature. Wei Cai et al. studied the corrosion and wear resistance of 45 steel treated by QPQ treatment [16]. In the hot-water immersing tests, the initial rusting time for untreated samples is only around 10 min, while the initial rusting time for QPQ treated samples can reaching the maximum of 216h. In the wear tests, the weight loss of QPQ treated samples reaches minimum of 0.0029 g when the weight loss of untreated samples is 0.14 g.

Conclusions

Because of the limitation of PM technology, the porosity of sintered parts affects the performance and limits their applications. As described in this paper, nitriding processes including gas nitrocarburizing, plasma nitriding and quench-polish-quench can be used to improve the hardness, corrosion resistance and wear resistance of powder metallurgical materials. The nitrided layer with good compactness and reasonable thickness can be obtained by suitable nitriding processes. It is beneficial to the application of ferrous PM components.

References

1. Y. Lu, Y. B. Liu, Y. C. Zhang, et al. Investigation of Wear Behavior on Nitriding Sinter Metal Materials. Transactions of the Chinese Society of Agricultural Machinery, 2001, 5(32):100-102.

2. S. Dizdar, H. Grosser, U. Engström. Friction and wear characterization of sintered low alloyed chromium steels for structural components. Wear, 2011, 273(1):17-22.

3. A. Molinari, B. Tesi, T. Bacci, et al. Plasma nitriding and nitrocarburising of sintered Fe-Cr-Mo and Fe-Cr-Mo-C alloys. Surface and Coatings Technology, 2001, 140:251-255.

4. D. Grimanelis, T. S. Eyre. Sliding wear mapping of an ion nitrocarburized low alloy sintered steel. Surface and Coatings Technology, 2006, 201(6):3260-3268.

5. M. Campos, J. M. Torralba. Surface assessment in low alloyed Cr–Mo sintered steels after heat and thermochemical treatment. Surface & Coatings Technology, 2004, 182(2):351-362.

6. Y. Lu, Y. B. Liu, Z. M. Gao. Microstructure Analysis of Powder Sintering Nitride Layer. Automobile Technology & Material, 2004, 7:7-9.

7. S. Mansoorzadeh, F. Ashrafizadeh. The effect of thermochemical treatments on case properties and impact behaviour of Astaloy CrM. Surface & Coatings Technology, 2005, 192:231-238.

8. A. N. Klein, R. P. Cardoso, H. C. Pavanati, et al. DC Plasma Technology Applied to Powder Metallurgy: an Overview. Plasma Science and Technology, 2013, 15(1):70-81.

9. S. Q. Fang, M. T. Chen, J. J. Qu, et al. The Current Application Situation of Nitriding Technology and Nitriding Steel. Materials Review, 2014, 28:392-395.

10. Q. Y. Wang, Y. He, P. F. Zhang, et al. Research on Gas Nitro-carburizing Technique of Fe-based Powder Metallurgy. Material & Heat Treatment, 2009, 38(22):141-143.

11. H. Fujikawa, H. Iwamura, M. Uramoto. Corrosion Behaviour of Steel Nitrided and Nitrocarburized in Gas, Respectively. Defect and Diffusion Forum, 2015, 365:278-284.

12. S. Mansoorzadeh, F. Ashrafizadeh, X. Y. Li, et al. Plasma Nitriding of Low Alloy Sintered Steels. Transactions of Materials and Heat Treatment, 2004, 5(25):325-329.

13. A. F. Marcos, G. P. Ricardo, F. A. F. Pires, et al. Characterization of plasma nitrided layers produced on sintered iron. Journal of Materials Research and Technology, 2014, 3(3):210-216.

14. J. W. Lu, Q. Y. Wang, B. Zheng. Influence of QPQ Salt Bath Composite Processing on Microstructure and Property of a Certain Type Aviation Piston Engine Ring. Applied Mechanics and Materials, 2015, 751:26-29.

15. G. J. Li, Q. Peng, C. Li, et al. Microstructure analysis of 304L austenitic stainless steel by QPQ complex salt bath treatment. Materials Characterization, 2008, 59(9):1359-1363.

16. W. Cai, F. N. Meng, X. Y. Gao, et al. Effect of QPQ nitriding time on wear and corrosion behavior of 45 carbon steel. Applied Surface Science, 2012, 261(22):411-414.

MICROMIM - POWDER INJECTION MOLDING IN THE MICRO WORLD

Volker Piotter, Alexander Klein and Klaus Plewa

Karlsruhe Institute of Technology (KIT), Karlsruhe, Germany

Abstract: *High value-add products incorporating microscale features have already entered the market in a wide range of branches: Medical technology, IT, automotive, watch making just to name the most important ones. Many of these applications demand for materials with specific properties which cannot be provided by plastics or silicon and adequate large scale manufacturing processes are required as well. With respect to this constellation development of the so-called MicroPIM process for the fabrication of metal and ceramic micro components had been an obvious concern [1-4]. However, there are technological challenges to merge plastic injection molding, powder technology, and micro fabrication [5-11]. This article discusses the characteristics and process details of MicroMIM.*

MicroPIM Process Description

Materials

Manufacturing products having miniaturized structural details and good surface qualities requires powders of comparatively fine particle size for injection molding [8-12]. Small powder particle size also favors achieving high densities during sintering. Powders should allow high, homogeneous packing density to optimize sintering properties. Particle shape should be spherical, rounded, or at least equiaxed for good flowability and high packing density. Therefore, typical powders used for MIM are gas or, to a lower extend, water atomized, and , have a mean particle size ranging from lower than 5 to 20 µm for steel powders. Smaller particle size can be obtained by classifying if necessary. Common PM ferrous metals for MIM include 17-4PH and 316L stainless steels; nonferrous metals like copper [13], tungsten and tungsten alloys have already been added.

Powder cost are a crucial factor in manufacturing macroscopic PIM components, especially if fine rained, gas atomized fractions are required. However, in case of MicroMIM, part weights are significantly lower, so operating costs are usually more important than powder cost. Preventing powder agglomeration is crucial in both traditional PM and MicroMIM , as agglomerates have a detrimental effect on the processing behavior of powder fractions and on properties of the final parts. Agglomerates can be crushed during compounding when shear forces in the mixing process exceed the binding forces of the agglomerates. Therefore, co-rotating twin-screw extruders and shear roll compactors that provide high shear forces are recommended for feedstock production.

As with common MIM, a binder is used to help maintain the shape of green parts up to the onset of sintering. Several types of binder systems are used usually composed of several organic components to ensure meeting process requirements. Various organic substances, such as waxes (e.g., paraffin wax); thermoplastic materials such as polyethylene (PE), polypropylene (PP), polyoxymethylene (POM), and polyethylene glycol (PEG), as well as various additives to improve powder dispersion are combined to form a suitable binder system. In principle, binders used for MicroMIM must have the following properties:

- Good flowability, i.e., low viscosity over a wide shear rate range

- High strength to ensure dimensional stability during demolding and debinding

- Low de-mixing tendency

- Good wetting characteristics of the inorganic component

- Thermal stability at processing temperature

- Non-polluting characteristics; e.g., no contamination during debinding

Characteristics of the Injection Molding Step

Particular differences between the injection molding process for macro and MicroMIM must be taken into account [14]. Due to the extremely small dimensions of the manufactured parts and the high degree of tooling precision, special manufacturing methods are required to produce mold inserts.

A more comprehensive discussion of special methods for manufacturing microstructured mold inserts can be found in [6]. All design and process rules associated with macroscopic PIM must be considered to at least the same extent when dealing with micro dimensions. An interesting micro specific approach is described in [15].

Venting - MicroMIM tooling often does not allow conventional venting of the tool via venting gaps, because the dimensions of the microstructures are similar to those of the gaps. Sealing and evacuating the tool core solves this problem. In addition, evacuation avoids undesired material reactions occurring under pressure at high temperatures with the oxygen from enclosed air bubbles.

Channel diameters - Microcavities often show abrupt changes in channel diameters depending on the manufacturing method, increasing the risk of jetting and dead sector effects.

Binder segregation- The risk of powder binder segregation during injection is larger than in macroscopic MIM due to high aspect ratios comparable to the ratio of flow path to runner width.

Binder degradation - High aspect ratios expose the material to high shear forces, which can lead to decomposition and mechanical degradation of the organic binder system.

Feedstock supply - The amount of feedstock supplied for a part is usually very low depending on the type of tooling and the injection molding machine. However, parts with auxiliary features and long sprue gates require more material, which could require specialized equipment. Custom micro injection molding machines have been developed by companies like Sodick Co. Ltd., Japan, Wittmann Battenfeld GmbH, Austria, or Arburg GmbH + Co KG, Germany [16].

Temperature process conduct - Due to higher surface to volume ratios of micro-sized parts setting occurs much faster. Increasing injection speed can compensate for this only to a limited extent. In certain cases, Heating the core of the tool during injection $(T_{tool} \geq T_{g(feedstock)})$ avoids premature material setting in certain cases. Tools must be cooled during demolding. $(T_{tool} \geq T_{(feedstock)})$ to avoid deformation of the component. Heating and cooling the tool (the so-called variotherm process) results in longer cycle times (around 50 to 70 s) than typical cycles. Recently, it has been demonstrated that applying variothermal or dynamic temperization increases significantly geometrical accuracy of the MIM parts [17].

Demolding - The combination of high aspect ratios causing high friction/shear forces to act on the component with the relatively low green strength of molded parts require smooth, gentle demolding procedures.

Handling - Further processing and/or assembly of the small green components demands high precision and often requires special equipment. For example, it must be taken into account that single microparts sometimes stick to the gripper instead of falling down due to their light weight.

Debinding - Microparts inherently avoid large temperature and concentration gradients due to higher surfaceto-volume ratios, which should make debinding in parts with very small dimensions easier. However, certain

microfeatures like sharp diameter changes make it necessary to determine debinding parameters in MicroMIM as carefully as for macroscopic MIM.

Sintering - Sintering considerations for microparts are generally quite similar to those for macrostuctured parts, with the exception of the grain size of the final sintered parts. The grain size of microparts must be much smaller than that for macrostructured parts because a multicrystalline microstructure is required to obtain isotropic mechanical properties. This can be achieved by use of fine and even submicron-scale powders. Another approach is to use higher heating and cooling rates and to shorten peak temperature holding times. Grain growth inhibitors can also be used, but their effect on the entire grain structure must be taken into account.

Outlook

As described before extensive R+D activities have been accomplished [18-20], however, there are still challenges for further progress:

One point concerns the application of finer powders, e.g. in the range or even below 1 µm, to increase surface quality and detail replication performance. Further on improvement of powder preparation for defined adjustment of viscosity and sintering temperature represents a future task.

A further important topic relates to the reduction of failure rates in powder injection molding. This purpose usually requires modifications in all steps with a certain focus on the injection phase, where powder-binder segregation, which cannot be omitted completely, might cause distortions and/or defects. Early detection of failures in the green body (cracks, cavities, powder-binder segregation etc.), favorably on line immediately after the injection molding step, represents another technological challenge for the progress of MIM manufacturing.

Although (Micro-)MIM is obviously predestined for manufacturing complex shaped parts the final accuracies, may not be sufficient for all kinds of high value-added products [51,52]. Therefore, various attempts for improvement have been started, for example, holistic analysis of the parameters influencing part accuracies, the increase of the powder loadings, or the utilization of multi-modal powder fractions.

References

1. R.M. German: Medical and dental applications for microminiature powder injection moulding (microPIM) - a roadmap for growth. Powder Injection Moulding International, Vol. 3; Inovar Communications Ltd., 2009, pp. 21-9.

2. Yole Developpement, "Status of the MEMS Industry 2017". www.yole.fr, accessed March 2018.

3. R.M. German: Materials for Microminiature Powder Injection Molded Medical and Dental Devices; International Journal of Powder Metallurgy, Vol. 46, 2, 2010, pp. 15-18.

4. N. Williams: Metal Injection Moulding: Building on solid foundations in the medical sector. PIM International, Vol. 11, No. 1,2017, pp. 43-57.

5. F. Petzoldt: Micro powder injection Moulding – challenges and opportunities, Powder Injection Moulding International, Vol. 2, No. 1, Inovar Communications Ltd., 2008, pp. 37-42.

6. A.A. Attia, J.R. Alcock: A review of micro-powder injection moulding as a microfabrication technique. J. Micromech. Microeng. 21 043001, Vol. 4, 2011.

7. V. Piotter, T. Moritz: Micro Powder Injection Moulding: Processes, materials, and applications; Powder Injection Moulding, Vol. 9, No. 3(2015), pp. 63-70.

8. N. Muhamad, J. Rajabi, A.B. Sulong, A. Fayyaz, M.R. Raza: Micro powder injection moulding using nano sized powders. Trans Tech Publications Ltd., Vol. 1024, 2014, pp. 116-119.

9. A. Islam, N. Giannekas, M. Marhöfer, G. Tosello, H.N. Hansen: A Comparative Study of Metal and Ceramic Injection Moulding for Precision Applications., Proc. of 4M/ICOMM2015

Conference, Research Publishing, Singapore, ISBN: 978-981-09-4609-8 (2015), pp. 567-570.

10. J.P. Choi et al.: Analysis of the rheological behavior of Fe trimodal micro-nano powder feedstock in micro powder injection molding. Powder Technology 319 (2017), pp. 253-260.

11. J.W. Oh et al.: Influence of nano powder on rheological behavior of bimodal feedstock in powder injection molding. Powder Technology 311 (2017), pp. 18-24.

12. J. Rajabi, N. Muhamad, A.B. Sulong: Effect of nano-sized powders on powder injection molding: a review. Microsyst Technol, Vol. 18, 2012, pp.1941-1961.

13. B.S. Zlatkov, R. Hubmann: Tube type X-Cooler for microprocessors produced by MIM technology, Powder Injection Moulding International, Vol. 2, No. 1, Inovar Communications Ltd., 2008, pp. 51-54.

14. V. Piotter, A. Klein, T. Mueller, K. Plewa: Manufacturing of integrative membrane carriers by novel powder injection moulding. Microsyst Technol., 22 (2016), pp. 2417–2423.

15. A. Albers, T. Turki: Supporting design of primary shaped micro parts and systems through provision of experience. Microsyst Technol, Vol. 19, 2013, pp.471-476.

16. M. Maetzig, H. Walcher, U. Haupt: New Injection Moulding Equipment for PIM Microparts; Proc. Euro PM2011, Vol. 2, European Powder Metallurgy Association, Shrewsbury, UK, ISBN 978-1-899072-21-7 (2011), pp. 195-200.

17. M. Maetzig, H. Walcher, M. Bloemacher, S. Fleischmann: Production of MIM parts with a High Aspect Ratio; Proc. Euro PM 2017 - Powder Metallurgy Congress & Exhibition, 01.-05.10.2017; Published by EPMA, ISBN 978-1-899072-49-1.

18. H. Cho, J. Lee, S. J. Park: Fundamental Experiments for Fabrication of Copper Micro Heat Pipe by Powder Injection Molding. Proc PM2016 World Congress, Hamburg 09. - 13.10.2016, published on USB by EPMA, ISBN: 978-1-899072-48-4.

19. T. Osada: Control the Deformation of MIM Parts by the Powder Size Distribution. Proc PM2016 World Congress, Hamburg 09. - 13.10.2016, published on USB by EPMA, ISBN: 978-1-899072-48-4.

20. Xu Hui et al.: The Effects of Sintering Temperature on Micro-MIM Carbonyl Fe Parts. Proc PM2018 World Congress, Beijing 16. - 20.09.2018, published on USB by CSM and CPMA (2018) 637-645.

TWO MATERIALS POWDER INJECTION MOLDING (2C-PIM) OF STAINLESS STEEL 17-4PH-STAINLESS STEEL 316L POWDERS

**Najlaa Nazihah Mas'ood, Abu Bakar Sulong, Norhamidi Muhamad,
Intan Fadhlina Mohamed, Farhana Mohd Foudzi, Farrahshaida Mohd Salleh***

Department of Mechanical and Material Engineering,

Faculty of Engineering and Built Environment, Universiti Kebangsaan Malaysia, Selangor, Malaysia.

*Faculty of Mechanical Engineering, Universiti Teknologi Mara, UiTM Shah Alam, Selangor, Malaysia.

Abstract: *Two materials Powder Injection Molding (2C-PIM) is a recently developed method to manufacture functionally graded components. This study is focused on determining the suitability of two materials combined via experimental PIM technique by the sintering and microstructural evaluations. In addition, the shrinkage behavior between the two materials is also observed. The materials in 2C-PIM are said to be compatible with each other in terms of metallurgical bonding and responsive during the sintering process. The materials are stainless steels 17-4PH and 316L with palm stearin and polyethylene as the binders. It has been found that the difference sintering shrinkage for both materials is not significant due to the coefficient thermal expansion (CTE) between the two materials are quite similar. Therefore stainless steels 17-4PH and 316L can be combined successfully via the 2C-PIM technique.*

Introduction

Powder injection molding (PIM) is a powder metallurgy net shaping process that allows complex parts to be mass manufactured with metal, ceramic, or composite materials [1]. Such process consists of four main steps: mixing, injection molding, debinding, and sintering. These four steps are also practice in 2C-PIM or also can called as Co-PIM. However, the difference between PIM and 2C-PIM is during the injection molding step where 2C-PIM may be implemented in two ways either over-molding or co-injection molding [2]. In the over-molding, two different barrels are used to inject two different materials into a desired shape while co-injection molding is a functionally graded structure which produces the desired part using the flow behavior of materials through the same runner system while co-injection molding, it can produce a component that has a core and skin made of two different materials [2].

In this paper, dilatometry is used as an experiment method to determine the compatibility of two different materials for two metal powder injection molding. The co-sintering behavior can be identified and isolated from the shrinkage behavior. The two material systems exhibiting diverse characteristics are selected in order to identify and isolated the behavior. The objective of this experimental study was to assess suitable material systems for co-sintering process in powder injection molding. Not only can examine the most similar thermal shrinkage rate, the dilatometer study also was selected because of their capability to give favorable interfacial integrity after injection molding and co-sintering [2].

The concept of 2C-PIM is based on joining of the ceramic-metal composite in their green states and subsequently, obtaining the desired density through further processing which includes debinding and sintering. So far, various processing techniques utilizing interlayer material for joining have been established [3,4]. In these techniques, the disadvantage of inclusion of a third material different from the

base materials and additional manufacturing step are usually imposed [5]. Thus, direct joining of composites such as through 2C-PIM process ensures reduction in the process chain and complexity in addition to assembly cost savings.

Methodology

The two stainless steels; 17-4PH and 316L are mixed separately with a binder system consists of 60wt% palm stearin (PS) and 40wt% polyethylene (PE). PE helps in decreasing the viscosity of feedstock and increase the replication ability while PS is functioned as modifier to reduce the viscosity and yield stress of the mixture. Prior mixing, the critical powder volume percentage (CPVP) is conducted to determine the optimum powder loading for the feedstock using the Brabender mixer. Such optimum powder loading leads to feedstock stability that prevents the powder-binder separation. Each stainless steel is then mixed with the binder system separately at 150 °C for 1 hour using the same mixer.

The injection molding process is then conducted using the BOY Machine 22A. The co-injection molding variants are utilized in order to conduct the 2C-PIM technique. SS17-4PH feedstock is injected first followed by SS316L feedstock using the same barrel. For initial experimental work, the green part for each materials is produced first due to find the relevant parameters which can be used for 2C-PIM process.

However, before proceed with sintering process, the sintering shrinkage of the injected 2C-PIM is also compared with that of the injected single material produced by the same injection molding machine. Such comparison is needed for better evaluation regarding the thermal expansion mismatch due to two different materials. The debound part is then presintered using a dilatometer at 1200 °C and 5 °C/min in order to identify the shrinkage behavior for both materials. The dilatometer study is conducted by using vertical dilatometer Linseis Model for

each material. When the shrinkage percentage is identified, then the co-sintering process is continued. After all, the micrograph is observed through the SEM image.

Results and discussion

The moulding parameters are heavily interactive at any particular moulding condition, thus the solution to one problem can lead to a defect in another form. The critical parameters include; injection temperature, mould temperature, injection speed, injection pressure and cooling time. The injection temperature must typically be set above the melting point of the higher molecular binder or backbone binder. This temperature influences the viscosity of the melt and consequently the ability to fill the mould cavity. Too low temperature setting can result in flow lines evident on the part due to poor flow characteristics [6]. On the other hand, higher temperatures can cause blister effects. The mould temperature must also be set at a temperature below the melting point and recrystallization temperature of the lower molecular weight binder component or primary binder. The mould temperature affects the development of stresses, rate of cooling and filling of the mould cavity. Too low mould temperature can lead to incomplete filling of the part or other defects while higher mould temperatures can lead to blisters and flashing [6]. The injection speed is important to ensure the die cavity promptly fills in a short time while injection pressure drives the filling of the mould. Adequate cooling time is also essential for redistribution of internal stresses and consequently, satisfactory part.

The co-injected part of SS17-4PH/SS316L is shown in Figure 1. It is observed that both materials can be combined via 2C-PIM using the same injection molding parameters as used by the single material. In addition, no visible defects are observed on the surface of the injected green part.
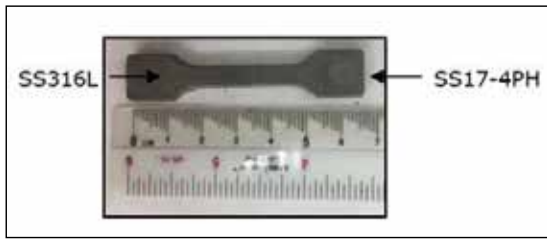
Figure 1. Green Part 2C-PIM

Conclusions

The components were defect free. 2C-PIM of SS17-4PH and SS316L was successfully injected where no visible defects on the surface were observed. Such success may achieved by the binder system that showed promising rheological properties as required in PIM. In addition, the mixing was conducted well where no powder-binder separation occurred due to the homogeneous mixture of the feedstocks. The suitable powder loading for SS17-4PH and SS316L are 72vol% and 64vol%, respectively. Dilatometer study also proved that both materials can be injected in 2C-PIM or Co-PIM process because the co-sintering process is successfully implemented without any defects.

Acknowledgement

References

1. Liu, Z. Y., Damon, K., and Schaffer, G.B. (2009). Powder injection moulding of an Al–AlN metal matrix composite. Materials Science and Engineering, A 513: 352-356.

2. D.F.Heaney, P.Suri, R.M.German. (2003). Defect-free sintering of Two Material Powder Injection Molded Components. Journal of Materials Science, 38(24): 4869-4874.

3. Jadoon, A., Ralph, B., & Hornsby, P. 2004. Metal to ceramic joining via a metallic interlayer bonding technique. Journal of Materials Processing Technology, 152(3):257-265.

4. Singh, M., Shpargel, T. P., & Asthana, R. 2008. Brazing of yttria-stabilized zirconia (YSZ) to stainless steel using Cu, Ag, and Ti-based brazes. Journal of Materials Science, 43(1):23-32.

5. Dourandish, M., Simchi, A., Tamjid Shabestary, E., & Hartwig, T. 2008. Pressureless sintering of 3Y-TZP/stainless-steel composite layers. Journal of the American Ceramic Society, 91(11), 3493-3503.

6. Heaney, D. 2012. Powders for metal injection moulding. Handbook of Metal Injection Molding, Woodhead Publishing Limited Cambirdge, pp. 50-63.

CHANGES IN MICROSTRUCTURES AND MECHANICAL PROPERTIES OF SELECTIVE LASER MELTED Al-10% Si-0.4% Mg ALLOY AFTER HOT ISOSTATIC PRESSING

Tomotake Hirata, Takahiro Kimura and Takayuki Nakamoto

Osaka Research Institute of Industrial Science and Technology, Osaka, Japan

Abstract: *We investigated the microstructures and mechanical properties of an Al-10%Si-0.4%Mg alloy fabricated by selective laser melting (SLM), before and after hot isostatic pressing (HIP). The influence of the internal porosity of the alloy on its mechanical properties was also investigated. Sub-micron-sized fine dendritic cell microstructures were formed in the as-built alloy. The strength and ductility of the as-built alloy decreased with increasing internal porosity. After HIP, the internal porosity of the alloy decreased; however, the strength of the alloy was significantly lower than that in the as-built state. This can be attributed to the microstructural changes that occur at elevated temperatures during HIP. The initial internal porosity had a relatively small effect on the strength of the alloy that had subjected to HIP. On the other hand, the ductility of the alloy improved significantly after HIP, while the ductility deteriorated with increasing initial internal porosity. Therefore, it is important to optimize the laser irradiation conditions when fabricating aluminum alloys by SLM.*

Introduction

Additive manufacturing (AM), otherwise known as 3D printing, is a layer-by-layer processing technology based on slice data prepared from 3D CAD data [1, 2]. AM has attracted considerable attention in recent years because it can be used to produce new functional parts on demand, as well as to fabricate customized complex 3D structures that would be impossible to fabricate using conventional manufacturing methods such as machining, forming, and casting. A type of AM fabrication, known as "selective laser melting (SLM)", can produce metal 3D objects from metal powders by stacking and then melting the powders, layer by layer, by laser heating. SLM can be used to produce materials with very fine microstructures, due to the very rapid solidification rate that is a feature of the SLM process (about 1×10^6 °C/s) [3]. The fine microstructures that can be produced using SLM enable the production of materials with excellent mechanical properties [4, 5].

SLM with aluminum powders is especially promising, because the low specific weight and high thermal conductivity of aluminum should enable the production of light-weight components and heat-control parts such as heat exchangers and heat sinks for the aerospace and automotive fields [6, 7]. Therefore, many researchers have examined the use of aluminum alloys with SLM [8-13]. However, it is easy for internal pores to form in aluminum SLM materials because the aluminum exhibits high thermal conductivity and poor laser absorption.

It is well known that the hot isostatic pressing (HIP) method can eliminate internal pores from a material. HIP is regarded as being very effective process as a post-SLM treatment because it is possible to retain the shape of the SLM material after the pressing. Therefore, many researchers have examined materials that have been fabricated by SLM and then subjected to HIP [14-20]. However, the SLM material is heated at high temperatures for an extended duration during HIP, so knowledge of how heat treatments, a frequently used industrial process, change the microstructures and mechanical properties of SLM materials is also required. However, the

CHANGES IN MICROSTRUCTURES AND MECHANICAL PROPERTIES OF SELECTIVE LASER MELTED Al-10% Si-0.4% Mg ALLOY AFTER HOT ISOSTATIC PRESSING

influence of HIP on the microstructure of SLM aluminum alloys has not yet been clarified. In the present study, we fabricated AlSi10Mg specimens by SLM and investigated the microstructures and mechanical properties of these as-built SLM alloys as well as those after being subjected to HIP.

Experimental procedure

Specimens were fabricated using an EOSINT M280 SLM machine equipped with an Yb fiber laser (maximum power: 400 W, beam spot diameter: approx. 0.1 mm, wavelength: approx. 1.07 μm). The specimens were fabricated from a gas-atomized powder of Al-10% Si-0.4%Mg aluminum alloy obtained from EOS GmbH. The powder particles had a mean diameter of 25.6 μm and a near spherical shape.

Cylindrical (diameter: 7 mm, height: 55 mm) specimens were fabricated in an argon atmosphere (residual oxygen concentration of approx. 0.1%) under two laser-irradiation conditions. The first was the optimum laser-irradiation condition, which produces the highest relative density (laser power: 300W, scan speed: 1200 mm/s, scan spacing within ranges: 0.15 mm, layer thickness: 0.03 mm) [21]. The second laser-irradiation condition featured a low energy density, relative to the optimum condition. This was adopted to enable the investigation of the influence of the porosity. Table 1 lists the relative densities of the two materials. Sample A was fabricated under the optimum conditions and sample B was produced with the low energy density. The relative density of sample A was almost 100%. On the other hand, that of sample B was lower at about 98%. The stacking direction corresponds to lengthwise direction of the bar and the laser-scanning pattern was rotated through about 67° for each layer, as shown in Fig.1. Before starting the SLM process, the base

plates (A5083) were pre-heated to 35 °C using a heater placed inside the building platform.

Table 1. Relative density of as-built SLM specimens fabricated under the optimum (sample A) and low energy density (sample B) laser irradiation conditions.

Specimens	Laser irradiation conditions	Relative density (%)
Sample A	Optimum	99.96
Sample B	Low energy density	97.99
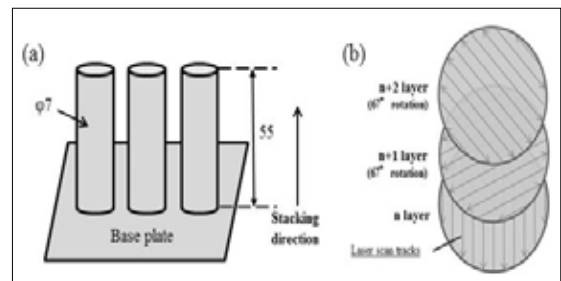
Fig. 1. Schematic illustrations of (a) stacking direction and (b) laser scanning pattern of SLM specimens

Microstructural observations were carried out by field emission electron microscopy (JEOL JXA-8530F). The microstructures were observed in horizontal and vertical cross-sections (perpendicular and parallel to the stacking direction, respectively). Prior to the observations, the cross-sections were etched using Keller's reagent. The micro-hardness was evaluated using a Vickers hardness tester (Mitutoyo HM-200) in the horizontal cross-section. In addition, three-point bending tests were carried out to evaluate the mechanical properties of the SLM specimens. Figure 2 shows the bending test to which the specimens were subjected. The cylindrical specimens were placed in the jig and then the indenter was pressed into the material by the universal material testing machine (SHIMADZU UH-100kNXR). The span length was 50 mm and the diameter of the indenter was 12 mm.

The HIP treatment was conducted using a HIP machine made by Kobe Steel Ltd. The duration of the HIP treatment was 2 h, using a pressure of 100 MPa and a constant temperature of 500 °C. Note that the specimens were not sealed inside a leak-resistant container before HIP. The internal pores were investigated by applying a high-resolution 3D X-ray computed tomography (CT) scanner (TOSCANER-32300μFD) to the mid-section of the cylindrical specimen. The X-ray tube voltage and tube current were 200 kV and 50 μA, respectively. Under these conditions, the spatial resolution was 8 μm. The CT data were analyzed using the Volume Graphics myVGL 2.2 analysis software.
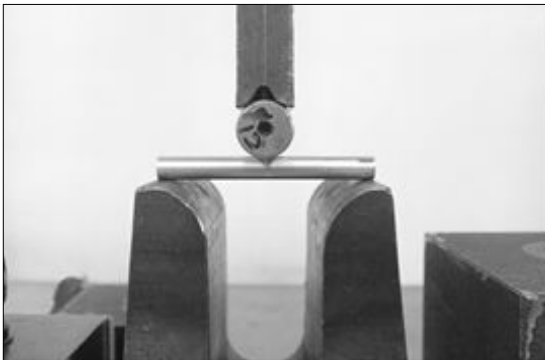

Fig. 2. Bending test of SLM specimen.

Results and discussion

1. Microstructural features before HIP treatment

Figures 3 and 4 show microstructural SEM images of the etched (a) horizontal and (b) vertical cross-sections of samples A and B, respectively, prior to HIP treatment. Fine dendritic cell microstructures of sub-micron size were observed for the horizontal cross-section (a) while elongated cell microstructures along the stacking direction (i.e., the direction of the heat flow) were observed for the vertical cross-section (b) of both materials. However, the

cell size of sample B was smaller than that of sample A.

These fine cell microstructure configurations are specific to the SLM process and were formed in response to the instant melting and rapid solidification of the powder during laser irradiation [5, 21-23]. It was suggested that sample B had higher cooling rate than sample A because a laser irradiation of lower energy density was applied to sample B than that applied to sample A. It is assumed, therefore, that the cell size of sample B was smaller than that of sample A.

Fig. 3. Microstructural SEM images of etched (a) horizontal and (b) vertical cross-sections of sample A prior to HIP treatment. The stacking direction corresponds to the longitudinal direction in (b).

Fig. 4. Microstructural SEM images of etched (a) horizontal and (b) vertical cross-sections of sample B prior to HIP treatment. The stacking direction corresponds to the longitudinal direction in (b).

Figure 5 shows a 3D visualization of pores as captured by X-ray CT scans of samples (a) A and (b) B prior to HIP treatment. The black areas in the scans correspond to the internal pores. For sample A, there were few pores in the specimen and the sizes of those pores were very small (<

100 μm). These pores are assumed to be caused by residual gas porosity or a lack of fusion defects. On the other hand, a large number of pores were observed in sample B, with the sizes of the pores being larger than those in sample A. It is assumed that the presence of internal pores influences the mechanical properties of sample B.
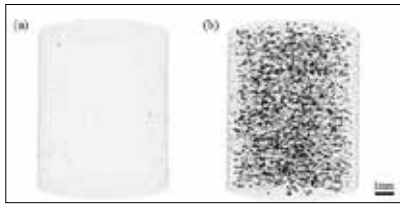
Fig. 5. 3D visualization of pores (black) as captured by X-ray CT scans of samples (a) A and (b) B prior to HIP treatment.

2. Microstructural features after HIP treatment

Figure 6 shows a 3D visualization of pores as captured by X-ray CT scans of samples (a) A and (b) B after HIP treatment. There are fewer internal pores were in both specimens. Especially for sample B, a few pores were observed only near the surface because the specimen was not sealed, and thus, the pores opened to the surface could not be pressed during HIP treatment, despite there being many pores in the as-built specimen. Thus, sample B would be expected to exhibit good mechanical properties.

Figures 7 and 8 show microstructural SEM images of the etched (a) horizontal and (b) vertical cross-sections after the HIP treatment of samples A and B, respectively. The microstructures were found to have changed drastically in both specimens. In addition, no major differences were observed between samples A and B, and the microstructures in the vertical cross-sections exhibited a tendency similar to that observed in the horizontal cross-sections. The microstructural changes were generated by the Si diffused and agglomerated into the granular precipitated phase of less than 5 μm size. Li et

al. [24] reported that the Si phases grew and that the number of Si phases decreased when AlSi12 SLM specimens were heated to a temperature of 500 °C, leading to reduced tensile strength and enhanced ductility due to the microstructural change. It is therefore suggested that the microstructural change caused by the HIP treatment strongly influenced the mechanical properties.

Fig. 6. 3D visualization of pores (black) as captured by X-ray CT scans of samples (a) A and (b) B after HIP treatment.

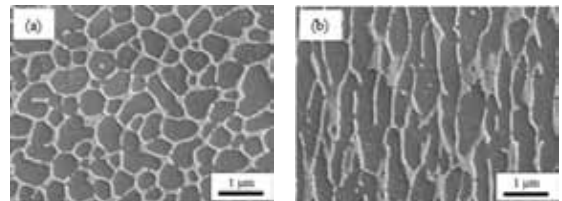*Fig. 7. Microstructural SEM images of etched (a) horizontal and (b) vertical cross-sections of sample A after HIP treatment. The stacking direction corresponds to the longitudinal direction in (b).*
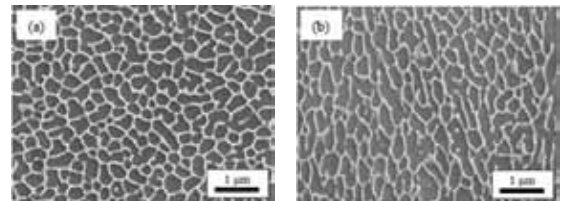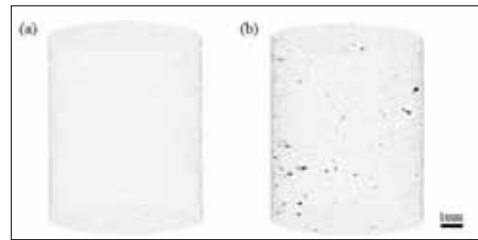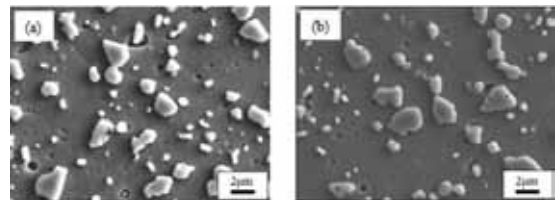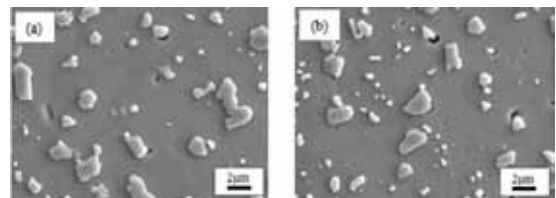

Fig. 8. Microstructural SEM images of etched (a) horizontal and (b) vertical cross-sections of sample B after HIP treatment. The stacking direction corresponds to the longitudinal direction in (b).

3. Mechanical properties of the as-built specimens and those after HIP

Table 2 lists the results of the micro-Vickers hardness tests for samples A and B, both as-built and after being subjected to HIP. Before the HIP treatment, the hardness was very high, at about 130 HV, for both specimens, although that of sample B was slightly higher than that of sample A. This is thought to be caused by the microstructure of sample B being finer than that of sample A. After the HIP treatment, on the other hand, the hardness of both samples decreased significantly as a result of the change in the microstructure. The measured hardness was about 50 HV with there being no remarkable difference between the samples A and B.

Table 2. Results of micro-Vickers hardness tests for samples A and B, both as-built and after HIP.

Type of specimen	Sample A (as-built)	Sample B (as-built)	Sample A (after HIP)	Sample B (after HIP)
Hardness (HV)	127	134	51.3	54.1

To evaluate the strength and ductility of the specimens, three-point bending tests were carried out. Figure 9 shows the load-displacement curves for the three-point bending tests performed on samples A and B, both as-built and after being subjected to HIP. In addition, Fig. 10 shows the appearances of the specimens after the three-point bending tests. Although, in the hardness tests, only a slight difference was noted between samples A and B, very large differences were observed in the three-point bending tests. The maximum load that could be applied to the as-built specimens was much higher than that which could be withstood by the specimens that had been subjected to HIP. However, the ductility of the as-built specimens was much lower than that of the specimens subjected to HIP. Ma et al. [25] reported on the effects of annealing on the mechanical properties of AlSi20 SLM specimens, whereby the ultimate tensile strength and breaking elongation changed from 506 MPa and 1.6% in an as-built specimen to 252 MPa and 8.7%, respectively, in a specimen annealed at 400 °C. This trend was very similar to the results of the present study. In addition, the maximum load and ductility were found to be dependent on the porosity prior to the HIP treatment. The maximum load that could be applied to as-built sample A was much higher than that which could be applied to sample B. However, after the HIP treatment, the difference between the maximum loads for samples A and B was relatively small. On the other hand, the ductility of the as-built sample A was much higher that than that of sample B. Moreover, the most important result was that, after the HIP, the ductility of sample A was higher than that of sample B. These results indicate that HIP treatment could improve the ductility of the specimen but is not an effective means of eliminating the internal pores in SLM specimens perfectly.

It has been suggested that the dominant mechanism leading to the elimination of the internal pores during HIP is diffusion bonding. It is well known that, in aluminum, diffusion bonding is difficult because there are stable oxide scales on the surface [26]. On the other hand, the diffusion bonding of titanium is relatively easy because the oxide scales disappear during diffusion bonding. In fact, Wu et al. [27] reported that the mechanical properties, such as the fatigue properties, improved significantly as a result of applying HIP treatment to SLM titanium alloy. In short, it is assumed that it would be very difficult to eliminate internal pores of SLM aluminum alloy by the HIP treatment. Therefore the mechanical properties of an aluminum SLM specimen with a high porosity, subjected to HIP treatment, are inferior to those of a sample with low porosity. Therefore, a method for eliminating internal pores should be developed in the future, ensuring optimization the laser irradiation conditions, when fabricating aluminum alloys by SLM in the present circumstances.
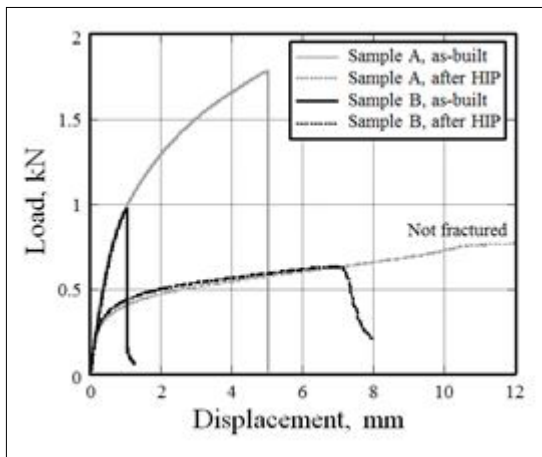
Fig. 9. Load-displacement curves of three-point bending tests for samples A and B, both as-built and after HIP.
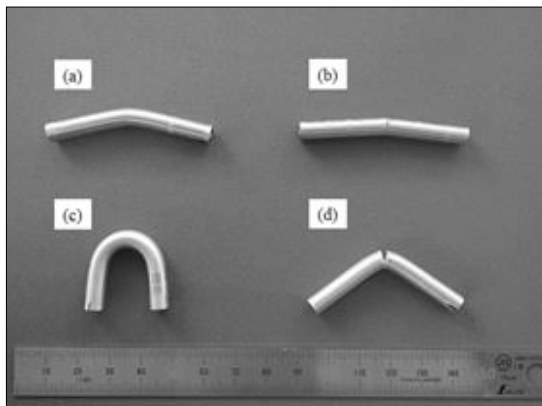

Fig. 10. Specimens after three-point bending test: (a) sample A of as-built; (b) sample B of as-built; (c) sample A after HIP; (d) sample B after HIP.

Conclusions

In the present study, we prepared AlSi10Mg alloys by SLM, after which the influences of an HIP treatments and the internal porosity were investigated. Fine dendritic cell microstructures of sub-micron size were observed in the as-built specimens. The cell size decreased with the energy density of the laser irradiation, such that the hardness of the specimen produced with the low energy density was slightly higher than that produced under the optimum conditions. However, the strength and ductility of the specimen produced with the low energy density was low because the internal porosity was high. After the application of HIP, the number of internal pores in the specimens was reduced. However, the Si was diffused and agglomerated into coarse granular phases. The hardness and strength of the specimens subjected to HIP decreased significantly owing to the resulting changes in the microstructure. On the other hand, the ductility of the specimen subjected to HIP improved significantly. However, the initial internal porosity had a significant effect on the ductility of the specimen subjected to HIP, with ductility deteriorating with an increase in the initial internal porosity. Therefore, optimization of the laser irradiation conditions is imperative for aluminum SLM alloy fabrication.

Acknowledgments

References

1. I. Gibson, D.W. Rosen, B. Stucker, *Additive Manufacturing Technologies*, New York, Springer, 2010.

2. W.M. Steen, J. Mazumder, *Laser Material Processing*. 4th ed., Springer, New York, 2010 349–369.

3. W.M. Steen, J. Mazumder, *Laser Material Processing*. 4th ed., Springer, New York, 2010 309–317.

4. T. Nakamoto, N. Shirakawa, Y. Miyata, H. Inui, J. Mater. Process. Tech., 209 (2009) 5653–5660.

5. A. Takaichi, N.T. Suyalatu, N. Joko, N. Nomura, Y. Tatsumi, S. Migita, H. Doi, S. Kurosu, A. Chiba, N. Wakabayashi, Y. Igarashi, T. Hanawa, J. Mech. Behav. Biomed. Mater., 21 (2013) 67–76.

6. W. Matthew, S. Tsopanos, J. Chris, O. Leuan, Rapid Prototyp. J., 13 (2007) 291–297.

7. T. Vilaro, S. Abed, W. Knapp, Proc. 12th European Forum Rapid Prototyp., AFPR, Paris, 2008.

8. *T. Kimura, T. Nakamoto, Mater. Design, 89 (2016) 1294–1301.*

9. *T. Kimura, T. Nakamoto, M. Mizuno, H. Araki, Mater. Sci. Eng. A, 682 (2017) 593-602.*

10. *T. B. Sercombe, G. B. Schaffer, Science, 301 (2003) 1225-1227.*

11. *T. Kimura, T. Nakamoto, Mater. Trans., 58 (2017) 799-805.*

12. *N. Read, W. Wang, E. Khamis, M.M. Attallah, Mater. Design, 65 (2015) 417–424.*

13. *E. Brandl, U. Heckenberger, V. Holzinger, D. Buchbinder, Mater. Design 34 (2012) 159–169.*

14. *S.L. Lu, H.P. Tang, Y.P. Ning, N. Liu, D.H. StJohn, M. Qian, Metall. Mater. Trans. A, 46A (2015) 3824-3834.*

15. *N. Perevoshchikova, C.R. Hutchinson, X. Wu, Mater. Sci. Eng. A, 657 (2016) 371–382.*

16. *M.W. Wu, P.H. Lai, Mater. Sci. Eng. A, 658 (2016) 429–438.*

17. *B. Ruttert, M. Ramsperger, L.M. Roncery, I.L. Galilea, C. Körner, W. Theisen, Mater. Design, 110 (2016) 720–727.*

18. *A. Röttger, K. Geenen, M. Windmann, F. Binner, W. Theisen, Mater. Sci. Eng. A, 678 (2016) 365–376.*

19. *H.P. Tang, J. Wang. C.N. Song, N. Liu, L. Jia, J. Elambasseril, M. Qian, JOM, 69 (2017) 466-471.*

20. *A. Kreitcberg, V. Brailovski, S. Turenne, Mater. Sci. Eng. A, 689 (2017) 1–10.*

21. *T. Kimura, T. Nakamoto, J. Jpn. Soc. Powder Powder Metallurgy, 61 (2014) 531–537.*

22. *L. Thijs, K. Kempen, J.P. Kruth, J.V. Humbeeck, Acta Mater., 61 (2013) 1809–1819.*

23. *K.N. Amato, S.M. Gaytan, L.E.Murr, E. Martinez, P.W. Shindo, J. Hernandez, S. Collins, F. Medina, Acta Mater., 60 (2012) 2229–2239.*

24. *X.P. Li, X.J. Wang, M. Saunders, A. Suvorova, L.C. Zhang, Y.J. Liu, M.H. Fang, Z.H. Huang, T.B. Sercombe, Acta Mater., 95 (2015) 74-82.*

25. *P. Ma, K.G. Prashanth, S. Scudino, Y. Jia, H.Wang, C. Zou, Z. Wei, J. Eckert, Metals, 4 (2014) 28–36.*

26. *T. Enjo, K. Ikeuchi, K. Furukawa, J. Jpn. Inst. Light Metals, 35 (1985) 388-395.*

27. *M.W. Wu, J.K. Chen, B.H. Lin, P.H. Chiang, Mater. Design, 134 (2017) 163–170.*

IMPROVING MACHINABILITY RESPONSE OF PM COMPONENTS; ENSURING A REPEATABLE AND COST EFFECTIVE MACHINABILITY RESPONSE

Sunil Patel, Neal Kraus, Bruce Lindsley, Kylan McQuaig

Hoeganaes Corporation, Cinnaminson, NJ, USA

Abstract: Secondary processing of PM components is a necessity in the production of PM parts. Most produced parts across the industry require some level of secondary operations to produce an in-specification part. One of the major operations employed in this production is that of machining. While MnS is the most widely used machining additive in the industry, previous work has shown that processing conditions can greatly impact the response of this additive. Namely; it has been shown that MnS does not deliver a stable or consistent machining process when exposed to moisture in sintered PM parts. The response of both MnS and an alternatively designed stable additive (AncorCut) are explored.

Introduction

Powder metallurgy (PM) parts are widely used across a range of industries including automotive and lawn-and-garden. While the cornerstone of the PM industry is the ability to produce near net shape products at high throughput rates in comparison to other competing processes, a high percentage of parts require some level of secondary machining. This processing, which is often a secondary thought compared the primary production of the part, can still account for a sizable ~30% amount of the overall cost of part production as is the case for more complex assemblies such as carriers.

With this secondary processing, the material's response to cutting is a key driver to the overall cost of the process. A material – tool combination that allows for increased throughput and longer tool life spreads the cost of the disposable inserts across a greater number of parts and, in turn, reduces machining costs. However this reduced machining cost only works if the response is repeatable.

Machining response is a combination of many influences including part, machine, tool and process parameters shown simply in the fishbone diagram in Figure 1. To ensure a repeatable and,

therefore, cost effective and LEAN machining process, all these factors must be controlled. An area beyond part production which has been explored recently is that of production lifecycle [2]. Here, work has been conducted on the effectiveness of MnS when processed under several conditions. This information is of key importance as it shows that not only material selection and processing, but consistent lifecycle timing can have a profound impact on the industry's most widely used machining additive.
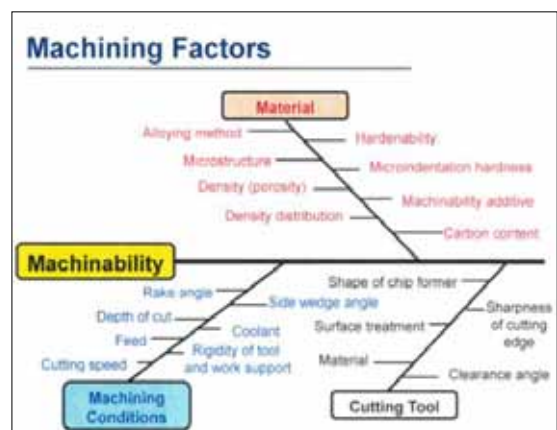

Figure 1: Fishbone diagram outlining factors which influence the machinability response of a PM part [1].

This area of work should be of key importance as there is often a pause in the production cycle of parts between sintering and machining when done at outside sources. This work focuses on the impact of lifecycle timing across different machinability additives and should act as a guide in the selection of machining additives based on process control capabilities.

Materials and Experimental Techniques

The machining response of the selected additives; MnS and AncorCut was evaluated in the industry's most common ferrous alloy system; namely, FC-0208 / F-08C2 (Fe-2Cu-0.8C). Machining was done in-house for turning and drilling utilizing a Haas ST-10 and VF-1, respectively. Parts were compacted to a density of 6.9 g/cm^3 and sintered at 1120°C in accordance with previous study parameters [2]. Measurements of both tool life and tool wear were used to assess the materials in question.

Results and discussion

In order to compare the stability and repeatability of the machining response of the selected additives, samples were compared in the As-Sintered and the Exposed-Sintered state as previously outlined by Kraus et al [2]. This work in combination with Borgonovo et al's [3] previous work shows that MnS, when exposed to humidity in the As-Sintered state, has a negative impact on the machining response of the parts; or more simply, that MnS is not stable in sintered PM parts (Figure 2).

In both cases a trend towards MnS having no beneficial effect on machining performance was observed with increasing moisture exposure levels. This observation of the impact of moisture exposure to machining performance indicates that the machining response of the material can be greatly impacted by changes in production timing. This varying response, or lack of product stability, then leads to lower efficiency as

machining cells will not get consistent tooling life, which increases time and, ultimately, cost.
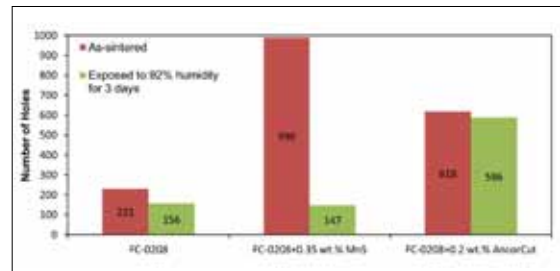
Figure 2: Effect of humidity exposure on drill bit life [3].

Further turning trials were subsequently completed on the FC-0208 material to complement the previous work. Figure 3 shows a change in wear response between samples machined in the As-Sintered and the Sinter-Exposed state. In this case, a greater slope of the line indicates a change in machining response (increased tool wear) after exposure of the sintered parts to moisture. This change in machining response thus indicates a lack of consistency in tool wear and an inherent lack of stability of the material. Since AncorCut and the no machining add state showed no change in machining response regardless of processing conditions, they are stable with respect to humidity exposure and their slope is low in Figure 3. Again, this information then corresponds with the previous data shown in Figure 2.
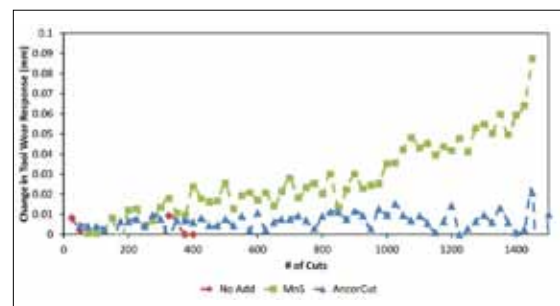
Figure 3: Change in machining response with sintered part exposure to moisture.

Similarly to the work shown in Borgonovo et al. and Kraus et al., the samples prepared with MnS showed a large increase in tool wear after exposure to moisture (green line). Thereby, the machinability with MnS-containing parts is less consistent over time and different atmospheric conditions. This inconsistency again is led by the fact that the MnS reacts with exposure to moisture and chemically and physically transforms (Figure 4).
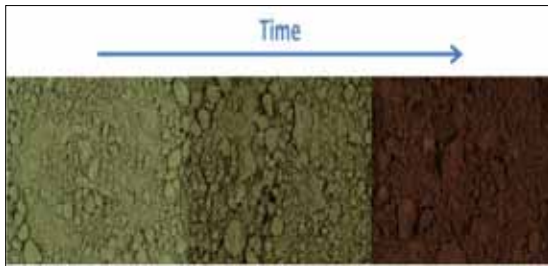
Figure 4: Effect of moisture exposure on MnS powder over time [2].

Alternatively, AncorCut was shown to be consistent regardless of the timing of moisture exposure, which leads to a more consistent machining response of the alloy. This is as expected, as AncorCut has been previously shown to be designed with stability in mind which not only helps consistency, but removes the propensity for part rusting that additions of MnS bring (Figure 5).
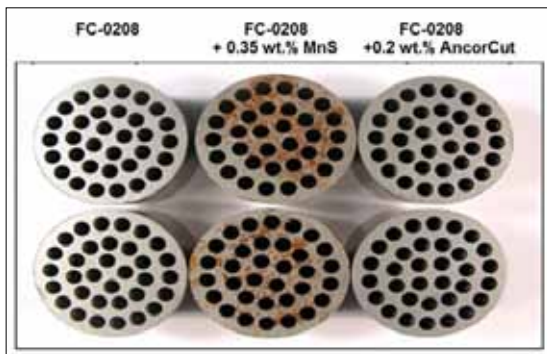
Figure 5: Rusting after 2 weeks of drilling with coolant [3].

Conclusions

• The machining response of MnS bearing products was found to be affected when sintered parts were exposed to moisture

• The machining response of AncorCut bearing products was found to be unaffected when sintered parts were exposed to moisture.

• AncorCut does not increase the propensity for part rusting as has been shown for MnS containing products.

References

1.   B. James, "Machinability of Ferrous PM Materials: Test Methods and Standards", Powder Metallurgy Machinability Seminar, April 4-5 2017

2.   N. Kraus, B. Lindsley and K. McQuaig, "Improving Machinability of PM Components; Examining the stability of additives and machinability best practices", September 2018, WorldPM2018 Proceedings, Beijing, China

3.   C. Borgonovo, B. Lindsley, "Improving Machinability of PM Components via a New Additive Compound", International Journal of Powder Metallurgy, 2016, Vol 52 (1), pp. 37-48

PROCESSING OF HIGH DENSITY W-Cu ALLOY BY NANOPOWDER PROCESS

Jai-Sung Lee

Department of Materials Science and Chemical Engineering,Hanyang University ERICA, Korea

Abstract: *High density tungsten (W) alloys with a density in the range of 15 to 19 g/cm³ are used for radiation absorption, gyroscope weights, kinetic energy penetrators, golf club weights, and aircraft wing weights. A wide variety of compositions exist for these applications, including W-Ni-Fe, W-Cu, W-Ni-Cu, W-Ni-Co and etc. Among them, lower copper (Cu) content of W-Cu alloy with less than 10 weight percentage of Cu is more advantageous than the heavy alloys such as W-Ni-Fe and W-Cu-Ni, in that the pure Cu matrix offers higher density as well as higher conductivity than the W soluble alloy matrix phases. However, due to insolubility between W and Cu, the lower Cu content W-Cu powder compact hardly attains full density by conventional sintering process.*

Introduction

Lee et al. [1] reported a possibility of full density processing of low Cu containing W-Cu alloy using nanopowder process. It was found that full density as well as homogeneous microstructure could be obtained only by conventional sintering of W-15wt.%Cu nanocomposite powders. Such an interesting finding was explained by the fact that the diffusion controlled Ostwald ripening process predominates full density process. Based on this result, the lower Cu content of W-Cu alloy below 10wt.%Cu can be fabricated by nanopowder process. The present study focused on optimal processing of high density W alloy using W-5wt.%Cu nanocomposite powder in terms of powder synthesis and consolidation by liquid phase sintering. Especially, microstructure evolution during liquid phase sintering of W-5wt.%Cu nanocomposite powders was discussed in association with material property and application.

Experimental Techniques

The W-5wt.%Cu nanocomposite powders were prepared by the mechano-chemical process using WO_3 (99.6%, 75□m) and CuO (99.9%, 1□m) [2]. Ball-milling of oxide powders was performed in an attritor at a speed of 300 r.p.m. for 1h in which the powder-to-ball mass ratio was 1:50

with a powder mass of 100 g, and methyl alcohol was used as a process control agent. After high energy ball milling, the powders were dried at 333K for 12h and sieved down to 150□m particle diameter. The W-Cu oxide powders were reduced during heating stage up to 1073K at 7K/min in hydrogen atmosphere (dew point 197K).

To optimize the condition of powder synthesis, the effect of Cu content on hydrogen reduction behavior of ball-milled WO_3 and CuO nanocomposite powders was investigated, in which hydrogen reduction kinetics were characterized by thermogravimerty and hygrometry measurements. For sintering experiments, the W-5wt.%Cu nanocomposite powders were compacted at 1250 MPa into disc (10 mm diameter, 1.5 mm height) to have relative green density of 48% theoretical density. Sintering was performed at 1623K for 2h in hydrogen atmosphere. Sintering properties of the W-Cu as densification process and mechanical property were investigated in terms of microstructure development using FE-SEM and Vickers hardness test, respectively.

Results and discussion

The result for the hydrogen reduction kinetics of W-Cu oxide nanocomposite powder revealed that the activation energy for reduction of

nanoscale WO_3 exists in the range of 129 to 139 kJ/ mol, which is in accordance with the activation energy for reduction of conventional WO_3 powders. However, the presence of Cu phase was found to inhibit the reduction process of W oxide by reducing diffusion paths. Fig. 1 shows the microstructures of (a, b) surface- and (c, d) center zone of the W-Cu specimen after sintering in which the microstructure of the center zone inside the specimen was observed on the fracture surface. It is clearly observed in Fig. 1(a, c) that the low Cu content of W-Cu nanocomposite powders during sintering at 1623K reached full density with homogeneous microstructure. More striking microstructures can be seen at higher magnification in Fig. 1(b, d). The surface zone of the specimen shows a very interesting soap-bubble like structure which consists of well grown W grains and film like interface structure. Such homogeneous microstructure is a good evidence for W grain growth in the process of full densification process during sintering of W-5wt.%Cu nanocomposite powders. This microstructure gives an implication on the shape and distribution of the constituent phases of W and Cu. The microstructure of the fracture surface in Fig. 1(d) enables us to understand about such microstructural evolution.
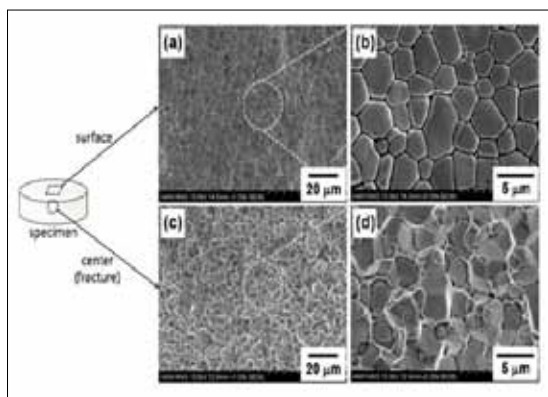

Fig.1. (a, b) Surface and (c, d) fracture morphologies of the W-5wt.%Cu specimen sintered at 1623K for 2h in hydrogen atmosphere

The most important factor initiating microstructure evolution is undoubtedly particle coarsening. As mentioned[1], the diffusion-controlled Ostwald ripening (DOR) of W grains is basically responsible for particle coarsening during sintering of W-Cu nanocomposite powders. Since commercial-grade of W-Cu powders contain a certain amount of impurities as it does in this study (total impurity level ~0.5wt.%), it is easily expected that the DOR growth of W grains is responsible for the microstructure evolution occurred in this W-Cu alloy. Moreover, capillary effect (Gibbs-Thompson effect) might promote the kinetics of local dissolution of nano-sized W powders in liquid Cu phase. Based upon the microstructure, it is expected that the W-5wt.%Cu provides high strength and physical conductivity by high contiguity structures of W-W grains and Cu phase, respectively.

To check mechanical property simply among these properties, hardness was measured to compare with the conventional W heavy alloys. It was found that the Vickers hardness of the W-5wt.%Cu alloy was 427±22 Hv, which is much higher than that (276±19Hv) of the conventional heavy alloy (94.9W-3.4Ni-1.7Cu). This result is thought to result from a higher contiguity structure of W grains compared to the conventional W heavy alloy due to a larger dihedral angle ($\square$=152º at 1623K) of W-Cu than W-Ni-Fe system. It is also expected that this high density W-Cu alloy has a higher conductivity owing to interconnected copper phase.

Acknowledgement

References

1. *J. S. Lee and J. H. Yu, Z. Metallkd. 92 (2001) 7.*
2. *J. S. Lee and T. H. Kim, Nanostr. Mat. 6 (1995) 691.*

CURRENT TRENDS & ADVANCES IN THE FABRICATION & APPLICATION OF DIAMOND TOOLS

Janusz S. KONSTANTY

AGH - University of Science & Technology, Krakow, Poland

Abstract: Historically, the methods of making diamond tools have undergone a remarkable development since the invention of synthetic diamond in the mid-1950s. Until the early 1990s the diamond tool industry had been mainly threatened by the very high cost of diamond, whereas the price of other raw materials, e.g. cobalt-based matrix powders, used in most professional and non-professional applications, had remained at an acceptable level. The sharp rise in the price of cobalt initiated an intensive search for cheaper matrix materials. Concurrently, rapid improvements in the cubic type multi-anvil high pressure equipment and its large-scale implementation for diamond synthesis, resulted in tremendous price cuts on the diamond supply side. As most of the diamond grits have always been used for sawing natural stone and concrete, new production techniques that emerged in the stone and construction industries in the 1990s brought pressure on toolmakers to develop new manufacturing routes and refine the existing tool designs in order to do the job faster, more accurately and at less cost. To meet all these objectives, the main efforts were directed toward substituting fine cobalt powders with iron-base and copper-base alloys, overcoming unsatisfactory diamond grit retention and achieving its better distribution in the sintered matrix, and developing methods and tools for hard-rock slabbing to render the slab production faster and cheaper with the minimum waste of rare and precious stones.

In sintered diamond tools substitution for cobalt often results in a loss in product performance. However, the steeply rising contribution of cobalt to the overall tool fabrication costs triggered an intensive search for cheaper matrix powders. This resulted in development of finely dispersed, pre-alloyed copper-base and iron-base powders. Since 1997, when the first powders were launched commercially under brand names Cobalite and Next, the number of specific grades has almost quadrupled to cater for the wide diversity of tool manufacturing techniques and application conditions. The inherently high manufacturing costs of chemically pre-alloyed powders affect their final price, which remains a major concern for their use. This attracts attention to markedly cheaper pre-mixed powders which, as their pre-alloyed counterparts, are steadily formulated and refined to couple the excellent consolidation behaviour with field performance similar to cobalt.

For a tool that is wearing ideally, the fraction of lost diamond grits should not be too large. The anchoring of grits by mechanical means often proves insufficient to retain high-grade blocky crystals used to cut granite and tough ceramics. To date two methods have been used to solve this problem. The most common practice involves coating the crystals with a thin film of a strong carbide former, such as titanium, chromium or silicon, which increases metallurgical bonding and diamond protection from surface graphitisation and prevents attack by aggressive matrix components. The coatings differ in thickness, method of deposition and are being applied to grits throughout the expanding range of qualities to suit a wide spectrum of applications and tool fabrication conditions. Parallel developments are being seen in thermal treatment of the crystals during consolidation of the diamond impregnated component. By roughening their surface it is possible to improve the hold on diamond grits by increasing friction at the diamond-matrix interface. Until quite recently this method was rarely practiced due to a high risk of harming the crystal integrity and strength. However, the latest application of this technique to the fabrication of wire saw beads has proved effective.

Other benefits can accrue to tool performance from uniform distribution of diamond crystals in the metallic matrix. This can be achieved by using either grits encapsulated in the matrix powder or diamond placing technology. The encapsulation route eliminates diamond clustering and their premature loss, and offers the freedom to vary the composition of discrete layers within the encapsulated pellet in order to improve grit retention and protrusion.

CURRENT TRENDS & ADVANCES IN THE FABRICATION & APPLICATION OF DIAMOND TOOLS

A technological breakthrough in manufacturing saw blade segments, wherein diamonds are equally-spaced and arrayed in a regular pattern, was made and implemented in 2004. At that time the elimination of random grit distribution alone resulted in marginal improvement in tool performance and did not justify increased production costs. Later enhancements in both cutting rate and tool life became possible due to optimising the number of diamond impregnated layers and arrangement of crystals within these layers. Nowadays specially designed segments are making significant inroads into the problem of slabbing granite with diamond frame saws. The new diamond blades cut faster than the traditional steel shot frame saws with lower kerf loss.

Since the 1980s diamond wire sawing technology has been gaining ground in the stone industry, primarily for quarrying of stone blocks and their further division, as well as in various construction applications. Further machine and wire developments were needed for hard-rock sawing. Stationary mono-wire machines were first developed and used for block squaring and profiling. Multi-diamond-wire (MDW) machines are the newest type of equipment used for granite-

block slabbing, where they mainly compete with traditional steel shot frame saws. In recent years considerable effort has been made to reduce the wire thickness. Through improvements in the construction of MDW machines, bead formulation and design, rope splicing and plasticisation, it is now possible to produce wires thinner than 4.5 mm.

Today, approaching the end of the second decade of the 21st century, we see that engineers are continually developing raw materials, tools and their production routes in order to improve their working characteristics and introduce them into new application areas. Examples include iron-rich powders free-sintered to near-full density below 950ºC, self-brazing powders dedicated to free-sintering of diamond beads, new small-diameter bead designs, as well as saw blade segments and core drill segments fabricated by high-pressure high-temperature sintering technology.

Introduction

The current review summarises key historical, recent and ongoing trends and developments in sintered diamond tools. The report concentrates on tools used within the stone and construction industries which, being the main consumers of metal-bonded diamond tools fabricated by powder metallurgy (P/M) technology, have always fuelled advances in tool design and production technologies.

Historical Background

The successful application of ultrahigh pressure to synthesise diamond grits and their commercialisation in 1957 [1] was a real milestone in fabrication and application of sintered diamond tools. Since that time, metal-bonded diamond-impregnated composites manufactured by various P/M routes have been increasingly used in machining natural stone

and ceramics, for cutting concrete, road repair and petroleum exploration. In 1990 the overall consumption of industrial diamond reached the volume of approximately 380 million carats, but still remained limited by the high price of the synthetic material utilised for more than 90% of industrial applications [2].

The situation changed during the 1990s, when consumption of synthetic crystals almost tripled, reaching 1 billion carats in 2000 [2]. A large share of the market was taken by a rapidly growing Chinese production. In the early 1990s tool fabrication costs were mostly affected by the very high prices of diamond grits and, to a lesser extent, hot pressing consumables, whereas the contribution of cobalt or cobalt-base matrix powders, ideally suited for the vast majority of applications, remained at an acceptable level. The then forthcoming drop in the price of synthetic grits and a sharp decrease in consumption of

graphite moulds and electrodes, due to the application of vacuum/nitrogen gas chambers in the hot pressing equipment, focused more attention on the steeply rising contribution of cobalt to the tool fabrication costs. The instability of the cobalt market initiated an eager search for cheaper options. Consequently four iron-base and copper-base cobalt substitutes were developed and marketed under the brand names Next (Eurotungstene 1997 [3]) and Cobalite (Umicore 1998 [4]). Concurrently, significant improvements in grit quality and its retention in the metallic matrix were achieved through the evolving sophistication of diamond synthesis and crystal coating technology.

In the new millennium the market for diamond tools has grown even faster. Although the data released for the years 2004–07 is inconsistent [5-7] there is no doubt that in the late 2000s production of industrial diamond reached the impressive volume of nearly 10 billion carats, with China emerging as the world's leading producer, with the annual production approaching 9 billion carats [7]. This became possible due to the massive use of large-volume, cubic-anvil high-pressure apparatus [8] in which a system of previously used external frames of tie bars was replaced by Chinese engineers with large castings connected by cylindrical pins. These castings were mass produced without extensive machining needed for the original tie bar/base design, giving cost advantages directly benefiting high volumes of production [9]. As a natural consequence of availability of synthetic grits in very large volumes and varieties, prices dropped by a factor of 5 [10], which transformed diamond into a commoditised product. It is noteworthy that the tremendous drop in the price of synthetic grits manufactured in China, to around 5 US¢ per carat in 2010, was accompanied by significant improvements in quality, catching up with the products offered by the world's leading producers [8].

Premature tool wear due to a non-uniform distribution of diamond crystals in the metallic matrix has always been a major concern. Early attempts to solve this problem by using metal powder-coated diamonds were made in the 1980s and 1990s [11-13]. This work was continued in the 2000s. The emphasis was placed on fabrication of dual-layered pellets containing a thin, tungsten carbide rich region localised around the diamond crystal. The usage of a wear resistant inner layer resulted in increased tool life, due to improved grit retention and protrusion [14].

A more ambitious approach to controlling grit distribution in the metallic matrix was proposed by two Korean toolmakers, i.e. EHWA Diamond Industrial Co. Ltd. (ZENESIS Project) and Shinhan

Diamond (ARIX Project). New ideas of placing diamond grits in three dimensional patterns were developed in the late 1990s and patented in the early 2000s [15-17]. Over the next few years proprietary technologies were mastered to position the grits within the segment in an optimal manner. Significant improvements in both cutting rate and tool life were achieved after proper sequencing of diamond-containing and diamond-free layers and finding the optimum angle at which the rows of diamonds were inclined with respect to the tool working face. The first ZENESIS and ARIX circular blades were launched commercially in 2004 and 2005, respectively. Soon after the ZENESIS technology was extended to other types of tools, including frame saw segments for sawing granite [18]. Over the next few years diamond setting technology was gaining ground due to the commercial availability of fully automated systems [19]. The universally accepted diamond placing method employs a volumetric cold press which fills a steel die with a thin layer of matrix powder, sets diamond crystals onto this layer in a predetermined pattern by a perforated suction

feeder, levels the powder at a low pressure, puts another layer of powder on top of the previous layer, and so forth. The sequence continues until the preset number of layers is achieved. Then full compaction pressure is applied, followed by ejection.

In addition to the significant technological progress in diamond synthesis, tool design and its fabrication techniques, the first decade of the new millennium witnessed a major breakthrough in the recognition of the diamond wire saw as a powerful tool in sawing granite and other difficult-to-cut-stones. At the turn of the 1970s and 1980s, when diamond wire was successfully used for quarrying and squaring of marble blocks in Carrara [20], there was a common opinion that igneous rocks would never be cut economically with diamond wire, due to the high cutting forces. At that time, granite blocks were cut into slightly oversize slabs with traditional steel shot frame saws, while diamond-segmented frame saws were used exclusively on softer stones, such as marble, dolomite or sandstone. The then forthcoming machine and wire developments enabled widespread commercialisation of mobile single-wire machines for granite extraction in the quarry and stationary mono-wire machines used for block squaring and/or profiling [21]. A prototype multi-diamond-wire (MDW) machine, equipped with 10 wires, 10 mm in diameter, was tested in 1994, but extensive use of MDW machines in slabbing of granite blocks as a replacement for steel shot frame saws came in the 2000s [22]. As the technology evolved, MWD machines taking 58 wires 6.7 mm in diameter were soon marketed by Bideseimpianti S.r.l. in Italy [20], which was a significant breakthrough in machine design.

**Current trends and market perspectives for sintered diamond tools**

In 2009, the slowdown in global economies affected mainly the European stone and construction industries. Until 2013, the EU (28 countries) suffered a 16% drop in the production of natural stone and around 9% in the construction industry [23]. China, on the other hand, took over the leading position in the international natural stone industry from Italy, increasing its world market share to 42.4% in 2015 [23]. However, after a period of unrestrained growth, stone production in China began to show a reverse trend [24]. The overall demand for diamond tools in China also declined, following the downturn in stone and construction industries. The output of Chinese synthetic diamond fell from 16.8 billion karats in 2014 to 15.1 and 13.9 billion karats in 2015 and 2016, respectively. The annual production of synthetic diamond grits is projected to grow at a moderate rate to reach 16.5 billion karats by 2020 [25].

With further improvements in the Chinese synthesis technology, toolmakers should rather expect better value for money than significant price cuts on the diamond supply side. In spite of this, the contribution of diamond grits to the overall tool costs will remain low. Therefore diamond tool industry's sole concern is to reduce the price of matrix powders and to use more cost-effective tool fabrication processes.

Historically, cobalt has been the most valued matrix metal, but recent figures reveal for the Italian market a decreasing use of cobalt, which accounts for 25% of 350 tons of powders consumed annually by the diamond tool industry [24]. Pre-alloyed powders constitute the largest share of 40% [24], but, despite obvious advantages over pre-mixed powders (35% share), they are expensive to manufacture. Therefore intensive research is currently in progress to substitute for the commercially practiced hydrometallurgical methods, which generate large quantities of environmentally harmful wastes (salts). Emphasis is also placed on lower content, or complete elimination, of expensive alloying elements such as cobalt or nickel.

CURRENT TRENDS & ADVANCES IN THE FABRICATION & APPLICATION OF DIAMOND TOOLS

The method developed at AGH [26] eliminates the expensive hydrometallurgical stage at which homogeneous mixtures of hydroxides, or oxalates, are formed. It has been replaced by an inexpensive mechanochemical synthesis of hydrogen reducible oxides, which provides more freedom in the selection of powder chemical composition. The process relies on ball milling of substrates prior to annealing in a reducing gas. Examples of fully pre-alloyed powders developed and manufactured [27] by means of this method are illustrated in Fig. 1.
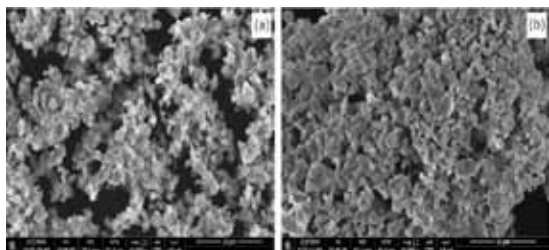
Fig. 1. Fe-Cu-P powder containing 95.5% iron (a) and "self-brazing" Fe-Cu-Sn-P powder containing 90% iron (b)

The powders can be pressureless sintered to a closed-pore state at 900°C and yield materials which meet acceptance criteria for the fabrication of high quality tool components, e.g. diamond saw beads. After cold compaction at 200MPa and pressureless sintering at 900°C in hydrogen, the Fe-Cu-P powder reaches a density of 7.74 g/cm^3 and a hardness of 212 HV. Interestingly, on quenching from the sintering temperature, the alloy can be age hardened to 312 HV. The tin-modified Fe-Cu-Sn-P version has been developed for efficient and economical fabrication of diamond saw beads. A green diamond-impregnated tube made from the self-brazing powder can be firmly joined to a plain carbon steel sleeve during sintering, thereby eliminating the need for a subsequent brazing operation. In the as-sintered condition the self-brazing alloy reaches a density of 7.94 g/cm^3 and a hardness of 230 HV.

Ball milling can also be used in the manufacture of inexpensive matrix powders for fabrication of diamond segments by the hot press route. It has been shown that ball-milled iron-base Fe-Ni-Cu-Sn-C and Fe-Mn-Cu-Sn-C powders can be hot pressed to near-full density at 900°C, to yield materials characterised by high resistance to abrasion [28]. Until recently it has been common practice to use fine Co-WC powders, typically containing 20-40% WC, for the fabrication of diamond segments for cutting/drilling abrasive materials such as sandstone, fresh concrete, asphalt, porous ceramics, etc. The combination of a very low price, ease of densification and high abrasion resistance makes the ball-milled iron-base powders ideal candidates to replace expensive Co-WC mixtures for the fabrication of tools for processing abrasive materials.

The consolidated pre-alloyed powder matrices have finer microstructures and higher mechanical strengths compared to those made from pre-mixed powders. The latter option has usually the merit of being cheaper. Moreover, pre-mixed powders show flexibility in alloy composition, enabling creation of unique microstructures and properties, have better pressing characteristics, and can readily be customised to fit specific wear conditions, etc. Therefore there is enough incentive for toolmakers to continue developing proprietary powder compositions. Combinations of the base carbonyl iron powder with pre-alloyed bronzes, elemental copper, tin, nickel and WC are most often used for a wide variety of applications.

There has been a lot of machinery designed for working stone, ceramics and construction materials over the past decade. The industry sees novel CNC workcentres, bridge saws, wire saws, etc. The machines themselves can be remotely diagnosed by the manufacturers via the internet or monitored to provide information about

working conditions and service demands. The new processing techniques dictate novel tool designs which have to meet unique application requirements.

Unlike any other types of tools, a wire saw for hard-rock sawing has undergone many modifications in recent years to improve its performance. Today wire sawing technology is undergoing widespread commercialization and is used, not only for granite block extraction at the quarry face, block squaring and profiling on mono-wire machines, but also increasingly for finish slabbing of blocks on MDW machines. Unlike single diamond wires, which have reached maturity, replacing large circular diamond blades, the MDW technology is still being developed and has yet to reach its full potential. As there is still a considerable number of steel shot frame saws in operation, diamond multi-wires must also compete with the patterned diamond frame saws, which can be used on the traditional pendulum motion frames after their modification [29].

In frame sawing the reciprocating movement of the blade facilitates diamond pullout since there is no build-up of matrix tail, and forces act on diamond grits in alternate directions. The

patterned diamond segments, so-called ZGS (Zenesis Gang Saw) segments, contain diamonds arranged in groups of at least two crystals. Short distance between the working grits, of 2-3 times the grit size, changes their loading conditions and enables formation of a supporting matrix tail, similar to that on circular saw blades. The effect of cutting conditions on diamond loading is explained schematically in Fig. 2.

The ZGS system has advantages over traditional steel shot frame sawing in that the yield of usable stone is bigger by 15%, the cutting rate is 3-5 times higher, and there is far less variation in slab thickness and a better surface finish. As

demonstrated in Table 1, until recently the ZGS system also outperformed MDW sawing in terms of yield obtained from the stone.
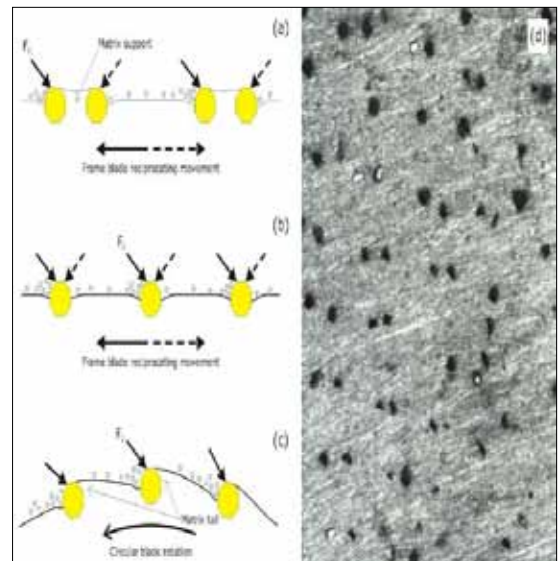
Fig. 2. Diamond loading force (Fc) in frame sawing (a), (b) and in circular sawing (c).
(a) ZGS segments: build-up of matrix supports between paired diamonds; trailing grits are not loaded (b) Conventional segments: undercuts on either side of grits due to alternating loading (c) Circular blade segments: build-up of matrix tails due to blade rotation in a constant direction (d) Side view of a ZGS segment

Table 1. Yields of slabs and down-feed rates typical for various granite slabbing methods

Sawing technique	Number of slabs per 2 m block width		Down-feed rate, cm per hour
	Slab thickness: 21 mm	Slab thickness: 31 mm	
Zenesis Gang Saw	76	56	10 - 15
Steel shot frame saw	66	50	2 - 5
Multi-wire ø7.3 mm	68	51	20 - 50
Multi-wire ø6.3 mm	72	53	20 - 50
Multi-wire ø5.3 mm	74	55	20 - 50
Multi-wire ø4.3 mm	80	57	20 - 50

In 2017, however, a significant breakthrough in MDW sawing took place with the advent of ø4.3 mm diamond wires installed on a dedicated MDW machine designed and constructed in Poland by Q-TEQ Ltd. (Fig. 3).
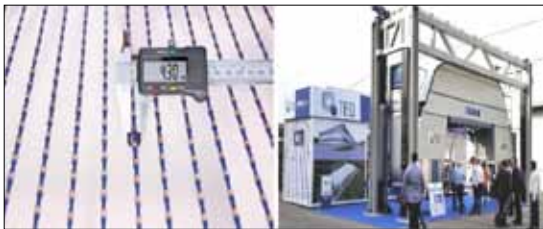

Fig. 3. The thinnest commercial diamond wire and presentation of Premia MDW machine at Marmomac 2017 held in Verona, Italy (Courtesy of Q-TEQ Ltd.)

In addition to faster cutting, another advantage of MDW systems over frame sawing is quick positioning of wires on the machine, which allows simultaneous production of slabs of different thickness (2-3-4-5 cm and multiples). The benefits of MDW sawing have recently been recognised by manufacturers of stone tiles used for flooring and wall cladding. Although multi-bladed tile sawing machines are still in common use, an unique Polyone multi-wire winding system has been designed to perform two simultaneous cuts, in opposite directions, for each wire, in order to produce slightly oversize slabs for further calibration and polishing to a finished tile thickness of 1 cm [30].

Seemingly, diamond multi-wire sawing is now the fastest growing application area for sintered diamond tools [31]. Producers of MDW machines increasingly demand smaller diameter diamond wires to minimise kerf width and maximise the number of slabs that can be sawn from a single block. Apart from this increase in yield, there are also significant economic and environmental benefits to accrue from increased cutting rates and smaller amounts of waste generated.

An undesirable consequence of decreasing the wire thickness is a disproportional reduction in the steel rope diameter. For fixed block sawing, the downward pressure of the wire on the block is kept constant. Therefore, assuming the same bead length, spacing and specification, the wire tension force has to be set proportional to its diameter. It means that for the dimensions provided in Fig. 4, the ø2 mm steel rope used in ø4.3 mm diamond wires has to withstand tensile/fatigue loads at least 75% higher compared to those used in ø6.3 mm and ø7.3 mm wires. This gives rise to the urgent need for stronger steel ropes and high-grade diamond beads. The latter include improved bead sintering parameters and optimum selection of matrix powders and diamond grits, with an emphasis on free-cutting characteristics of the tool.
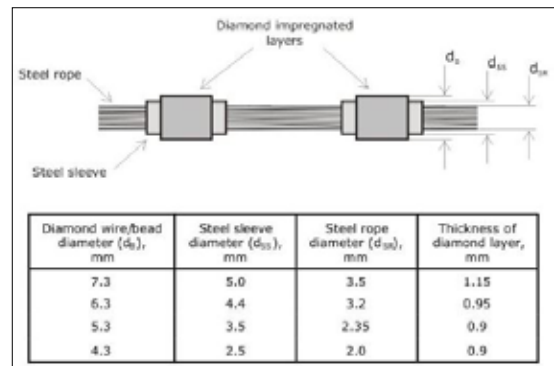

Diamond wire/bead diameter (d_b), mm	Steel sleeve diameter (d_{ss}), mm	Steel rope diameter (d_{sr}), mm	Thickness of diamond layer, mm
7.3	5.0	3.5	1.15
6.3	4.4	3.2	0.95
5.3	3.5	2.35	0.9
4.3	2.5	2.0	0.9

Fig. 4. Typical diamond bead and steel rope dimensions

The commonly used ø7.3 and ø6.3 mm wires are likely to be superseded by thinner, with ø5.3 and ø4.3 mm, very soon. Therefore major improvements in construction of MDW machines, bead formulation, design and spacing, steel rope strength, rope splicing and wire plasticisation are needed to satisfy the demanding application conditions and increasing customer expectations. Finding solutions to all these problems is a great challenge for the toolmakers today.

Looking forward

The advancements seen over the last decades in diamond synthesis technology have brought down diamond price by two orders of magnitude and led to its large-scale industrial use. As a natural consequence, the matrix powders and tool fabrication technologies have been receiving increasing toolmakers' attention. Therefore, there is considerable interest and activity in development of new and improvement of existing metallic powders and tool fabrication routes today. The matrix powders should combine low price with desired sintering characteristics and excellent application performance, whereas manufacturing technologies are expected to be more cost-effective. On a laboratory basis, diamond-impregnated segments for sawing and drilling have already been manufactured by high-pressure high-temperature sintering technology in China [32,33]. Significant progress recently achieved by Chinese design engineers in the development of the cubic high-pressure apparatus and its adaption to high-pressure sintering is a good prognostic for future commercialisation of this technology.

Despite the signs of stagnation in stone and construction industries, they will most probably continue to consume the majority of sintered tools with a growing demand for diamond wires. Until very recently fabrication of ø6.2 mm beads presented a formidable technological challenge [34]. Due to unique approaches for onward development, however, sintered diamond beads thinner than 4 mm in diameter may soon be targeted.

References

1. J.C. Sung et al., *The revolution of diamond synthesis technology. Materials Science Forum 2007, 534-536, 1141-1144*

2. C. Owers, *Industrial diamond: applications, economics and a view to the future. Industrial Diamond Review 2000, 60(3), 176-181*

3. Anon., *A new generation of powders for the diamond tool industry. Marmomacchine Int. 1997, 18, 156-157*

4. I.E. Clark, B.J. Kamphuis, *Cobalite HDR - a new prealloyed matrix powder for diamond construction tools. Industrial Diamond Review 2002, 62, 177-182*

5. D.W. Olson, *Diamond, Industrial. U.S. Geological Survey Minerals Yearbook - 2007, p. 21.10*

6. D.W. Olson, *Diamond, Industrial. 2008 Minerals Yearbook, p. 21.11*

7. B. Williams, *Powder Metallurgy: A Global Market Review. International Powder Metallurgy Directory, 15th Edition 2012-2013, Innovar Communications Ltd., Shrewsbury, U.K., 2012, 5-25*

8. Z.H. Li et al., *China's diamond in the world market. Key Engineering Materials 2011, 487, 526-532*

9. J.D. Belnap, *Sintering of ultrahard materials. Sintering of advanced materials. Ed. Z.Z. Fang. Woodhead Publishing Ltd., Cambridge, 2010, 389-414*

10. *Diamond Industry Report 2011, Bain & Company, Inc., p. 61*

11. K. Kimura, *Method for forming metal-coated abrasive grain granules. US Patent 4,770,907 (September 13, 1988)*

12. R.R. Matarrese, *Dual-coated diamond pellets and saw blade segments made therewith. US Patent 5,143,523 (September 1, 1992)*

13. O. Cai, *Encapsulated diamond: remarks and technical notes. Diamante Applicazioni & Tecnologia 1996, 2(8), 62-72*

14. D. Egan et al., *A study of the use of encapsulated diamond in saw-blades for the cutting of stone. Proc. PM2010 World Congress, Vol. 3, 10-14 October 2010, Florence, Italy*

15. C.M. Sung, *Metal bond diamond tools that contain uniform or patterned distribution of diamond grits and method of manufacture thereof. U.S. Patent 6,286,498 B1, Sep. 11, 2001*

16. S.K. Kim et al., *Diamond tool. U.S. Patent 6,626,167 B2, Sep. 30, 2003*

17. H. Park, *ARIX - a major advance in diamond segment design. Industrial Diamond Review 2005, 65(2), 40-42*

18. S.K. Kim et al., *Cutting tip of frame saw and frame saw with the cutting tip. U.S. Patent 8,656,901 B2, Feb. 25, 2014*

19. G. Weber, *DiaSet - now fully automatic setting of diamond arrays. Diamond Tooling Journal 2010, 2 (1), 38–40*

20. P. Daniel, *Multi-wire saws gains ground. Stone Business, December 2006*

21. M. Jennings, *Diamond tooling in the new stone age. Stone Business, August 2004*

22. P. Daniel, *The multiwire story. Diamante Applicazioni & Tecnologia, 2015, 21(82), 29-36*

23. M. Gussoni, *Stone sector 2016. Annual Report and Prospects for the International Stone Trade. Internazionale Marmi e Macchine Carrara S.p.A., 2016*

24. E. Dossena, F. Tagliabue, *The diamond tools community in Italy. Diamante Applicazioni & Tecnologia 2017, 23(91), 17-27*

25. *Global and China Synthetic Diamond Industry Report 2017 with Focus on the Chinese Market 2016-2020, Research and Markets, Dublin, March 09, 2017*

26. J. Konstanty et al., *Prealloyed iron-based powder, a method for the manufacturing and use thereof and a sintered component. European Patent Application EP 3 124 634 A1, 1.02.2017*

27. J. Konstanty, *New highly sinterable iron-base powders for diamond wire beads. Diamante Applicazioni & Tecnologia, 2015, 21(82), 18-19*

28. J. Konstanty et al., *Ferrous ball-milled powders for fabrication of sintered diamond tools. Advanced Materials Research, 2014, 1052, 514-519*

29. *www.zenesissolutions.com*

30. *www.pellegrini.net*

31. U. Wilkinson, *Modern Multi-wire production. Proc. 6th Zhengzhou International Superhard Material & Related Products Conference, 14-17 November 2013 , Zhengzhou, China, 139-142*

32. F. Deng et al., *Comparative test of diamond-thin-walled drilling rig in China. 18th session of Chinese Superhard Materials Technology Development Forum. Taiyuan, Shanxi, China, 2014, p. 113*

33. Y. Zhao, *Study on the new sintering technology and sawing performance of large diamond circular saw blade. MSc thesis, China University of Mining & Technology, Beijing, 2016, 55-74*

34. J. Konstanty, *Sintered diamond tools: trends, challenges and prospects. Powder Metallurgy, 2013, 56(3), 184-188*

DEVELOPMENT OF TITANIUM BASED IN-SITU COMPOSITES PREPARED BY CONVENTIONAL POWDER METALLURGY ROUTE AND ITS FUTURE ASPECTS

Harshpreet Singh, Muhammad Hayat and Peng Cao

Department of Chemical and Materials Engineering, Auckland, New Zealand

Abstract: *Metal matrix composites (MMCs) are widely used in engineering applications. MMCs reinforced with ceramic particles provide high strength while maintaining reasonably good ductility and hence have been used in practical applications for decades[1, 2]. Titanium and its alloys are known to possess a good set of mechanical properties. High specific properties (e.g., strength/density, stiffness /density, modulus/density), and good creep and corrosion resistance of titanium make it an attractive candidate for many applications[3]. By reinforcing high-temperature, lightweight materials such as titanium with ceramic particulates of high strength and high stiffness, a class of composite materials have been produced and commonly referred to as titanium-based metal matrix composites (Ti-MMCs).*

In this work, the effect of different reinforcements (borides, nitrides and carbides) have been studied in the development of Ti-MMCs by powder metallurgy route. Here we used TiB2, Si3N4 and MWCNTs as our major reinforcements for the fabrication of titanium based MMCs. The effect of reinforcements on the microstructure evolution, interfacial bonding between reinforcement and matrix and mechanical properties have been studied in detail. A systematic study of the various physical and mechanical properties of the composites was also studied.

Experimental Methodology and Results

Ti-in-situ TiB Composites

Ti- in-situ TiB composites were developed by powder metallurgy route. The effect of concentration of TiB_2 particles was studied by reinforcing titanium diboride (TiB_2) powder in different weight fractions (2, 5, 10 and 20 wt.%) into pure Ti powder during the fabrication process. The present study investigates the phase identification and microstructural evolution of these in-situ TiB composites. The influence of the concentration of the reinforcement system was understood by analysing the interfacial bonding between the Ti matrix and TiB reinforcements. The dynamic mechanical properties, such as flexural strength and impact energy evaluations, were performed to understand the behaviour of the composite system subjected to transient (dynamic) load cases. A tribology study is also carried out to determine the wear characteristics of this composite system for relevant industrial applications. Fig.1 shows X-ray diffraction graph which confirms the successful development of

these in-situ composites. No peaks of TiB_2 were observed, indicating that the chemical reaction between TiB_2 and Ti was completed successfully during sintering at 1300°C. Fig.2 shows the bright field TEM image for these composites. The needle type morphology of TiB whiskers can be clearly seen from TEM image.
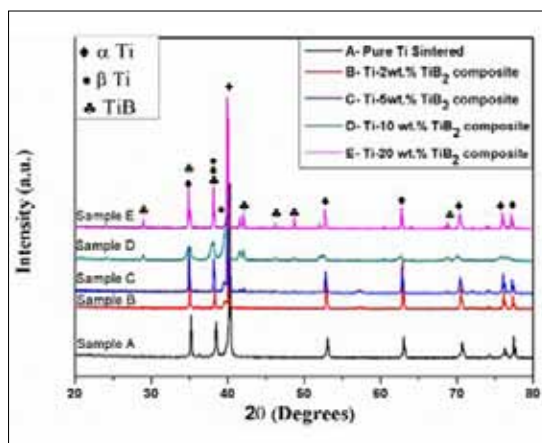

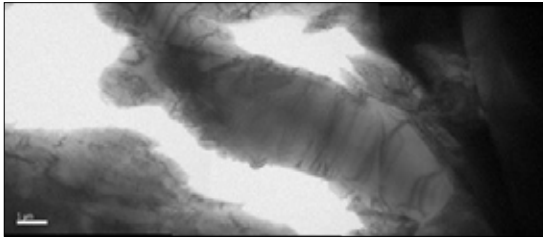*Fig. 1 X-ray diffraction for Ti-in-situ TiB composites*

Fig. 2 Bright field TEM image of Ti-in-situ TiB composites

It is worth noting that all the developed composites were of high density, > 90%. The hardness value increases with increasing the TiB_2 fraction in the matrix. The highest hardness value is ~ 580 HV1 achieved in sample E, which had the highest TiB_2 fraction. The recorded flexural strength for Pure Ti is ~ 1420 MPa which is increased to ~ 1554 and 1541 MPa for samples Ti- 2 wt. % TiB2 composites and Ti -5 wt. % TiB2composites, respectively. This corresponds to an increase of 9.4% and 8.5% respectively, for samples Ti- 2 wt. % TiB_2 and Ti -5 wt. % TiB_2 composites as compared to pure Ti without losing much ductility.

Ti-Si_3N_4 Composites

Ti-based composites with Si_3N_4 particle reinforcements were fabricated by a conventional press and sinter route. The effects of sintering temperature and the fraction of Si_3N_4 in Ti matrix were investigated ,regarding phase constituents, microstructure and tribology properties. The weight fraction of Si_3N_4 particles added in the raw mixtures varies from 1 wt. % to 5 wt. %. A systematic study of in-situ phase formation and tribology properties were studied for prospective wear resistant material in industrial applications. The X-ray diffraction study (Fig.3) reveals the formation of a new in-situ Ti_5Si_3 phase at Ti-5 wt. % Si_3N_4 composite sample. The formation of Ti_5Si_3 is due to the in-situ reaction ($5Ti + 3Si \rightleftharpoons Ti_5Si_3$) between Ti and Si at higher temperature [4-6].
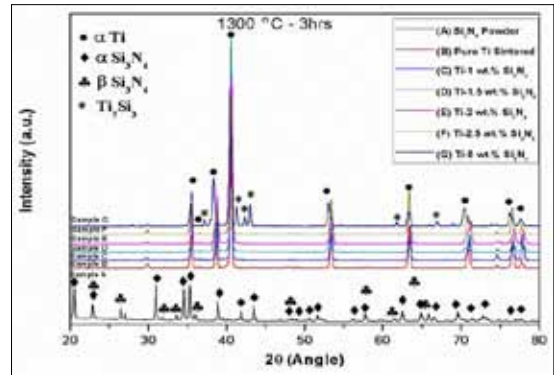

Fig. 3 XRD pattern for composite samples

It was found that Si_3N_4 completely decomposes during sintering resulting in the formation of different in-situ phases depending on the weight percent of Si_3N_4. At low concentrations of Si_3N_4 (≤1 wt. %), only silicon and nitrogen solid solution strengthening was observed. As the concentration of Si_3N_4 increased in titanium matrix, an additional effect of precipitation hardening was observed with the formation of new in-situ phases. However, the mechanism for the in-situ reaction needs further investigation by high energy in-situ X-ray or neutron diffraction technique.

Ti-TiB_2- MWCNTs hybrid composites

Ti-0.2wt% MWCNTs composite (sample A) and a Ti-0.2 wt. % MWCNTs -1.8 wt. %TiB_2 composite (sample B) was prepared by conventional powder metallurgy route. Microstructural characterization of these composites was studied in detail to observe the formation of new in-situ phases during sintering at a higher temperature. Microhardness and wear properties were also analysed for these composites system.The X-ray diffraction graph in Fig. 4 shows the peaks of α-Ti and TiC for sample A and α-Ti, TiC peaks and TiB peaks respectively which confirms the in-situ reaction between Ti and the reinforcements.
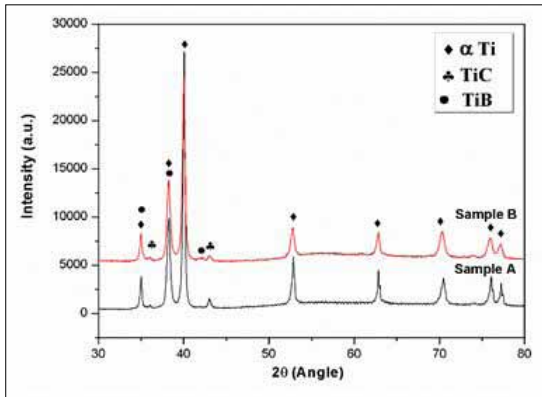
DEVELOPMENT OF TITANIUM BASED IN-SITU COMPOSITES PREPARED BY CONVENTIONAL POWDER METALLURGY ROUTE AND ITS FUTURE ASPECTS

Fig. 4 XRD patterns of sintered samples

Hardness and wear properties of these composites were also studied. The increased hardness and the reduced wear rate indicates that the in-situ phase formations significantly affect these properties [7, 8]. Overall, the combination of reinforcements used in samples A and sample B shows the potential to develop composites with improved mechanical properties. However, the mechanical properties of these composites and the effect of concentration of these reinforcements need further investigation.

Future Aspects

The future appears bright for the various facets of titanium powder metallurgy technology. The increasing need of high-performance composites material for framing of exterior chassis in aerospace and marine industry is considered to be the key driver of the metal matrix composites market. It's being said that, researchers admit that they have only just begun to explore the possibilities of these new materials. With the dramatically growing market for additive manufacturing and consistent property performance of an increasing number of AM titanium components, the use of metal powders for the manufacture of structural components is expected to become more acceptable than before.

References

1. Chawla, K.K., Metal Matrix Composites, in Materials Science and Technology. 2006, Wiley-VCH Verlag GmbH & Co. KGaA.

2. Chawla, K.K., Composite Materials: Science and Engineering. 1998: Springer.

3. Godfrey, T.M.T., P.S. Goodwin, and C.M. Ward-Close, Production of titanium particulate metal matrix composite by mechanical milling. Materials Science and Technology, 2000. **16** (7-8): p. 753-758.

4. Jiao, Y., et al., Effects of Ti5Si3 characteristics adjustment on microstructure and tensile properties of in-situ (Ti5Si3+TiBw)/Ti6Al4V composites with two-scale network architecture. Materials Science and Engineering: A, 2016. **673**: p. 595-605.

5. Zhang, X., et al., Structure and mechanical properties of in-situ titanium matrix composites with homogeneous Ti5Si3 equiaxial particle-reinforcements. Materials Science and Engineering: A, 2017. **698**: p. 73-79.

6. Bernert, T., et al., In situ observation of self-propagating high temperature syntheses of Ta_5Si_3, Ti_5Si_3 and TiB_2 by proton and X-ray radiography. Solid State Sciences, 2013. **22**: p. 33-42.

7. Munir, K.S., P. Kingshott, and C. Wen, Carbon Nanotube Reinforced Titanium Metal Matrix Composites Prepared by Powder Metallurgy — A Review. Critical Reviews in Solid State and Materials Sciences, 2015. **40**(1): p. 38-55.

8. Kondoh, K., et al., Characteristics of powder metallurgy pure titanium matrix composite reinforced with multi-wall carbon nanotubes. Composites Science and Technology, 2009. **69**(7–8): p. 1077-1081.

PREDICTION AND MITIGATION OF BUCKLING TYPE DISTORTION IN ADDITIVELY MANUFACTURED THIN WALLED STRUCTURES

Anil Kumar, Mukul Atri, Kajal Khan and Sankar Seetharaman

ANSYS Inc., Pune, India

Abstract: *Additive manufacturing for complex metallic components brings in lot of challenges during part building process. Engineers find it difficult to mitigate challenges like distortion and residual stresses even after vast experimental experiences. This is particularly true in making of thin metal parts, where these issues can pop up unpredictably and can cause quite a lot of build failures. Simulations using finite element analysis tools have proved to be quite useful in prediction of such issues beforehand. But there are challenges in simulation too. Main challenges in simulation of AM process is the time it takes to solve, especially for thin and complex parts. Additionally, the accuracy of the numerical model depends on many simulation parameters. In the present study, a superlayer based thermo-mechanical model has been presented. This method exhibits not just computational efficiency over full pass-by-pass thermomechanical simulation but also gives very accurate trend of results. The sensitivies of different simulation parameters are studied in detail to obtain a reliable computational model.*

Introduction

Additive Manufacturing (AM) refers to all processes in which the material is joined layer-by-layer to generate a desired shape. AM was initially developed as a rapid prototyping method in which a prototype of mostly plastic part was made before actual manufacturing by well-accepted methodologies, such as forging, CNC, welding etc. Now, AM is transitioning into a real manufacturing process, especially for metal parts. The American Society for Testing and Materials (ASTM) group "ASTM52900-15 – Additive Manufacturing", formulated a set of standards that classify the range of Additive Manufacturing processes into 7 categories, namely; Vat polymerisation, Material jetting, Binder Jetting, Fused deposition modelling (FDM)/Material Extrusion, Powder Bed Fusion (PBF), Sheet lamination and Directed Energy Deposition (DED) [1].

The Powder Bed Fusion (PBF) process consists of about 60% of all metal additive processes [2]. In PBF a thin powder layer is spread over built plate using spreader blade. This layer of powder is selectively melted or sintered using laser or electron beam. Once the layer solidifies, the next layer is spread, and the process continues until the entire part is build [3]. Due to high thermal gradient, residual stresses develop in the build part which causes it to distort [4]. Sometimes the distortion is so severe that it causes the part to bend or to crack. For thin geometries, unpredictable buckling like local deformations are often observed. Brute force trial and error techniques are often implemented to mitigate such issues, but these require a large number of iterations that leads to an excessive cost.

This paper showcases how FEM simulation tools can be used to mitigate issues related to distortion in additive manufacturing processes for thin structures. Thin structures are often manufactured using additive processes which are then used for heat exchangers, pressure vessels, thin iso-grid structures etc. AM can provide significant advantage over traditional manufacturing due to reduction in development times, significant efficiency improvements, weight reduction & considerable reduction in inventory. Main challenges of distortion and residual stress predictions for thin wall parts are carried out in this study. Sensitivities of different

simulation parameters are studied in detail to establish best practices for such simulations.

Numerical Modelling

One-way thermo-mechanical analysis is carried out in ANSYS®, that is, temperatures are mapped from full thermal transient solutions over to static structural solution for stress & deflection calculations. Element birth-death is used in both thermal & structural steps to model the layer by layer process [5]. Only the elements of current layers are in active state (contribute to conduction, stiffness, mass), rest do not contribute till they are alive (powder state) in FEM solution. The transient heat conduction equation solved in the thermal analysis is given by Eq. 1.

$$\frac{\partial}{\partial x}\left(k_x \frac{\partial T}{\partial x}\right) + \frac{\partial}{\partial y}\left(k_y \frac{\partial T}{\partial y}\right) + \frac{\partial}{\partial z}\left(k_z \frac{\partial T}{\partial z}\right) + \dot{q} = \rho c \frac{\partial T}{\partial t} \tag{1}$$

where ρ is the material density, c is the specific heat, T is the temperature, t is time, x, y, and z are the spatial location, q is heat generation per unit volume, and k_x, k_y, k_z are the thermal conductivities in x, y and z directions respectively. Appropriate thermal boundary conditions are imposed in the above equation for solving. Base plate is generally kept at constant temp in PBF machines & the chamber is also heated up. Reduced scaled properties of powder is used to model some heat dissipation via powder. All temperature material constants are dependent.

Standard structural finite element equations derived using the principle of virtual work are used for the static structural solution as given by Eq. 2.

$$([K_e] + [K_e^f])\{u\} - \{F_e^{th}\} = [M_e]\{\ddot{u}\} + \{F_e^{pr}\} + \{F_e^{nod}\} \tag{2}$$

where $[K_e]$ is element stiffness matrix, $[K_e^f]$ is element foundation stiffness matrix, $\{u\}$ is the primary displacement, $\{F_e^{th}\}$ is element thermal load vector, $[M_e]$ is element mass matrix, $\{F_e^{pr}\}$ is element pressure vector, $\{F_e^{nod}\}$ is element nodal load vector. Temperature dependent material properties like Youngs modulus, poissons ratio, thermal expansion coefficient, density, thermal conductivity and specific heat are defined for the analysis. Temperature dependent bilinear isotropic hardening plasticity is used in the structural analysis to capture the plastic deformation. Clamping is modeled by fixed displacements of the clamped locations.

Results and Discussions

To study the effect of different parameters like build geometry, large deformation theory, plasticity, superlayer height, element aspect ratio etc., a thin walled box section has been considered with the dimension of 35 mm x 5 mm x 40 mm in the length, width and build directions respectively. The thickness of the section is taken as 1 mm. The simulation domain is shown in Figure 1. The material for the build and base plate has been considered as Inconel 625. The following process parameters are employed: deposition thickness - 0.05 mm, hatch spacing - 0.1 mm, scan speed - 1000 mm/s and preheat temperature - 80º C.
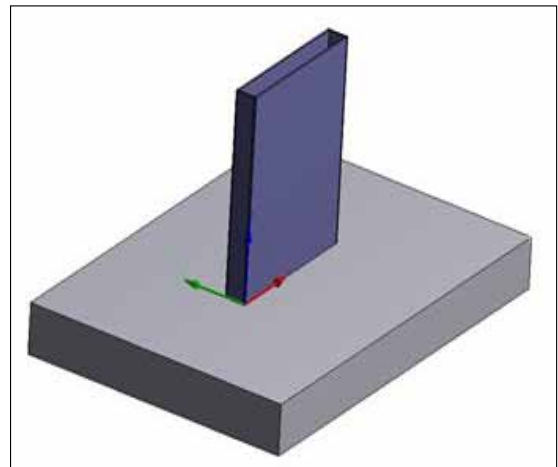

Fig. 1 Schematic representation of the simulation domain.

The observations from the numerical studies are as follows:

a. Buckling like excessive deformation is mostly seen in the build directions.

b. In-plane thermal stresses (Sxx or Syy) are compressive, aiding (Stress stiffening effect) to local buckling along the build direction.

c. Distortion behaviour is highly sensitive to the material, thickness of the thin part as well as the geometry. For example, straight sections are more prone to bulging.
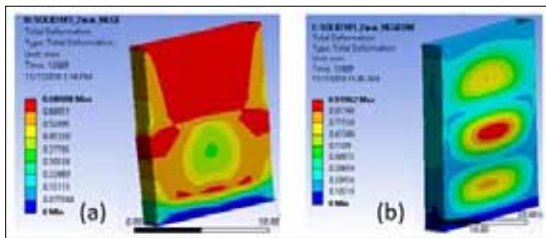

Fig. 2 Predicted distortion using (a) small deformation and (b) large deformation theory

d. To analyse the buckling like behaviour, large deformation theory has to be implemented. Small deformation theory which doesn't account for the update of stiffness can lead to inaccurate deformation behaviour as shown in Figure 2.

e. An elasto-plastic analysis leads to a more realistic distortion and residual stress behaviour as compared to a purely linear elastic analysis.

f. The element size has a great effect on the results. Two cases of mesh sensitivity study have been considered in the present analysis: the superlayer height and the aspect ratio of elements. It has been observed that the distortion is highly sensitive to the superlayer height as shown in Figure 3. Similar observations are made for the element aspect ratio. However, the distortions are similar within a big range of aspect ratios.
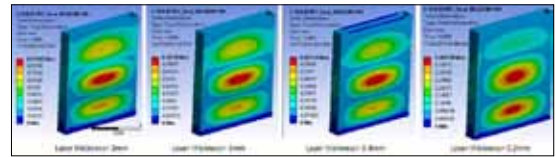

Fig. 3 Predicted distortion for different superlayer thickness

Conclusions

In the present study a finite element based modelling technique has been presented for the simulation of additive manufacturing process of thin parts. Sensitivities of different simulation parameters are studied in detail to establish best practices for such simulations. Further work can be performed to validate the abstraction level used in the superlayer approach.

References

1. *ISO/ASTM52900-15 Standard Terminology for Additive Manufacturing – General Principles – Terminology.*

2. *A.Lundbäck, LE.Lindgren "Modelling of metal deposition. Finite Elements in Analysis and Design," Vol. 47, pp.1169–1177, 2011.*

3. *T.DebRoy, H.L.Wei, J.S.Zuback, T.Mukherjee, JW.Elmer, J.O.Milewski, AM.Beese, A.Wilson-Heid, A.De, W.Zhang "Additive manufacturing of metallic components – Process, structure and properties," Progress in Materials Science Vol. 92, pp.112-224, 2018.*

4. *E.R.Denlinger, J.C.Heigel, P.Michaleris, and T.A.Palmer "Effect of inter-layer dwell time on distortion and residual stress in additive manufacturing of titanium and nickel alloys," Journal of Materials Processing Technology, Vol.215, pp.123–131, 2015.*

5. *A.Malmelöv, A.Lundbäck, LE.Lindgren, Validation of an approach to reduce simulation time for additive manufacturing, In 2017 Simulation for Additive Manufacturing, Munich, Germany, 11-13 October 2017.*

COMPUTATIONAL FLUID DYNAMICS SIMULATIONS FOR ADDITIVE MANUFACTURING

Pareekshith Allu

CFD Engineer & Flow Science Inc., NC, USA.

Abstract: *Laser welding has been replacing traditional welding methods due to its superior productivity, faster scan speeds and lower heat inputs. With better control and smaller heat affected zones, laser processing technology has led to a rise of interest in metal additive manufacturing (AM) processes such as laser powder bed fusion and direct metal deposition.*

Although AM has been generating significant interest, challenges remain towards a more widespread adoption of this technology. These challenges include defect formation such as porosity and spatially non-uniform material properties that occur because of insufficient knowledge of process control. Computational fluid dynamics (CFD) modelling can help researchers understand the effects of process parameters on underlying physical phenomena such as melt pool dynamics, phase change and solidification. With experimental studies successfully capturing melt pool data such as molten metal velocities and temperatures, it is possible to calibrate numerical models using experimental data. These numerical models, which are based on a rigorous solution of the conservation equations, can provide further insights such as fluid convection in the melt pool, temperature gradients and solidification rates.

In this presentation, case studies from industry and academia highlighting the use of CFD and numerical models in understanding powder bed fusion processes are discussed. Process parameter optimization in controlling porosity formation and balling defects for the IN718 alloy are studied in detail. On the one hand, slower laser scan speeds and higher angles of inclination in laser welding can lead to an unstable keyhole configuration, which typically results in porosity. On the other hand, faster scan speeds result in longer melt pools, and Rayleigh instabilities can cause the elongated melt pool to break down into tiny islands of molten metal resulting in balling defects. Additionally, effects of powder packing density, laser power and particle size distribution on the formation of balling defects are explored. It is also seen that recoil pressure and material evaporation play important roles in determining the melt pool dynamics and surface morphology. Finally, melt pool data from the numerical models is used to study and predict the solidification morphology for the IN718 alloy. Based on temperature gradients and solidification rates, which can be obtained through CFD models, it is possible to determine the resulting microstructure evolution and primary dendrite arm spacing resulting from the powder bed fusion processes. These results are compared to experimental data wherever available.

These high fidelity, multiphysics CFD models provide a framework to better understand AM processes from the particle and melt pool scales. Using this information, it will be possible to more accurately model additional aspects of AM processes such as thermal and residual stresses and distortions in the entire part build.

Effects of random powder distribution and material evaporation on melt pool dynamics[1]

A three-dimensional numerical model that incorporates a randomly-distributed powder bed and material evaporation is developed using FLOW-3D to investigate melt pool dynamics with keyhole formation by an Nd-YAG laser. The discrete element method (DEM) was employed to simulate powder packing, which accounts for the motion of a large number of particles including particle/particle and particle/wall interactions. The model was validated by measuring the particle size distributions in specific areas and ensuring that no powder size segregation occurs. Next the flow behaviour of the melt pool is characterized by calibrating parameters in the

numerical model to achieve good agreement with the experimental results. The importance of including material evaporation in the numerical model is demonstrated by measuring the melt pool dimensions, which turn out to be narrower and deeper than when evaporation effects are not considered. Moreover, a keyholing effect is observed due to the recoil pressure resulting from evaporation, which affects surface morphology and surface temperatures of the melt pool. As illustrated in Figure 1, the contours of the cross-sections of the melt region including the dimensions and surface morphology compare very well between the simulations and experiments, justifying the importance of including evaporation effects.
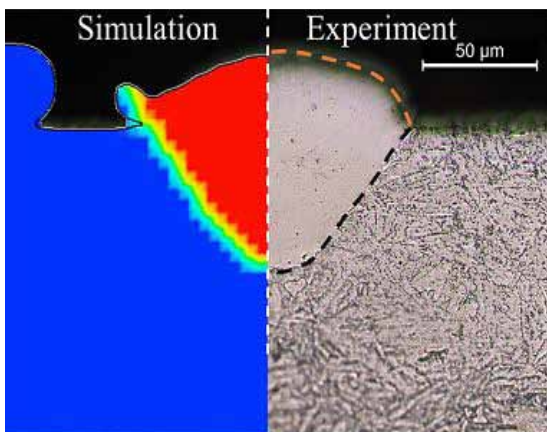

Figure 1: Validation of the melt-pool dimensions (black-dashed line) and the surface morphology (orange-dashed line).

Simulation of Heat Transfer and Fluid Flow in Laser Powder Bed Additive Manufacturing [2]

Process parameters such as laser scan speed, laser power, packing density and particle size distribution have a direct effect on melt pool dynamics in a laser powder bed fusion process. The highly transient nature of the melt pool affects the final surface quality of the solidified melt region.

As illustrated in Figure 1, balling defects occur when the molten pool becomes discontinuous and breaks into separated islands of molten metal. Such defects can be attributed to void formations in the melt pool, which eventually break the melt pool into separate regions as seen in Figures 2(c) – (d). Strong backward flow because of surface tension gradients is usually the driving force behind the formation of these voids.
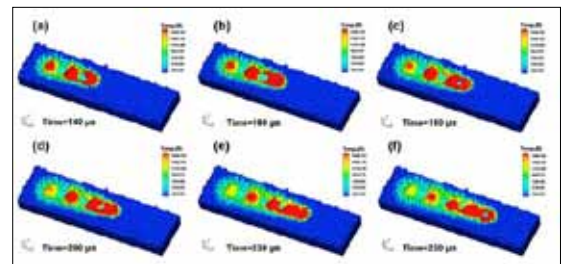
Figure 2: Evolution of molten pool profile illustrating the formation of balling defect.

Additionally, it is found that the high scanning speeds and a particle size distribution which is skewed to a higher number of larger sized particles are detrimental to the surface quality and can potentially cause balling defects. However, using a higher powder packing density can potentially reduce the onset of balling defects. This paper summarizes the effects of several process parameters on melt pool dynamics and formation of balling defects for L-PBF processes in Inconel® 718.

Modelling of heat transfer, fluid flow and solidification microstructure of nickel-base superalloy fabricated by laser powder bed fusion[3]

The microstructure evolution in laser powder bed fusion processes is investigated using fluid flow and heat transfer models built in FLOW-3D. Solidification parameters, particularly solidification rate and temperature gradients that are calculated from temperature fields are used

to assess solidification morphology and grain size for L-PBF of Inconel® 718 using existing theoretical models. The numerical models are validated by calibrating the dimensions of the melt pool for two partially overlapping laser scan tracks, and it can be seen below in Figure 3 that the cross-sectional dimensions compare well between experiments and simulations.
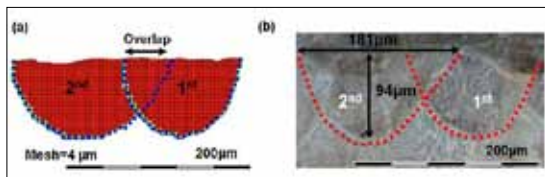

Figure 3 : Comparison of (a) calculated and (b) experimentally measured molten pool shapes.

Solidification parameters at the molten pool side edge and the molten pool trailing end are calculated. These locations correspond to the maximums and minimums of solidification parameters, and by using existing analytical models for welding and cladding processes, it is calculated that columnar dendrite is the dominant morphology in IN718 made by L-PBF. The primary dendrite arm spacing (PDAS) is another important microstructure parameter and the dendrite size was estimated to be between 1.32 and 1.87 μm. The calculated solidification morphology and PDAS are consistent with experimentally observed results. The reader is invited to refer to the cited journal article for more information on the methodology and results.

Multi-physics modelling of single/multiple-track defect mechanisms in electron beam selective melting[4]

A high-fidelity powder scale and fluid flow model is built in FLOW-3D to investigate detailed formation processes of single/multiple-track defects, such as balling, inter-track void formation and single-track non-uniformity in a selective electron beam melting process. The

computation models reveal the influence of process parameters such as scan patterns, laser powers and hatch spacing on the subsequent quality of the melt pool as seen in Figure 4 below.
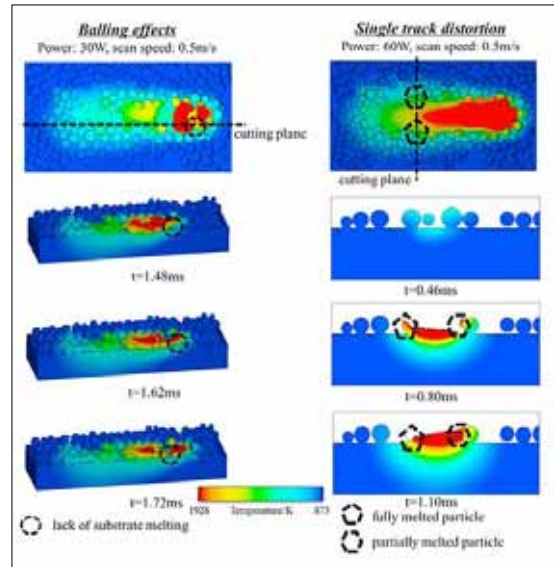

Figure 4 : Simulation results of balling defects and single-track distortions.

Several scan patterns, including unidirectional scans, counter-directional scans, layer-wise rotated and inter-laced scan strategies are analysed in detail to investigate their effects on formation of voids. It is found that the hatch spacing must be no larger than the width of melted region within the substrate and that the inter-laced scan strategies result in the least void formation among all the scan strategies implemented.

References

1. *Wu, Yu-Che & San, Cheng-Hung & Chang, Chih-Hsiang & Lin, Huey-Jiuan & Marwan, Raed & Baba, Shuhei & Hwang, Weng-Sing. (2017). Numerical modeling of melt-pool behavior in selective laser melting with random powder distribution and experimental validation. Journal of Materials Processing Technology. 254. 10.1016/j.jmatprotec.2017.11.032.*

2. *Mesoscopic simulation of heat transfer and fluid flow in laser powder bed additive manufacturing." Lee, Y. S., and W. Zhang, Proceedings of the Annual International Solid Freeform Fabrication Symposium, Austin, TX, USA. 2015.*

3. *Lee, Yousub & Zhang, W. (2016). Modelling of heat transfer, fluid flow and solidification microstructure of nickel-base superalloy fabricated by laser powder bed fusion. Additive Manufacturing. 12. 178-188. 10.1016/j.addma.2016.05.003.*

4. *Wentao Yan, Wenjun Ge, Ya Qian, Stephen Lin, Bin Zhou, Wing Kam Liu, Feng Lin, Gregory J. Wagner, Multi-physics modelling of single/ multiple-track defect mechanisms in electron beam selective melting, Acta Materialia, Volume 134, 2017, Pages 324-333, ISSN 1359-6454.*